

# ULTRAFAST CARRIER AND PHONON DYNAMICS IN LAYERED TWO-DIMENSIONAL MATERIALS

A Dissertation

Presented to the Faculty of the Graduate School  
of Cornell University

in Partial Fulfillment of the Requirements for the Degree of  
Doctor of Philosophy

by

Haining Wang

August 2016

© 2016 Haining Wang  
ALL RIGHTS RESERVED

# ULTRAFAST CARRIER AND PHONON DYNAMICS IN LAYERED TWO-DIMENSIONAL MATERIALS

Haining Wang, Ph.D.

Cornell University 2016

As semiconductor markets have matured, new market demands focus on the low cost integration of multiple sensing capabilities with Internet connectivity, *i.e.*, the Internet of Things (IoTs). Although IoTs have already become the main driving force for device innovation, and its market value is expected to reach  $\sim$  \$1.7 Trillion in 2020 [110], the traditional semiconductor technologies have not been able to provide device solutions for many emerging IoTs applications. For instance, it is desirable to integrate high quality thin film semiconductors and their heterostructures on flexible substrates without material growth issues (lattice mismatch and defects); traditional MEMS devices cannot easily scale beyond 10 GHz due to challenges in nanofabrication processes; low-cost high performance far-infrared photoemitters and photodetectors are needed for integrated medical and spectroscopy applications.

Nanomaterials could provide solutions for these device innovation challenges. The objective of nanomaterial research is not to replace, but to complement the traditional semiconductor technologies. The most common innovation approach is to select nanomaterials possessing unique properties that can be utilized for a particular application. For example, graphene plasmonic devices are best for THz and far-infrared photodetection applications; layered materials and their heterostructures are attractive because they can be built on any substrate by transfer techniques instead of growth.

In this thesis, I present my Ph.D. research on two-dimensional (2D) layered materials. My research has been motivated by device applications, and has focused on studying optical, mechanical, electronic and plasmonic properties of 2D materials. In chapter 1, a brief introduction to 2D materials is provided. The experimental techniques that have been used during my Ph.D. research are discussed in chapter 2. Next, the experimental work on the hot carrier and phonon relaxation dynamics in graphene is presented in chapter 3. From chapter 4 to 7, I present my work on monolayer and multilayer molybdenum disulfide ( $\text{MoS}_2$ ). The topics include photoexcited carrier recombination dynamics of monolayer and few layer  $\text{MoS}_2$ , the ultrafast photoresponse of monolayer  $\text{MoS}_2$  photodetectors, and THz coherent mechanical oscillations of few layer  $\text{MoS}_2$ .

## BIOGRAPHICAL SKETCH

Haining Wang was born in Shanxi China, and finished his elementary and high school study in Beijing China. In 2003, he left Beijing to pursue undergraduate study in Electrical Engineering at McGill University in Quebec, Canada. He started research work with Prof. Ramesh Abhari in signal integrity simulation in 2005. Towards the end of his study at McGill, he joined Gennum *Corp.* as an analog circuit designer intern in 2006 to explore alternative career paths. His strong interest in device physics drove him back to research after one and half years in industry, and he was admitted Cornell University in 2008. At Cornell, he was deeply impressed by Prof Farhan Rana's nanoscale physics lectures and decided to join the Cornell Optoelectronics Lab. He received most of his optics training from Jared Strait, and nano-fabrication training from Wei-min Chan and Shriram Shivaraman. In 2014, he met his wife Ya Li in Austin Texas while paying a visit to his college friend, and they got married in 2015. Haining was the winner of the Cornell ECE Best Ph.D. Thesis Award in 2016.

Dedicated to my wife Ya Li, mother Qin Gao, father Shucheng Wang and my  
brother Chenyu Wang.

## ACKNOWLEDGEMENTS

There are many people that have positively influenced my life in different ways. Over the years, I have slowly realized that without their technical, emotional and financial support, I could not even have the chance to think about my postgraduate education. When I was much younger, I often attributed my failures and successes to luck and personal effort, but now I see them as weaknesses of my personality and opportunities provided by kind hearts.

I am deeply grateful to my parents for paying for my undergraduate education at McGill University. They have spent years of their savings for a very clear vision: through their support, the exploratory life I experienced in Canada helped me grow into a more independent, compassionate and responsible person.

Prof. Ramesh Abhari encouraged and trained me to become an independent researcher at McGill University. She was extremely kind and patient. Every week she spent an hour with me to carefully plan my research goals. During my internship at Gennum Corp., my supervisor, Ranjit Singh, guided me through the entire integrated analog circuit design flow, and tried very hard to secure my position during the great recession.

Prof. Farhan Rana has been my Ph.D. committee chair since I joined the Cornell ECE department . He is an exceptionally rigorous scholar and the most available advisor I have seen. There were countless nights that he dropped into our lab and spent hours with me discussing my experimental set-ups and data. I have always been inspired by his comprehension of a broad range of physics and his effort in continuous learning. I would also like to thank Prof. Jiwoong Park, Prof. Dan Ralph, and Prof. Edwin Kan for being my committee members, providing critiques and guidance to my research. Their suggestions regarding

my communication skills have greatly improved my research presentation ability over the past years. I am thankful for the many research discussions and collaborations with Prof. Michael Spencer and Prof. Debdeep Jena as well.

Jared Strait and Paul George were the senior students in our group when I joined. During my first two semesters, they trained me in aligning and building optical set-ups. Their effort and kindness helped me quickly becoming an independent experimentalist. I met Wei-min Chan and Shriram Shivaraman in the cleanroom at the Cornell CNF. Although they were from different research groups, they never hesitated to share their fabrication knowledge and were my clean-room mentors during my first two years at Cornell. Later, we became collaborators and good friends. Changjian Zhang was a masters student in our group, and she assisted me in most of my published work. Ryan Frink and Okan Köksal are junior students in our group, and have helped in proof-reading many of my writings. Sunwoo Lee is my roommate. His joyful and ambitious character always encourages me.

Lastly, I want to thank my wife Ya Li. Because we have been physically separated throughout my Ph.D., Ya visited me from Texas every month to minimize the impact of the long distance to our relationship. She is kind and considerate. No matter how late I work into the night, she is always up waiting for me to call her after I finish my work. Many times she has scarified her emotional needs to avoid interrupting my research. I feel deeply indebted to her.

## TABLE OF CONTENTS

Biographical Sketch . . . . .	iii
Dedication . . . . .	iv
Acknowledgements . . . . .	v
Table of Contents . . . . .	vii
List of Tables . . . . .	x
List of Figures . . . . .	xi
<b>1 Introduction to layered materials</b>	<b>1</b>
1.1 Layered two-dimensional materials . . . . .	1
1.2 Experimental techniques . . . . .	4
<b>2 Characterization of layered materials</b>	<b>7</b>
2.1 Introduction . . . . .	7
2.2 Spontaneous and stimulated Raman scattering . . . . .	8
2.3 Confocal transmission and reflection measurements . . . . .	13
2.4 Broadband photoconductivity measurements . . . . .	15
2.5 Lock-in electrical transport measurement for linear devices . . . . .	16
2.6 S/N ratio optimization in ultrafast spectroscopies . . . . .	18
2.7 Spatially-resolved ultrafast measurements . . . . .	22
<b>3 Hot carrier and phonon relaxation dynamics in graphene</b>	<b>24</b>
3.1 Introduction . . . . .	24
3.2 Sample preparation and experiment set-up . . . . .	25
3.3 The electron-phonon scattering model . . . . .	28
3.4 Conclusion . . . . .	33
<b>4 Defect assisted carrier recombination dynamics in monolayer MoS<sub>2</sub></b>	<b>35</b>
4.1 Introduction . . . . .	35
4.2 Sample preparation . . . . .	36
4.3 Measuring photoexcited carrier recombination dynamics . . . . .	37
4.4 Experimental results and discussion: . . . . .	41
4.5 Auger carrier capture model . . . . .	46
4.6 Optically induced sample damage . . . . .	53
4.7 Parameter space of Auger capture coefficients . . . . .	55
4.8 Two Photon Absorption OPOP measurements . . . . .	56
4.9 Comparison with other ultrafast techniques . . . . .	59
4.10 Conclusion . . . . .	60
<b>5 Ultrafast photoresponse of monolayer MoS<sub>2</sub> photodetector</b>	<b>62</b>
5.1 Introduction . . . . .	62
5.2 Motivations to use the TPPC technique . . . . .	62
5.3 TPPC technique . . . . .	63
5.4 Device fabrication and characterization . . . . .	66

5.5	Experimental results . . . . .	67
5.6	Ultrafast photoresponse of the metal-MoS <sub>2</sub> junction . . . . .	70
5.7	Carrier capture/recombination model . . . . .	73
5.8	Gate dependent TPPC measurements . . . . .	77
5.9	Simulation of photoexcitation at a metal-MoS <sub>2</sub> junction . . . . .	79
5.10	Circuit models of the metal-MoS <sub>2</sub> junction . . . . .	80
5.11	Sample variations . . . . .	83
5.12	Discussion . . . . .	84
5.13	Conclusion . . . . .	86
<b>6</b>	<b>Surface recombination in transition metal dichalcogenides</b>	<b>87</b>
6.1	Introduction . . . . .	87
6.2	Carrier recombination dynamics in bulk MoS <sub>2</sub> . . . . .	89
6.3	OPOP experimental set-up and sample preparation . . . . .	91
6.4	Experimental results and discussion . . . . .	94
6.5	Carrier recombination model . . . . .	99
6.6	Scaling of the carrier Lifetime with the number of layers: . . . . .	101
6.7	Defect refilling dynamics . . . . .	105
6.8	Conclusion . . . . .	107
<b>7</b>	<b>THz mechanical oscillations in transition metal dichalcogenides</b>	<b>108</b>
7.1	Introduction . . . . .	108
7.2	Introduction to high frequency MEMS . . . . .	109
7.2.1	MEMS oscillations in the time and frequency domain . . . . .	111
7.2.2	Quality factor . . . . .	112
7.2.3	BAW MEMS filters and resonators . . . . .	114
7.2.4	Coherent acoustic oscillations in MEMS . . . . .	116
7.3	Ultra-high frequency coherent phonon oscillations . . . . .	118
7.4	Ultrafast optical excitation of coherent phonons . . . . .	120
7.4.1	Optical interference grating . . . . .	120
7.4.2	Nanostructured grating . . . . .	122
7.4.3	Stress/heat pulses . . . . .	123
7.4.4	Surface space-charge field . . . . .	124
7.4.5	Displacive excitation and Raman scattering . . . . .	125
7.5	THz coherent mechanical oscillations in few-layer MoS <sub>2</sub> . . . . .	129
7.6	Displacive excitation of the coherent THz mechanical oscillations	133
7.7	Surface scattering limited coherent phonon lifetime . . . . .	135
7.8	Discussion . . . . .	138
<b>A</b>	<b>Exfoliation of 2D materials</b>	<b>141</b>
A.1	Substrate selection . . . . .	141
A.2	Substrate preparation . . . . .	142
A.3	Exfoliation . . . . .	144
A.4	E-beam lithography on quartz wafers . . . . .	147



## LIST OF TABLES

1.1	Quantum efficiency of direct gap transition metal dichalcogenides (TMDs). . . . .	3
3.1	Experimentally determined quantities. Ratio of Raman G-peak and D-peak intensities $I_G/I_D$ , the number of graphene layers $N$ , the extracted values of the optical phonon lifetime $\tau_{ph}$ , and the average equilibrium carrier density per layer $n_o$ . . . . .	25
4.1	Parameter values used in the simulations to fit the transient data.	50
5.1	Fitting parameters. Parameter values used in the simulations to fit the photovoltage correlation data. . . . .	76

## LIST OF FIGURES

1.1	Graphene and monolayer MoS <sub>2</sub> . Whereas graphene consists of a single layer of carbon atoms in the honey-comb configuration, monolayer MoS <sub>2</sub> has three layers of atoms. The unit cell of monolayer MoS <sub>2</sub> can be drawn in two different but equivalent ways: a triangular or a hexagonal configuration. Graphene is a semi-metal with zero bandgap and linear band dispersion; monolayer MoS <sub>2</sub> is a 2D direct bandgap semiconductor with exciton photoexcitation energy at $\sim 1.9$ eV. Note that monolayer MoS <sub>2</sub> has spin-degenerate conduction bands. The graphene/graphite phonon band is given by Mohr2007 <i>et al.</i> [102].	2
1.2	The advantages of layered 2D materials. . . . .	4
1.3	Versatility of ultrafast spectroscopies. . . . .	5
1.4	Nanostructured material research approach. . . . .	6
2.1	A confocal microscopy system for transmission, reflection, photoluminescence and Raman spectroscopies. The pinhole is used to select the transmitted/reflected light from micron-sized samples at the microscope image plane. . . . .	7
2.2	Characterization table and phonon modes of graphene [154, 3]. .	12
2.3	The reflection and transmission measurement. Electric and magnetic field definitions in transmission and reflection configurations.	14
2.4	Broadband photoconductivity measurement configuration. The broadband light is dispersed into monochromatic light by the grating spectrometer. In the current mode, the lock-in amplifier has 1 K $\Omega$ input resistance. . . . .	16
2.5	FTIR broadband photoconductivity measurement configuration. The DC lock-in output (the amplitude of the photodetector AC response) is fed back to FTIR. The product of lock-in time constant and the mirror velocity, which is the FTIR sampling distance without aliasing, determines the upper limit of the FTIR output spectrum. . . . .	17
2.6	Lock-in amplifier transport experiment. The lock-in amplifier on the left side supplies an AC driving voltage and measures the channel voltage drop, while the lock-in amplifier on the right side is phase-locked to the other lock-in, and measures the channel current. . . . .	18
2.7	The single chopped and double chopped configuration. . . . .	20
2.8	OPOP pump leakage filtering. The combination of optical and spatial filtering techniques can efficiently reject the pump beam leakage. By careful implementation of the illustrated filtering techniques, a single chopped OPOP measurement should provide a better S/N than the double chopped OPOP configuration.	21

2.9	Non-overlapping OPOP experiment. The $4F$ configuration has advantages in spatial resolution and flexibility, but suffers from interference problems at zero pump-probe delay. . . . .	23
3.1	The ultrafast optical pump optical probe setup. Note that the double chopped configuration is actually done as in Figure 2.7. .	26
3.2	Graphene OPOP transients. Measured differential probe transmissions (normalized to peak value) (circles). The autocorrelation of the $\sim 100fs$ pump and probe pulses(dashed lines), and the best-fit theoretical curves(solid lines) are plotted for different graphene samples. The extracted values of the average optical phonon lifetime $\tau_{ph}$ are indicated for each graphene sample. . . .	28
3.3	Cartoon illustration of an OPOP experiment on graphene. The curved green arrows represents the subsequent hot carrier thermalization and relaxation after the pump photoexcitation. . . . .	29
3.4	Intravalley and intervalley electron-phonon scattering in graphene.	30
3.5	Scattering rates and phase space of carrier-phonon interactions. (a)The electron intraband scattering time due to optical phonon scattering is plotted as a function of the electron energy [122]. (b) The phonon Brillouin zone is shown together with the annular regions (not to scale) at the $\Gamma$ and $K(K')$ points, in which the optical phonons participate in electron-phonon scattering. . . . .	30
3.6	Hot carrier cooling simulation results. (a) Calculated electron-phonon scattering rate vs electron energy is plotted for values of $T_c$ equal to 1250, 1500, 1750, and 2000 $K$ : total electron density is assumed to be $7 \times 10^{11} cm^2$ . Phonon temperature is fixed at 900 $K$ . (b) Measured differential probe transmissions (normalized to the peak value) (circles) and the best-fit theoretical curves (lines) are plotted for different pump pulse energies (2.5, 6, and 9.8 $nJ$ ). [(c) and (d)] The calculated electron and phonon temperatures and the phonon occupation numbers are plotted as a function of time after photoexcitation. The photoexcited electron-hole densities are assumed to be $2 \times 10^{11}$ and $7 \times 10^{11} cm^2$ . The equilibrium electron density is assumed to be $10^{11} cm^2$ . . . . .	33
4.1	Rendered image illustration of the ultrafast OPOP experiment. Monolayer $MoS_2$ samples were exfoliated onto quartz substrates. The strong blue pulses were used to excite electron-hole pairs, and the weak red pulses were designed to measure the carrier recombination dynamics after the pump excitation. . . . .	35

4.2	Optical conductivity of monolayer MoS <sub>2</sub> . (a,b,c,d) The measured real and imaginary parts of the optical conductivity of a monolayer MoS <sub>2</sub> sample are plotted for 5 K and 300 K. The A and B exciton resonances, as well as the probe photon energy are also indicated. (e) Schematic of the optical pump-probe scheme is shown. The probe differential transmission is affected predominantly by changes in the real part of the optical conductivity due to intraband absorption (intra-conduction band and intra-valence band absorption). . . . .	38
4.3	OPOP transient of monolayer MoS <sub>2</sub> . (a) The measured differential transmission $\Delta T/T$ of the probe pulse is plotted as a function of the probe delay with respect to the pump pulse. The pump fluence is $\sim 16 \mu J cm^{-2}$ and T=300 K. (b) A zoomed-in plot of the data in (a) shows three different temporal regions: (I) $\Delta T/T$ reaches its negative maximum within $\sim 500 fs$ . (II) A fast recovery of the negative $\Delta T/T$ then occurs within $\sim 2 ps$ . (III) Finally, a slow recovery of the negative $\Delta T/T$ lasts for more than a hundred picoseconds. . . . .	41
4.4	Pump fluence dependent OPOP transients. (a) The measured $ \Delta T/T $ of the probe pulse is plotted as a function of the probe delay for different pump fluences (1, 2, 4, 8, 16, and $32 \mu J cm^{-2}$ ) at T=300 K. The slow transient in region (III) appears to be nearly exponential with a time constant of 60-70 ps. . . . .	42
4.5	Quantum efficiency and temperature dependent OPOP transients. (a) Radiative quantum efficiency of a suspended monolayer MoS <sub>2</sub> sample, obtained by integrating the photoluminescence (PL) spectra, is plotted as a function of the optical pump power (pump wavelength was 532 nm). T=300 K. (b) The measured $\Delta T/T$ (normalized) of the probe pulse is plotted as a function of the probe delay for two different temperatures (5 K and 300 K). The data shows no significant temperature dependence of the time scales associated with the transient. The pump fluence was $\sim 32 \mu J cm^{-2}$ in both cases. . . . .	44
4.6	Normalized pump fluence transients. (a) $\Delta T/T$ (normalized) is plotted for two different pump fluences, 1 and $32 \mu J cm^{-2}$ , at T=300 K. Whereas the slow time scale in region (III) is completely independent of the pump fluence, the fast time scale in region (II) becomes marginally faster (by 10-15%) at highest pump fluence compared to at the lowest pump fluence. (b) The peak value of $ \Delta T/T $ is plotted as a function of the photoexcited carrier density (estimated from the pump fluence) showing a mildly sub-linear dependence. The fit obtained from the Auger carrier capture model is also shown. T=300 K. . . . .	45

4.7	Four basic Auger Processes. Four basic Auger processes for the capture of electrons ((a) and (b)) and holes ((c) and (d)) at defects are depicted. The approximate dependence of the capture rates on the electron and hole densities is also indicated for each process [125, 77, 127]. In n-doped samples, processes (a) and (c) are expected to dominate for electron and hole capture, respectively, for low to moderate photoexcited carrier densities. . . . .	47
4.8	Cartoon illustration of the ultrafast carrier dynamics in monolayer MoS <sub>2</sub> . (I) After photoexcitation, the carriers thermalize and cool and form a correlated electron-hole plasma. (II) Most of the holes, followed by the electrons, are captured by the fast defects within 1-2 ps. A small fraction of the photogenerated holes is also captured by the slow defects. (III) After all the photoexcited holes have been captured and the electrons have filled the fast traps completely, the remaining photoexcited electrons are captured by the slow defects on a 60-70 ps time scale and the slow transient lasts for more than 100 ps. . . . .	49
4.9	$\Delta T/T$ transient simulations. (a, b) The measured and calculated $\Delta T/T$ (pump fluence normalized) are plotted as a function of the probe delay. The calculations are done for two different and extreme values of the pump fluence, 1 and 32 $\mu Jcm^{-2}$ , used in our experiments. The Auger carrier capture model reproduces all the time scales observed in the measurements over the entire range of the pump fluence values used. (c) The simulated electron and hole densities are plotted as a function of time after photoexcitation for 32 $\mu Jcm^{-2}$ pump fluence. (d) The simulated electron occupations, $F_f$ and $F_s$ , of the fast and slow traps are plotted as a function of time after photoexcitation for 32 $\mu Jcm^{-2}$ pump fluence. . . . .	52

4.10	Optically induced damage in monolayer MoS <sub>2</sub> . (a) Optical microscope image of a sample damaged by a $\sim 128 \mu J cm^{-2}$ pump pulse is shown. No sign of damage is visible. (b) A scanned Raman image corresponding to the energy splitting between the $A_{1g}$ and $E_{2g}$ modes is shown for a sample damaged by a $\sim 128 \mu J cm^{-2}$ pump pulse. (c) A sample damaged by a $\sim 128 \mu J cm^{-2}$ pump pulse shows large absorption throughout the bandgap. (d) The transmission of the probe pulse at $905 nm$ wavelength in a damaged sample gets overwhelmed by the increased absorption inside the bandgap and, consequently, the dynamics observed by the probe pulse become completely different compared to the dynamics observed in an undamaged sample. A damaged sample shows a large slow component in the transient that has a time scale much longer than any of the time scales observed in an undamaged sample. (e,f) Possible probe absorption through optically induced defect states. . . . .	54
4.11	A C++ parameter solver. The flow diagram demonstrates how the fitting parameters were found by a C++ ODE parameter solver. . . . .	55
4.12	Fitting error given by the C++ parameter solver. This plot shows the Least Mean Square error given by the automatic ODE parameter solver in Figure 4.11 as a function of the slow and fast trap density. Good fitting exists for a wide range of slow and fast trap densities. . . . .	56
4.13	Optimized fitting parameters given by the C++ parameter solver. The fitting values given in Table 4.1 are plotted against the automatically generated parameter values given by the C++ ODE parameter solver. . . . .	57
4.14	TPA OPOP transients. (a) OPOP transients of three different pump fluences are plotted. (b) we decompose the measured $1.8 mJ/cm^2$ transient into 2 parts: a TPA component and a carrier absorption component (CA). (c) By using the CA data in (b), we are able to reconstruct the $0.6$ and $3 mJ/cm^2$ transients by assuming that the photoexcited carrier density has a quadratic dependence on the pump fluence.(d) Other than a slight difference in time resolution, the non-degenerate and degenerate techniques are consistent with each other. . . . .	59

- 4.15 OPTP and PL transients of monolayer MoS<sub>2</sub> by Docherty **et al.** [34]. Results reported by Callum [34] are in very good agreement with our experimental and theoretical results, and show that both electron and hole populations decay in the first 1-2 *ps* after photoexcitation, and that one carrier type (holes in our case) is almost entirely captured by defects in the first 1-2 *ps* with a small fraction of the other carrier type (electrons in our case) being captured over much longer time scales. . . . . 60
- 5.1 TPPC experiment setup. (a) Optical micrograph of a fabricated back-gated monolayer metal-MoS<sub>2</sub> photodetector on SiO<sub>2</sub>/Si substrate is shown. (b) A schematic of the two-pulse photovoltage correlation (TPPC) experiment is shown. Two time-delayed 452 *nm* optical pulses, both obtained via upconversion from a single Ti:Sapphire laser, are focused at one of the metal-semiconductor Schottky junctions. The generated DC photovoltage is recorded as a function of the time delay between the pulses. A lock-in detection scheme is used to improve the signal-to-noise ratio. The arrow indicates the positive direction of the photocurrent (and the sign of the measured photovoltage) from the illuminated metal contact. (c) A low-frequency circuit model of the device and measurement. The current source  $I_2(t, \Delta t)$  represents the short circuit current response of the junction in response to two optical pulses separated by time  $\Delta t$ .  $R_j$  is the resistance of the metal-MoS<sub>2</sub> junction.  $R_{\text{MoS}_2}$  is the resistance of the MoS<sub>2</sub> layer.  $R_{\text{ext}}$  is the external circuit resistance (including the  $\sim 10 M\Omega$  input resistance of the measurement instrument). . . . . 64

5.2	<p>TPPC experiment results. (a) The measured two-pulse photovoltage correlation (TPPC) signal <math>V_c(\Delta t)</math> is plotted as a function of the time delay <math>\Delta t</math> between the pulses. <math>T = 5K</math>. Gate bias is <math>0 V</math>. The pump fluence is <math>8 \mu J cm^{-2}</math>. The quantity <math>\Delta V_c(\Delta t)</math> is the difference between <math>V_c(\Delta t)</math> and its maximum value which occurs when <math>\Delta t \rightarrow \infty</math>. (b) <math> \Delta V_c(\Delta t) </math> is plotted on a log scale as a function of the time delay <math>\Delta t</math> between the pulses in order to show the two distinct timescales exhibited by <math>V_c(\Delta t)</math>. The two curves are for two different extreme temperatures: <math>T = 5 K</math> and <math>T = 300 K</math>. The plot shows two distinct timescales: (i) a fast timescale of <math>\sim 4.3 ps</math>, and (ii) a slow timescale of <math>\sim 105 ps</math>. Gate bias is <math>0 V</math>. The pump fluence is <math>8 \mu J cm^{-2}</math>. The two different timescales are observed at both temperatures and these timescales are largely temperature independent. (c) The measured two-pulse photovoltage correlation (TPPC) signal <math> \Delta V_c(\Delta t) </math> is plotted as a function of the time delay <math>\Delta t</math> between the pulses for different pulse fluences: 1, 2, 4, 8, and <math>16 \mu J cm^{-2}</math>. <math>T = 300K</math>. Gate bias is <math>0 V</math>. The two different timescales are observed at all values of the pump fluence and these timescales are not very sensitive to the pump fluence. . . .</p>	68
5.3	<p>Theoretical modeling and fitting of TPPC experiment results. (a) The energy band diagram (bottom) of the the metal-MoS<sub>2</sub> junction (top) is plotted as a function of the position in the plane of the MoS<sub>2</sub> monolayer after photoexcitation with an optical pulse. The Schottky barrier height is <math>\phi_B</math>. The Figure is not drawn to scale. (b) The measured (symbols) and computed (solid lines) photovoltage correlation signals <math> \Delta V_c(\Delta t) </math>, normalized to the maximum value, are plotted as a function of the time delay <math>\Delta t</math> for different pump fluence values: 4, 8, and <math>16 \mu J cm^{-2}</math>. <math>T = 300K</math>. The carrier capture model reproduces all the timescales observed in the measurements over the entire range of the pump fluence values used. (c) The scaling of the measured (symbols) and computed (solid line) values of <math> \Delta V_c(\Delta t = 0) </math> with the pump pulse fluence is shown. The error bars are the recorded peak-to-peak noise level of lock-in amplifier during each measurement. . . .</p>	73
5.4	<p>Band diagram of metal-MoS<sub>2</sub> junction. The effect of the gate voltage <math>V_g</math> on the energy band diagram of the the metal-MoS<sub>2</sub> junction is depicted when (a) <math>V_g = 0 V</math>, and (b) <math>V_g \gg 0 V</math>. The in-plane electric field increases near the metal junction with an increase in the gate voltage. . . . .</p>	77

5.5	Gated TPPC experiment results. The measured two-pulse photovoltage correlation (TPPC) signal $ \Delta V_c(\Delta t) $ is plotted as a function of the time delay $\Delta t$ between the pulses for different gate bias values: -3, 0, 3, 6 V. $T = 300K$ . The pump fluence is $8 \mu J/cm^2$ . As in Figure 2(b,c) in the article, two distinct time scales are observed in the dynamics and these time scales are largely independent of the gate bias. . . . .	78
5.6	Numerical simulation of photoexcitation at metal-MoS <sub>2</sub> junction. Finite Difference Time domain (FDTD) simulation of the optical excitation of the metal-MoS <sub>2</sub> junction is shown. The location of the MoS <sub>2</sub> layer is indicated by the dashed line. The simulation shows that a portion of the MoS <sub>2</sub> layer of length equal to a few hundred nanometers is photoexcited even underneath the metal. . . . .	79
5.7	Circuit model of the metal-MoS <sub>2</sub> photodetector. A high-frequency circuit model of the photodetector is shown in (a). The resistances and capacitances associated with the metal-MoS <sub>2</sub> junction are depicted in (b). $R_j$ and $C_j$ are the resistance and the capacitance associated with the metal-MoS <sub>2</sub> junction. $R_{MoS_2}$ is the resistance of the undepleted MoS <sub>2</sub> region. $C_p$ is an external parasitic capacitance and $R_{ext}$ is the external circuit resistance (including the input resistance of the measurement instrument). . . . .	81
5.8	Electrostatic simulation of the monolayer MoS <sub>2</sub> photodetector. The bias voltage is 1V and symmetric boundary condition is used on the left boundary (the 1 V side), and zero field boundary condition was applied to the other three sides. The extracted intrinsic capacitance is $\sim 0.03 fF/\mu m$ . . . . .	83
5.9	TPPC experiments on three different monolayer MoS <sub>2</sub> photodetectors. The experiments were performed under $8 \mu J/cm^2$ pump fluence at room temperature. The black curves are the theoretical fittings with the same set of Auger capture coefficients but different slow trap densities: $1 \sim 2 \times 10^{13}/cm^2$ for device A and B, $\sim 5 \times 10^{12}/cm^2$ for device C. . . . .	84
6.1	Pump fluence dependent OPTP measurements of bulk MoS <sub>2</sub> [142]. (a) OPTP transients for four pump fluences (0.2, 0.4, 0.8, 1.2 $\mu J/cm^2$ ) at 45 K. The time constants are the initial exponential relaxation time scale. (b)The Ti-sapphire laser has 81 MHz repetition rate, and pump pulses are separated by 12 ns in time. The slow carrier recombination (tens of nanoseconds) results in a background doping ( $\Delta N_-$ ) right before the photoexcitation. $\Delta N_+$ is the photoexcited carrier density right after the photoexcitation. (c) Extracted carrier recombination rate has a linear dependence on the photoexcited carrier density. . . . .	90

6.2	Optical conductivity and photoexcitation in few layer MoS <sub>2</sub> . (a) Nondegenerate ultrafast optical-pump optical-probe (OPOP) experiment on few-layer MoS <sub>2</sub> . (b) Bandstructure of few-layer MoS <sub>2</sub> and depiction of electron photoexcitation from the valence band and midgap defect states into the conduction band. (c)(d) The measured optical conductivities (real part(c) and imaginary part(d)) of few-layer MoS <sub>2</sub> samples are normalized to their layer numbers and plotted. . . . .	92
6.3	Temperature dependent optical conductivity measurements. (a,b) Temperature dependent transmission and reflection measurements on few-layer MoS <sub>2</sub> . (c,d) Real part of the optical conductivity of few-layer MoS <sub>2</sub> . Temperature dependent $\sigma_r$ is normalized to the number of layers and obtained from transmission and reflection measurements. . . . .	93
6.4	OPOP transients of few layer MoS <sub>2</sub> samples. (a,b) Measured differential transmission transients ( $\Delta T/T$ ) of few-layer MoS <sub>2</sub> ((a) 4-layer and (b) 10-layer as representatives of all measured samples) are plotted at different time scales and for different substrate temperatures. The negative dip in $\Delta T/T$ near zero probe delay is attributed to two-photon absorption between the pump and probe pulses. The positive part of $\Delta T/T$ right after photoexcitation comes from the decreased defect absorption of the probe pulse caused by the ionization of the defects by the pump pulse. The long negative part of $\Delta T/T$ , which lasts from tens of picoseconds to nanoseconds, is due to the intraband absorption of the probe pulse by the photoexcited carriers. The time scales exhibited in the long negative part of $\Delta T/T$ are temperature independent. (c) The magnitude of long negative $\Delta T/T$ transients are plotted on a log scale to show the dependence of the time scales on the layer number. Different curves are scaled in magnitude for clarity. Pump fluence was $32 \mu\text{J}/\text{cm}^2$ in all measurements. . .	96
6.5	Pump fluence dependent OPOP experiments of a 10-layer MoS <sub>2</sub> sample. (a) (Dots) Measured differential transmission transients $\Delta T/T$ of a 10-layer MoS <sub>2</sub> sample are plotted for different values of the pump fluence (4, 8, 16, $32 \mu\text{J}/\text{cm}^2$ ). T=300K. (Solid lines) Theoretical model for electron-hole recombination by defect-assisted processes in which carrier capture by defects occurs via Auger scattering. (b) The observed inverse carrier lifetime $1/\tau$ right after photoexcitation scales linearly with the photoexcited carrier density and, therefore, with the pump fluence. The recombination model fits the data very well. The vertical offset in the data at zero pump fluence is attributed to the light n-doping in our sample. . . . .	100

6.6	Carrier lifetime model. (a) (Dots) Carrier lifetime $\tau$ , extracted from the data in Figure 6.4(c), is plotted as a function of the number of layers. For each data point the pump fluence used was $32 \mu\text{J}/\text{cm}^2$ and $T=300\text{K}$ . (Solid lines) Theoretical model. The evolution of the carrier lifetime with the number of layers can be explained well by the competition between surface and bulk recombination, as explained in the text. The errorbars represent upper and lower bounds of the extracted lifetimes. (b) A depiction of the different recombination times in the bulk and at the surfaces of a few-layer $\text{MoS}_2$ sample. The solid line shows the probability density associated with the carrier envelope wavefunction in the few-layer sample. . . . .	102
6.7	Defect refilling dynamics of a 10 layer sample. (a,b) Pump fluence dependent defect refilling dynamics at room temperature. The dynamics was obtained by extracting away the simulated free carrier dynamics. The defect refilling dynamics has a super-linear dependence on the pump fluence. (c,d) The temperature dependent defect refilling dynamics shows that, there is a thermal activation energy for defect refilling, which is $\sim 200 \text{ K}$ . . . . .	106
7.1	SAW and BAW devices. . . . .	110
7.2	Real, imaginary and magnitude of $A_{osc}(\omega)$ . . . . .	112
7.3	Definition of Q in frequency domain. $Q = \omega_o/\Delta\omega = 1/2 \times \omega_o\tau$ . . . . .	113
7.4	BAW MEMS dominate the market of high frequency RF applications. BAW resonator, as illustrated in Figure 7.1, are used as the IEEE symbol for all crystal oscillators. . . . .	114
7.5	High frequency MEMS challenges. (a) It is very difficult to fabricate MEMS devices operating beyond 10 GHz with a good frequency-quality factor product (FQ)[157]. The dashed lines are theoretical maximum FQ products of AlN, Si and Quartz ( $1 \sim 2 \times 10^{13} \text{ Hz}$ ). (b) Quality factor Q drops rapidly as the MEMS devices shrink in size.[132] . . . . .	115
7.6	Rigid layer motions of few-layer $\text{MoS}_2$ . (a) Coherent optical phonon oscillations: adjacent layers move in opposite directions. (b) Coherent acoustic phonon oscillations: adjacent layers move in the same direction. . . . .	117
7.7	Several examples of reported coherent phonon oscillations[24, 80, 25, 179, 101, 144]. Whereas coherent optical phonon oscillations can be excited and observed in bulk materials, coherent acoustic phonon oscillations can only be excited if the wavelength of the excited acoustic phonon is well defined. For example, the acoustic oscillation wavelength is determined by the InGaN/GaN quantum well structure [144]. . . . .	119

7.8	The first demonstrations of optical pulse induced coherent acoustic phonon oscillations. Data was reported by Fayer <i>et al.</i> [130, 104, 105]. . . . .	121
7.9	Coherent acoustic phonon oscillations can be excited by applying ultrafast optical pulses on nanostructure gratings[144, 87]. . .	122
7.10	Acoustic pulse can be created by surface heat/stress pulse[152]. The acoustic echos (reflected acoustic pulses) were be observed in the transient reflection data. . . . .	123
7.11	Coherent optical phonons created by a surface space-charge field. Coherent longitudinal optical phonon oscillations of <i>GaAs</i> can be excited by applying ultrafast optical pulses [25, 75, 33]. Note that the oscillation phases differ by $180^\circ$ between the N-doped sample and P-doped <i>GaAs</i> samples. . . . .	124
7.12	Experimental set-up and measured coherent oscillation transients. (a) Nondegenerate ultrafast OPOP experimental set-up. (b) Coherent oscillations are observed along with the ultrafast defect and carrier dynamics, which were discussed in Chapter 4, 5, 6 and by the authors [168, 164, 162, 142, 167]. . . . .	130
7.13	Extracted frequency-thickness dispersion of the measured coherent oscillations. (a) Frequencies, lifetimes and phases of the coherent oscillations are obtained by subtracting the background defect and carrier dynamics. The extracted transient data (dots) can be fit by $\cos(\omega t)\exp(-t/\tau)$ (curves) very well. (d) The frequency dispersion of the coherently excited oscillations (circles with error bars) matches the Raman data (red dots) and 1D chain model (line) of out-of-plane rigid layer breathing mode in few layer $\text{MoS}_2$ very well [189]. Error-bars represents the upper and lower bounds of extracted frequency for each measurement. . . .	131
7.14	Out-of-plane (OOP) rigid layer breathing mode. The arrows depict the oscillation amplitude and direction of each layer in a 5-layer $\text{MoS}_2$ (fundamental mode). . . . .	132
7.15	OPOP transients by 1.37 and 1.57 <i>eV</i> probes. (a,b) Measured coherent rigid-layer LA phonon oscillations with different pump and probe wavelengths. No significant difference was observed between the 1.37 <i>eV</i> probe experiment(a) and the 1.57 <i>eV</i> probe experiment(b). The 17 <i>nm</i> thick $\text{MoS}_2$ sample has a bandstructure very similar to bulk $\text{MoS}_2$ , which has an indirect-gap at $\sim 1.3$ <i>eV</i> . The experiment shows that the coherent oscillations are detected by the probe beam through index oscillations. Indirect-gap Pauli-blocking of the probe beam has little contribution to the $\Delta T/T$ oscillation. Experiments were done at $T = 300$ <i>K</i> with pump fluence of $32\mu\text{J}/\text{cm}^2$ . . . . .	134

7.16	Pump fluence and temperature dependent oscillation lifetime. Pump fluence(a) and temperature(b) dependent oscillation lifetime on an 8 layer sample. The labels refer to the time sequence of the experiments, and a continuous degradation of oscillation lifetime was observed as a function of accumulated laser exposure time. No observable pump fluence and temperature dependence was found. Error-bars represent the upper and lower bounds of the extracted lifetime for each measurement. . . . .	139
7.17	Quality factor Q and FQ products of few layer MoS <sub>2</sub> samples. (a) The quality factors (Q) of the measured samples do not have a dependence on the sample thickness. The statistical distribution of the quality factors is plotted in the inset, and the distribution can be fit well by a "log-normal" function. Error-bars represent the upper and lower bounds of the extracted Q for each measurement. (b) The FQ product of few-layer MoS <sub>2</sub> can reach over $1 \times 10^{13}$ Hz in a 3 layer MoS <sub>2</sub> sample with an oscillation frequency of ~860 GHz. . . . .	140
A.1	Substrate preparation for exfoliation. Within each die, it is recommended to have both alignment keys (for lithography) and coordinate marks (for CAD design). . . . .	143
A.2	Scotch tape exfoliation method.(1) Prepare a one inch long piece of Scotch tape (facing up) with two folded-ends. (2) Fasten the Scotch tape to the table. (3) Place bulk crystal to the Scotch tape. (4) Use another Scotch tape (same in dimension) to start exfoliating the bulk crystal. (5,6,7) Perform exfoliation until thin bulk crystals fill the entire tape. (8) Peel off the Scotch tapes from each other and fasten them onto the table. (9) Perform tape-to-tape exfoliation until reaching the optimum thickness for exfoliation. The fraction numbers refer to the relative thickness of the tape. (10) Take one tape (1/8 thickness in this case). (11,12) Place it onto the target substrate. (13) Put more tape on top of the exfoliation tape to protect it from breaking. (14) Apply pressure to the tape on the substrate with a pen for a few minutes. (15,16) Hold the substrate from one end and slowly peel off the exfoliation tape with a small angle and steady force. . . . .	145

A.3	PDMS exfoliation method. (1) Cut one-inch square PDMS PF film (Gel-Pak). (2) Peel off the front plastic cover, then peel off PDMS film. (3) Place the PDMS film onto a clean microslide, which must be dust free. (4) Make sure there are no bubbles underneath the PDMS. (5) Place bulk crystal onto the PDMS film. (6) Prepare another microslide with PDMS film. (7) Exfoliate the bulk crystal between the PDMS films. (8) Exfoliate till the PDMS film is filled with thin bulk crystals. (9) Peel off the PDMS film from the microslide. (10) Place the PDMS film onto the target substrate. (11) Press the PDMS film on the target substrate for several minutes before peeling it off. . . . .	146
A.4	E-beam lithography on a quartz substrate. The lightning strikes on the PMMA are due to the sudden discharge of the accumulated electrons on the quartz wafer. . . . .	147

# CHAPTER 1

## INTRODUCTION TO LAYERED MATERIALS

### 1.1 Layered two-dimensional materials

Since the discovery of graphene [108], over one hundred different kinds of two-dimensional (2D) materials have been found, including boron-nitride [119], transition metal dichalcogenides [94], black phosphorus [82], silicene [160], germanene [9], the family of layered oxides [91], *etc.* Till today, 2D and layered material researchers have explored nearly all of the potential applications that one can imagine: micromechanical Systems [158], transistors [169], photodetectors [72], solar cells [86], lasers [174], batteries [68], superconductors [20], magneto memories [1], sensors [123], water filtering and drug delivery devices [28, 88], *etc.*

The aforementioned materials and applications just represent a small part of the vast 2D and nanomaterial research field. At present, the field of 2D and nanostructured materials is so large that it is no longer possible to provide a concise review chapter. Instead, readers are encouraged to read review articles such as [49, 134, 2, 170, 13]. Here, we only provide a very brief introduction to the basic properties of the two 2D materials that my Ph.D. research has focused on: graphene and MoS<sub>2</sub>.

Graphene and MoS<sub>2</sub> crystal structures are shown in Figure 1.1. Differing from graphene, which consists of a single layer of carbon atoms in the honeycomb configuration, monolayer MoS<sub>2</sub> consists of three layers of atoms: two layers of sulfur atoms sandwich a layer of molybdenum atoms. The thickness of

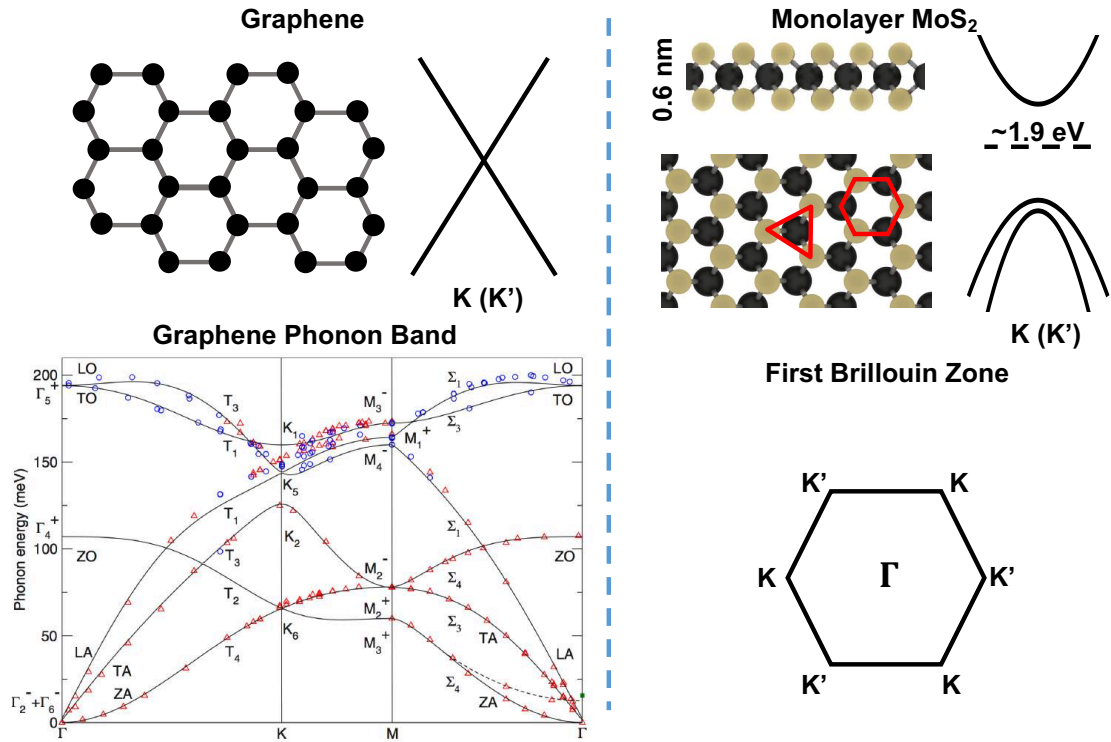


Figure 1.1: Graphene and monolayer MoS<sub>2</sub>. Whereas graphene consists of a single layer of carbon atoms in the honey-comb configuration, monolayer MoS<sub>2</sub> has three layers of atoms. The unit cell of monolayer MoS<sub>2</sub> can be drawn in two different but equivalent ways: a triangular or a hexagonal configuration. Graphene is a semi-metal with zero bandgap and linear band dispersion; monolayer MoS<sub>2</sub> is a 2D direct bandgap semiconductor with exciton photoexcitation energy at  $\sim 1.9$  eV. Note that monolayer MoS<sub>2</sub> has spin-degenerate conduction bands. The graphene/graphite phonon band is given by Mohr2007 *et al.* [102].

graphene is  $\sim 0.3$  nm and the thickness of monolayer MoS<sub>2</sub> is  $\sim 0.6$  nm [108, 94]. Whereas graphene is a zero bandgap semi-metal, monolayer MoS<sub>2</sub> has direct bandgap with exciton photoexcitation energy at  $\sim 1.9$  eV [94]. The unit cell of monolayer MoS<sub>2</sub> can be drawn in two different but equivalent ways: a triangular or a hexagonal configuration as shown in Figure 1.1. For both graphene and monolayer MoS<sub>2</sub>, the atoms are at the corners of the hexagonal unit cells,

TMDs Q. E	Device	Reference
0.1%	WSe <sub>2</sub> photodetector	Zhang, Iwasa, <i>et al.</i> [187]
< 0.01%	MoS <sub>2</sub> electroluminescence	Sundaram, Steiner, <i>et al.</i> [147]
0.1%	MoS <sub>2</sub> photoluminescence	Wang, Rana, <i>et al.</i> [168]
0.1%	WSe <sub>2</sub> electroluminescence	Ross, Xu, <i>et al.</i> [128]
0.1 ~ 1%	MoS <sub>2</sub> /Graphene photodetector	Bernadi, Grossman, <i>et al.</i> [6]
0. ~ 1.5%	WSe <sub>2</sub> /MoS <sub>2</sub> p-n photodetector	Furchi, Mueller, <i>et al.</i> [44]
0.02%	MoS <sub>2</sub> gated p-n photodetector	Baughner, jarillo-Herrero, <i>et al.</i> [4]

Table 1.1: Quantum efficiency of direct gap transition metal dichalcogenides (TMDs).

making  $K(K')$  of the First Brillouin Zone the most interesting parts of the band-structures.

Due to the extremely strong carbon-carbon bond, graphene has large optical phonon energies ( $\sim 200$  meV [102] see Figure 1.1). The large optical phonon energies in graphene turn out to be the major bottleneck for hot carrier cooling as discussed in Chapter 3. Direct gap semiconducting monolayer transition metal dichalcogenides (TMDs), such as monolayer MoS<sub>2</sub>, MoSe<sub>2</sub> and WSe<sub>2</sub>, are promising for many optoelectronic applications. However, they all suffer from very low quantum efficiency as shown in Table 1.1. Defect assisted electron-hole recombination dynamics and the potential device applications of monolayer and few layer MoS<sub>2</sub> are discussed in Chapter 4, 5, 6 and 7.

Unique mechanical, electrical and optical properties of 2D layered materials are not the only reasons driving the 2D research into its second decade. The real advantage of layered materials is that, potential devices can be designed to function on a variety of substrates, or be controlled by surface engineering. As in Figure 1.2, 2D heterostructures can be formed by transfer techniques instead of growth. The transfer techniques do not have the challenges that the tra-

ditional heterostructure growth technologies need to solve: defect control and lattice matching issues. Furthermore, 2D materials are flexible by nature, and can perfectly conform to flexible substrates, allowing them to bend and twist together with the substrates. In addition, as 2D materials have the ultimate surface to volume ratio, their material properties can be efficiently manipulated by surface engineering.

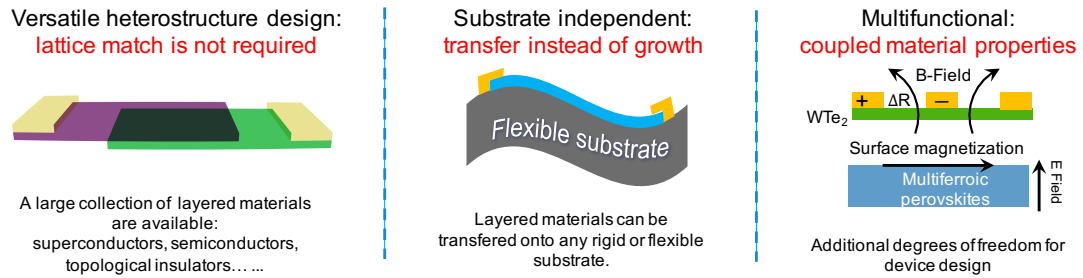


Figure 1.2: The advantages of layered 2D materials.

The goal of nanomaterial research is to exploit unique properties of emerging materials, and find the corresponding niche market applications. Given that the market demands and requirements are so diversified, it is always desirable to use the most suitable material for the specific application.

## 1.2 Experimental techniques

Two-dimensional layered materials are studied by different tools and techniques at the Cornell Optoelectronics Lab. I chose to specialize in ultrafast time resolved spectroscopy because it is informative, versatile and precise. As in Figure 1.3, with simple extensions, an ultrafast pulsed laser can stimulate

and probe myriad materials with a wide range of photon energies from infrared to ultraviolet. In addition, real time material response can be recorded by various techniques: optical/infrared differential transmittance/reflectance, broad band THz absorption/emission, photoluminescence, Raman, photovoltage/photocurrent correlation, magneto-optic effect, photoemission, spin echo, etc. A few commonly used techniques are illustrated in Figure 1.3. Because each of the aforementioned detection techniques addresses a different physical process or a distinct aspect of relaxation dynamic, ultrafast time resolved spectroscopy proves to be precise and versatile.

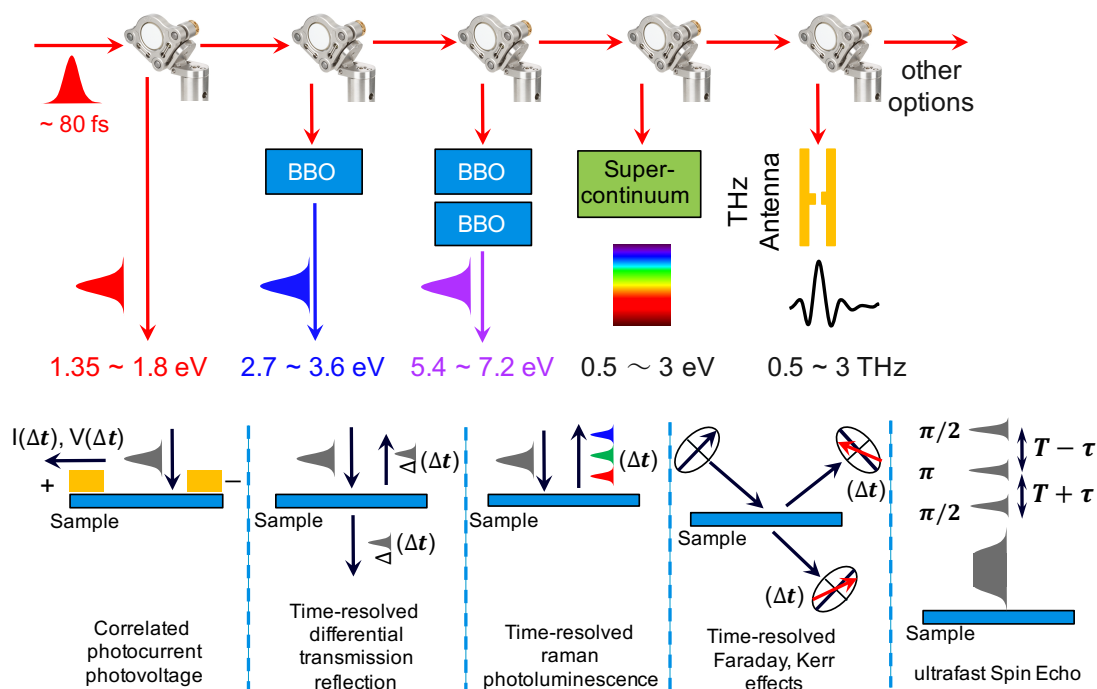


Figure 1.3: Versatility of ultrafast spectroscopies.

Equilibrium and quasi-equilibrium material properties can be studied by broad band confocal optical spectroscopies, such as transmission/reflection, Raman and PL measurements. We also have the capability of performing optical

spectroscopy experiments in the mid-IR to far-IR range by using FTIR (Fourier Transform IR) spectroscopy. Optical spectroscopies can be combined with electrical measurements as well: electrical transport and spectrum-resolved photoconductivity measurements on fabricated 2D devices can be performed on our home-built confocal systems. The details of the experimental configurations are discussed in Chapter 2.

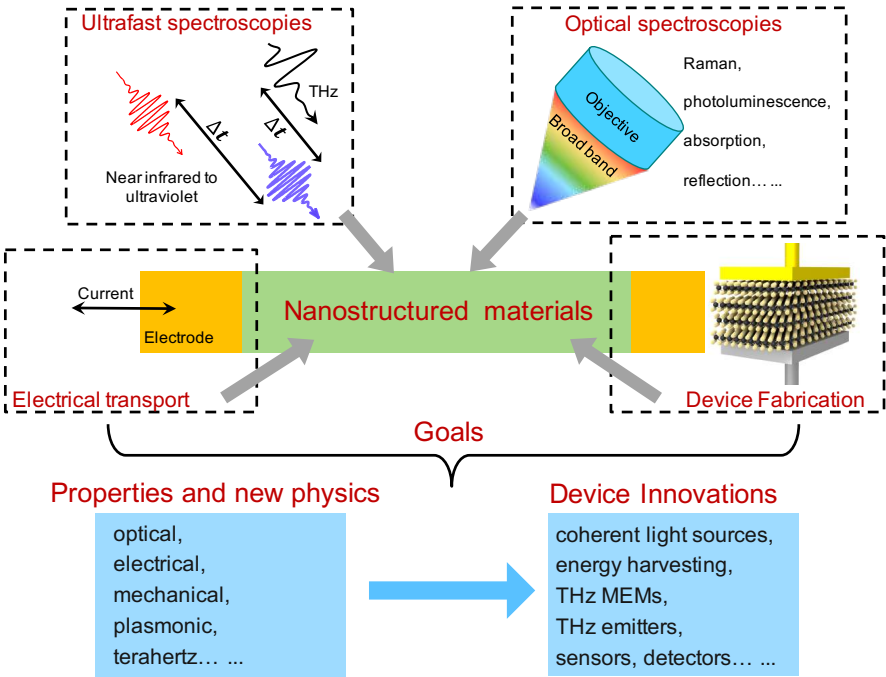


Figure 1.4: Nanostructured material research approach.

To summarize, our research approach is illustrated in Figure 1.4. By fabricating devices based on 2D and nanostructured materials, and using electrical transport and optical spectroscopy tools, our goal is to study the optical, electrical, mechanical, plasmonic, and terahertz properties of nanostructured materials for device applications.

CHAPTER 2  
CHARACTERIZATION OF LAYERED MATERIALS

## 2.1 Introduction

Optical spectroscopy tools offer quick and non-invasive characterization of nanostructured materials. A confocal spectroscopy system is shown in Figure 2.1. This system is designed to perform transmission/reflection, Raman and photoluminescence spectroscopies in the UV to near-IR range. For the transmission and reflection measurements, a pinhole is used to select the transmitted/reflected light from micron-sized samples at the microscope image plane. When electrical measurements are combined with optical excitation, wave-

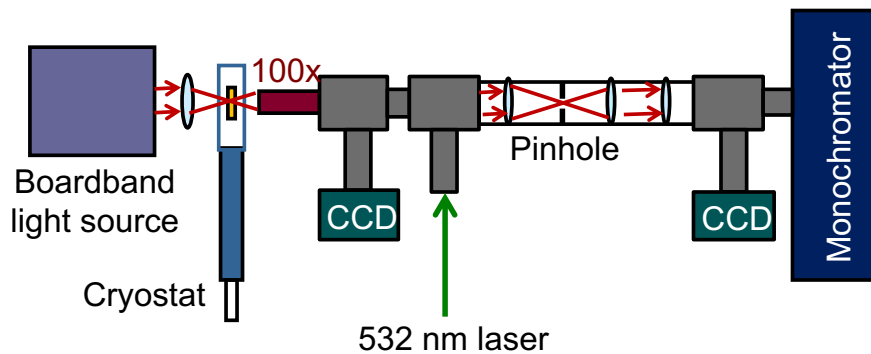


Figure 2.1: A confocal microscopy system for transmission, reflection, photoluminescence and Raman spectroscopies. The pinhole is used to select the transmitted/reflected light from micron-sized samples at the microscope image plane.

length dependent photoconductivity response can be measured as well. The goal of this chapter is to make a simple and practical introduction to the spectroscopy methods used in the Cornell Optoelectronics Lab.

## 2.2 Spontaneous and stimulated Raman scattering

Raman spectroscopy is a commonly used optical characterization technique, however, a good introductory discussion on the physics of spontaneous and stimulated Raman scattering processes is difficult to find. In this section, the symmetry requirement and the  $1/\lambda^4$  dependence of the Raman scattering intensity will be derived in a phenomenological way [111]. Because our research focuses on lattices, not molecules, the discussion does not include rotational Raman scattering processes.

The material polarization  $P$  due to the presence of an electromagnetic field  $E$  can be described in terms of the material susceptibility  $\chi$  or dipole moment  $\mu$  :

$$P = \epsilon_0 \chi(Q(t)) \cdot E(t) \quad (2.1)$$

$$P = N\mu(t) \quad (2.2)$$

$$\mu(t) = -e \cdot r(t) \quad (2.3)$$

$$\mu(t) = p(Q(t)) \cdot E(t) \quad (2.4)$$

where the dipole moment  $\mu(t)$  can be defined as the product of the electron charge  $e$  and the electron displacement  $r(t)$ , or,  $\mu(t)$  can be defined as the polarizability  $p(Q(t))$ , which itself is a function of the atomic configuration  $Q(t)$ .  $N$  is the total number of excited dipoles. Hence one can choose to discuss the Raman scattering based on susceptibility  $\chi$ , polarizability  $p$ , or dipole moment  $u(t)$ . The polarizability  $p$  can be expanded around the equilibrium atomic configuration  $Q_o$ :

$$p = p_o + \partial p / \partial Q_o \times Q(t) \quad (2.5)$$

Now let's make two other assumptions: (1) the electromagnetic field oscillates

at frequency  $\omega$ :  $E = E(\omega) \cos(\omega t)$  (2) the atomic configuration  $Q$  oscillates at frequency  $\omega_q$ :  $Q = Q(\omega_q) \cos(\omega_q t)$ . Hence we have:

$$P = N \times \{p_o + \partial p / \partial Q_o \times Q(\omega_q) \cos(\omega_q t)\} \times E(\omega) \cos(\omega t) \quad (2.6)$$

The second term of Eq.2.6 contains the Raman scattering process:

$$P_{Raman} = N \times \partial p / \partial Q_o Q(\omega_q) E(\omega) \times \{ \cos((\omega_q + \omega)t) + \cos((\omega_q - \omega)t) \} \quad (2.7)$$

Note that we have two new frequency components:  $\omega - \omega_q$  is called the Stokes shift, and  $\omega + \omega_q$  is called the anti-Stokes shift. And thus the dipole moment is:

$$\mu_R(t) = \partial p / \partial Q_o Q(\omega_q) E(\omega) \times \{ \cos((\omega_q + \omega)t) + \cos((\omega_q - \omega)t) \} \quad (2.8)$$

To determine the Raman scattering strength, we need to evaluate the radiation field strength of this dipole moment. In the far field, the integrated energy flux of an oscillating dipole is given by Jackson[60]:

$$I_\mu = \frac{N\omega^4}{12\pi\epsilon_o c^3} |\mu_R|^2 \quad (2.9)$$

The above result shows that the Raman efficiency scales as the fourth power of the frequency  $\omega$ . Last but not least, the above derivation does not consider energy and momentum conservation. To conserve energy and momentum, a scattered electromagnetic field is required, and we can rewrite the Raman scattering energy flux as:

$$I_\mu = \frac{N\omega^4}{12\pi\epsilon_o c^3} |E(\omega)|^2 |\vec{e}_i \cdot \partial p / \partial Q_o Q(\omega_q) \cdot \vec{e}_s|^2 \quad (2.10)$$

where  $\vec{e}_i$  and  $\vec{e}_s$  are the polarization vector of the incident and scattered electric field respectively, and the Raman tensor is given by:

$$R = \partial p / \partial Q_o Q(\omega_q) \quad (2.11)$$

which is a second rank tensor and defines the selection rule of the spontaneous Raman scattering. As we can see from the above derivation, the intensity of the spontaneous Raman scattering scales linearly with the intensity of the incident radiation. However, if the scattered radiation field is provided by an external source, *i.e.* in **stimulated** Raman scattering, the intensity of the Raman scattering scales linearly with the intensity product of the incident and scattered radiation.

Both optical and acoustic phonons can be excited through Raman processes as long as Eq. 2.10 is non-zero. In most cases, spontaneous Raman scattering is used to determine the frequency (energy) of a particular phonon mode, and energy difference between the excitation photon and Stokes-shifted photon is the phonon energy.

Infrared absorption spectroscopy is another commonly used method in studying phonon vibration modes of a crystal. However, the quantum selection rules of infrared absorption and Raman scattering processes are different. The fundamental difference is that, in infrared absorption, the dipole moment  $\mu$  oscillates at the same frequency as the driving electric field. Instead of the requirement of a non-zero polarizability (Eq. 2.5) as in Raman processes, the phonon vibration itself results in an oscillating dipole. Thus IR active phonon mode requires a non-zero dipole moment derivative  $\partial\mu/\partial Q_o$  (**not through the polarizability in Eq. 2.5**), while a Raman active phonon mode requires non-zero polarizability derivative  $\partial p/\partial Q_o$ . Sometimes non-zero  $\partial\mu/\partial Q_o$  and  $\partial p/\partial Q_o$  are called the **gross selection rule**.

Interestingly, the symmetry requirements of non-zero  $\partial\mu/\partial Q_o$  and  $\partial p/\partial Q_o$  are different. It is easier to discuss Raman and infrared absorption selection rules in terms of the symmetry of quantum transitions[153, 54]. The quantum transition

of infrared absorption can be expressed as:

$$T_{IR} \propto \left| \int \psi_f \times \mu \times \psi_i dx_i dx_f \right|^2 \quad (2.12)$$

where  $\psi_i$  is the quantum ground state,  $\psi_f$  is the excited state, and  $\mu$  is the dipole moment. Because the ground state  $\psi_i$  has the full symmetry of the crystal, the multiplication  $\mu \times \psi_i$  has the same symmetry as the dipole moment  $\mu$ , which can be decomposed into  $x$ ,  $y$  and  $z$  components. Thus  $T_{IR}$  is non-zero only if the excited state  $\psi_f$  is invariant under operation  $x$ ,  $y$  or  $z$ . On the other hand, the Raman selection rule is determined by the second rank tensor of polarizability  $p$ :

$$T_R \propto \left| \int \psi_f \times p \times \psi_i dx_i dx_f \right|^2 \quad (2.13)$$

Because the matrix elements of the second order polarizability tensor  $p$  have the same symmetry as the direct product of two vectors, which consists of  $xy$ ,  $xz$ ,  $yz$ ,  $x^2$ ,  $y^2$  and  $z^2$ , the Raman active phonon mode  $\psi_f$  must be invariant under symmetry operation  $xy$ ,  $xz$ ,  $yz$ ,  $x^2$ ,  $y^2$  or  $z^2$  in order to have non-zero  $T_R$ . The full quantum treatment of Raman scattering [153, 90] produces the same symmetry representation of the polarizability  $p$ .

Given that the final state  $\psi_f$  cannot simultaneously satisfy symmetry requirements of infrared absorption and Raman scattering processes, **a lattice phonon mode is either IR active or Raman active**. Fortunately, the symmetry operations of common crystals are already known, and look-up tables can be used to identify the invariant symmetry operations of the interested phonon modes. For example, graphene belongs to point group  $D_{6h}$ [154, 3], the characterization table, and the phonon modes are illustrated in Figure 2.2.

In the characterization table of graphene,  $A_{1g}$  phonon mode is the breathing mode in in the Figure 2.2(c). The  $A_{1g}$  mode satisfies the symmetry selec-

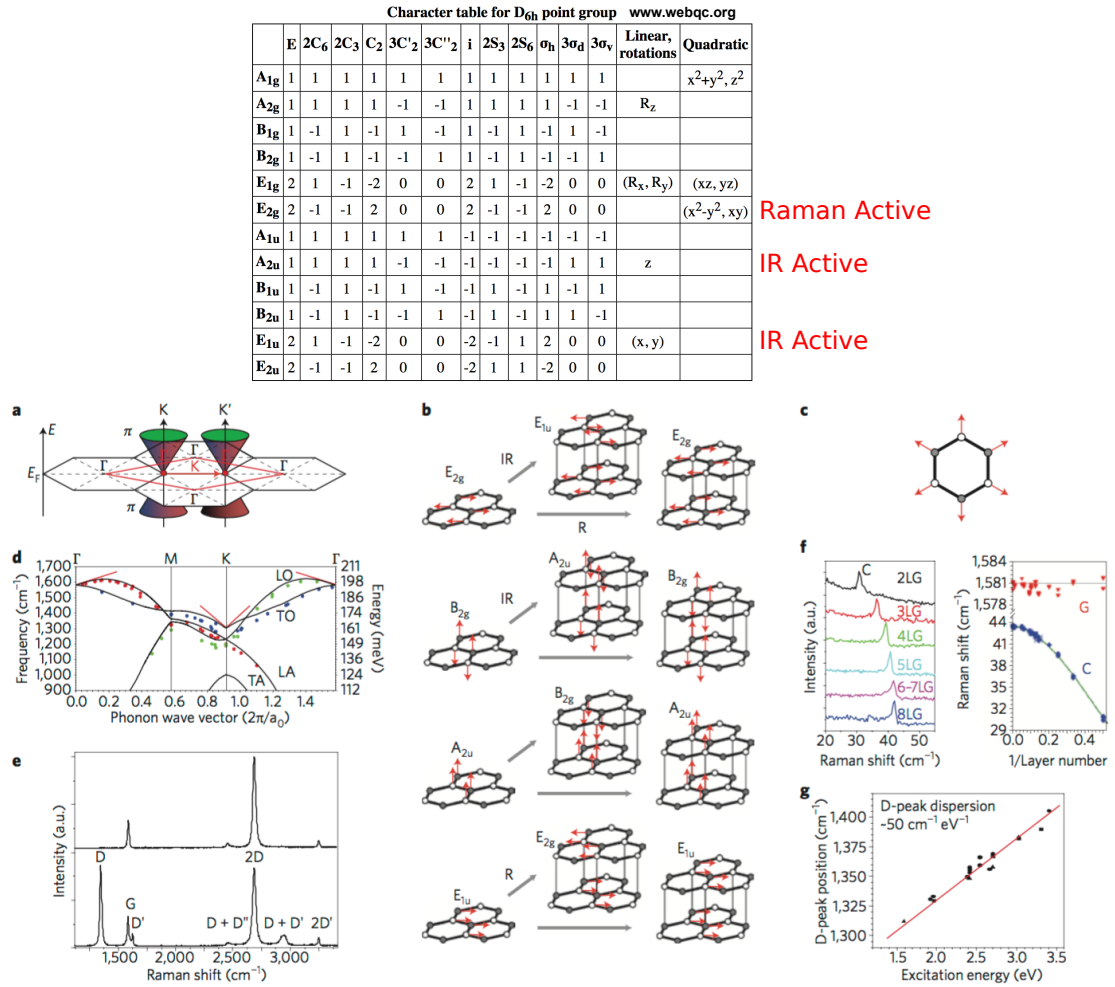


Figure 2.2: Characterization table and phonon modes of graphene [154, 3].

tion rule of Raman scattering. However, the  $A_{1g}$  mode does not satisfy the *gross selection rule* for a graphene lattice that extends to infinity, because the net polarizability is zero. Only graphene with finite grain sizes can have a non-zero polarizability, arising from the grain boundaries. Thus the  $A_{1g}$  mode is a signature of lattice grains and defects in graphene, and shows up as the  $D$  peak at  $\sim 1350 \text{ cm}^{-1}$  in the Raman spectrum. The  $A_{2g}$  and  $E_{1g}$  modes relate to the rotations of a molecule and do not exist in a lattice. The atomic motions of the  $A_{2u}$  and  $E_{1u}$  phonon modes are plotted in Figure 2.2, and they are IR active as

expected. The only Raman active mode is the  $E_{2g}$  mode, which peaks at  $\sim 1580 \text{ cm}^{-1}$  (G peak) in the Raman spectrum. The above crystal symmetry analysis explains the presence of D and G peaks in the Raman spectrum, but cannot explain the presence of  $D'$ ,  $2D$ , and other peaks. To understand Raman peaks at phonon energies consisting of a combination of different phonon modes, a higher order Raman theory with a full quantum treatment is required[95].

### 2.3 Confocal transmission and reflection measurements

Both the real and imaginary parts of optical conductivity can be directly extracted from transmission and reflection measurements. The optical conductivity extraction for layered two-dimensional (2D) materials is particularly simple. Because 2D materials have thicknesses much shorter than the optical wavelength (a few nanometers vs. a few hundred nanometers), they can be treated as a conductive boundary condition for the substrate they sit on.

In Figure 2.3, the broadband light transmits through the substrate with refractive index  $n_1$ , and has electric and magnetic field amplitude  $E_1$  and  $H_1$  respectively. At the substrate/air interface, the reflected E/H field is  $E_2/H_2$  and the transmitted E/H field is  $E_3/H_3$ ,  $k$  is the wave vector that represents the direction of light propagation. The same definition applies to the reflected fields as well. The boundary conditions for the transmission measurement are:

$$E_1 + E_2 = E_3 \quad (2.14)$$

$$E_1/\eta_1 - E_2/\eta_1 - E_3/\eta_0 = \sigma E_3 \quad (2.15)$$

where  $\eta_1$  and  $\eta_0$  are substrate and vacuum impedance respectively, and  $\sigma$  is the complex 2D optical conductivity of the material. By solving these two equa-

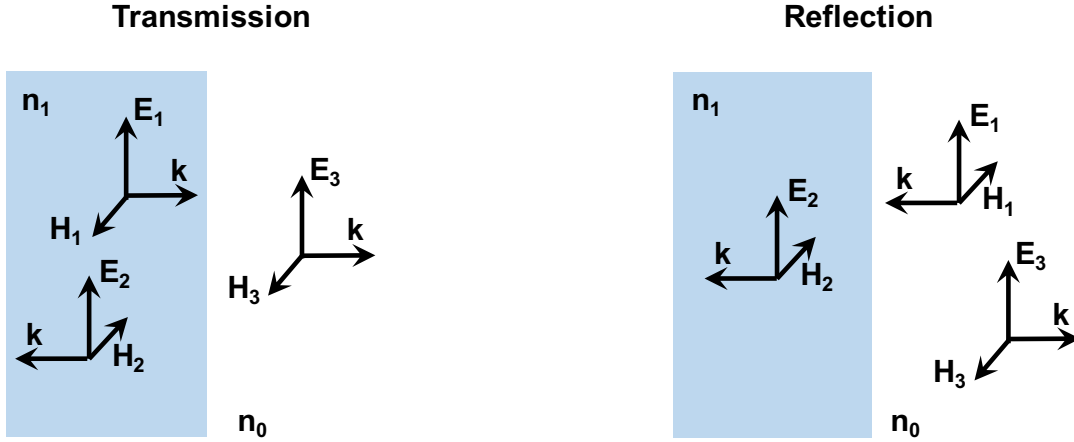


Figure 2.3: The reflection and transmission measurement. Electric and magnetic field definitions in transmission and reflection configurations.

tions, the transmission of the incident light through the sample is:

$$T_s = \left| \frac{E_3}{E_1} \right|^2 = \frac{4n_1^2}{(\sigma_r \eta_0 + 1 + n_1)^2 + \sigma_i^2 \eta_0^2} \quad (2.16)$$

where  $\sigma_r$  and  $\sigma_i$  are the real and imaginary part of the optical conductivity respectively. The transmittance  $T$  is defined as  $T_s/T_o$ , where  $T_o$  is the transmission through the substrate:

$$T = T_s/T_o = \frac{(1 + n_1)^2}{(\sigma_r \eta_0 + 1 + n_1)^2 + \sigma_i^2 \eta_0^2} \quad (2.17)$$

The reflectance  $R$  can be obtained in the same way:

$$R = R_s/R_o = \frac{(1 + n_1)^2 (1 - n_1 - \sigma_r \eta_0)^2 + \sigma_i^2 \eta_0^2}{(1 - n_1)^2 (\sigma_r \eta_0 + 1 + n_1)^2 + \sigma_i^2 \eta_0^2} \quad (2.18)$$

By observing the expression of  $T$  and  $R$ , we can rewrite  $R$  in terms of  $T$ :

$$R = \frac{(1 + n_1)^2 - 4(n_1 + \sigma_r \eta_0)T}{(1 - n_1)^2} \quad (2.19)$$

Thus the real part of the optical conductivity  $\sigma_r$  can be expressed in terms of the transmittance  $T$  and reflectance  $R$ :

$$\sigma_r = \frac{(1 + n_1)^2 - (1 - n_1)^2 R}{4\eta_o T} - \frac{n_1}{\eta_o} \quad (2.20)$$

By correctly measuring the transmittance and reflectance with respect to the substrate, the complex optical conductivity can be directly extracted.

## 2.4 Broadband photoconductivity measurements

Optical conductivity can be measured by broadband photoconductivity experiment as well. The advantage of broadband photoconductivity measurement is that the experimental set-up is usually much simpler than the all-optical approach, and sometimes the sensitivity can be much higher — especially in the mid-IR to far-IR regime. The disadvantage is that the samples need to be fabricated into photodetectors. In this section, we will briefly go through broadband photoconductivity measurement configurations.

The broadband photoconductivity measurement set-up in Figure 2.4 is best for the UV to Near-IR range (from  $\sim 300 \text{ nm}$  to  $\sim 3 \mu\text{m}$ ). By rotating the optical grating in the spectrometer, the monochlor photoconductivity response is measured. The lock-in amplifier should be set to the current reading mode and phase-locked with respect to the optical chopper. The dark current of the photodetector under DC voltage bias is filtered out by the lock-in amplifier due to the amplitude modulation of the optical light at the chopping frequency. Generally, a higher chopping frequency is preferred because the photodetector flicker noise inversely scales with frequency.

For near-IR( $\sim 2\mu\text{m}$ ) to far-IR broadband photoconductivity measurements, Fourier Transform IR (FTIR) spectroscopy provides cleaner and faster measurements. In the FTIR configuration, the lock-in time constant must be set to a very small value compared to the FTIR mirror single-trip time. We normally consider

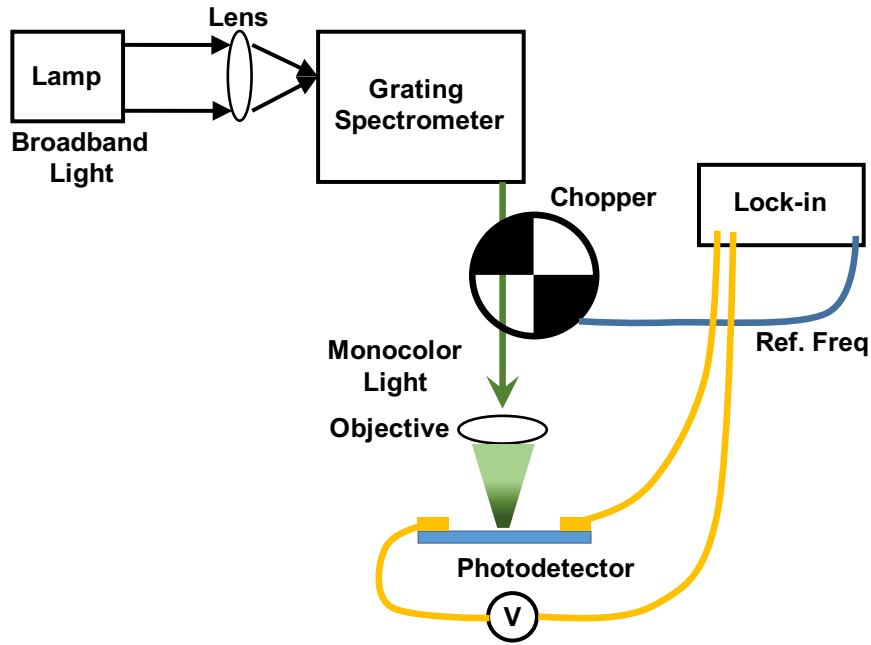


Figure 2.4: Broadband photoconductivity measurement configuration. The broadband light is dispersed into monochlor light by the grating spectrometer. In the current mode, the lock-in amplifier has  $1\text{ K}\Omega$  input resistance.

a lock-in amplifier output to be non-aliasing after three time constants, thus the upper limit of a valid FTIR spectrum output is:

$$F_{upper} = \frac{1}{3 \times V_{mirror} \times \tau_{lock-in}} \quad (2.21)$$

As long as the lock-in time constant is much smaller then the FTIR mirror single-trip time, the resolution of a measured photoconductivity spectrum is still set by the mirror travel distance as  $1/L$ .

## 2.5 Lock-in electrical transport measurement for linear devices

Most electrical transport experiments are performed by low noise source meters. Because graphene has a zero bandgap, graphene FETs behave like resistors

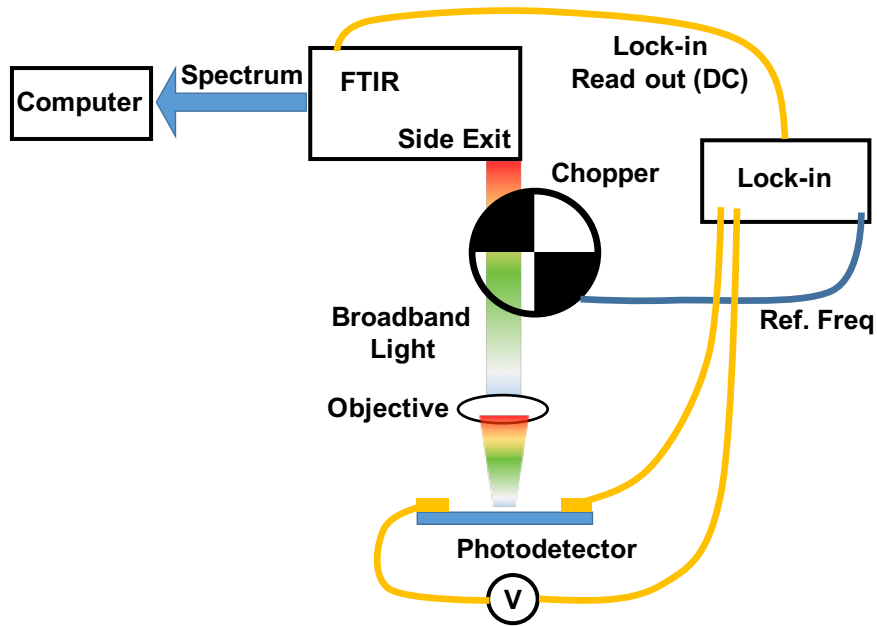


Figure 2.5: FTIR broadband photoconductivity measurement configuration. The DC lock-in output (the amplitude of the photodetector AC response) is fed back to FTIR. The product of lock-in time constant and the mirror velocity, which is the FTIR sampling distance without aliasing, determines the upper limit of the FTIR output spectrum.

under low drain-source bias, and the resistance is set by the back-gate bias. This resistive behavior allows for a more accurate electrical transport measurement technique. In this section, we will briefly discuss how to use two lock-in amplifiers to perform accurate transport measurements for graphene or other resistive devices.

In Figure 2.6, the voltage reference output port of the left lock-in amplifier serves as the low-noise voltage source to the four terminal device. The lock-in amplifier output frequency should be set according to the lock-in time constant setting. A general rule of thumb is that the output frequency should be set as:  $F > 3 \times 1/\tau$ ,  $\tau$  is the lock-in time constant. Because the device resistance is independent of the driving voltage in the linear region, we can use a resistor box

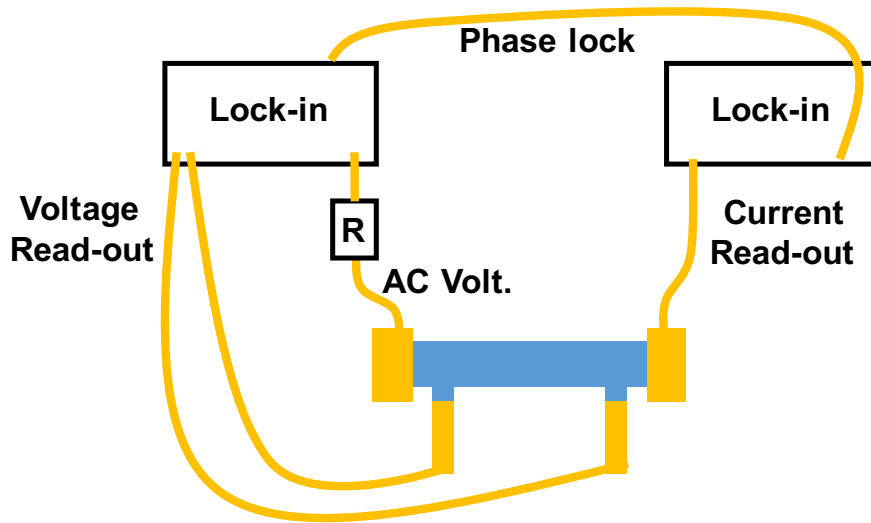


Figure 2.6: Lock-in amplifier transport experiment. The lock-in amplifier on the left side supplies an AC driving voltage and measures the channel voltage drop, while the lock-in amplifier on the right side is phase-locked to the other lock-in, and measures the channel current.

$R$  ( $\sim 10\text{ M}\Omega$  in Figure 2.6) to protect the device from being overloaded. With the left lock-in measuring the channel voltage drop, and the right lock-in measuring the channel current, the electrical transport experiment is done by sweeping the gate voltage.

## 2.6 S/N ratio optimization in ultrafast spectroscopies

Time-resolved ultrafast spectroscopy techniques are simple and easy to implement. However, straightforward ultrafast implementations suffer from low signal-to-noise (S/N) ratios, and can only reliably detect  $\sim 10^{-3}$  change in the probe reflectance or transmittance. The goal of this section is to explain several practical techniques, such that  $\sim 10^{-6}$  change in probe detection in the degenerate configuration, and  $\sim 10^{-8}$  change in probe detection in the non-degenerate

configuration can be obtained routinely without complicated balanced detection techniques.

The majority of the photodetection noise comes from the following sources, listed according to their relative importance: mode-lock quality, pump/stray light leakage, chopper noise, detector noise, lock-in noise, photon shot noise. Practically, photon shot noise is extremely small in comparison with other noise sources. Lock-in noise matters for probe detection beyond  $10^{-6}$  probe sensitivity. Chopper and detector noise might limit the probe detection sensitivity to  $10^{-5} \sim 10^{-6}$ . Bad pump/stray light leakage limits the probe detection sensitivity to  $10^{-2} \sim 10^{-3}$ , and without good mode-locking, ultrafast experiments cannot be performed.

There are two basic techniques to enhance S/N ratio of ultrafast spectroscopies: optical chopping and pump leakage minimization. The most basic optical chopping method is the single chopped configuration shown in Figure 2.7. Given that the pump light is completely filtered out, and only the probe beam can reach the photodetector diode, the differential reflectance or transmittance of the probe beam is modulated at the pump chopping frequency  $F_{pump}$  (the modulation is done by the sample), and can be picked up by a lock-in amplifier, which is phased locked at  $F_{pump}$ . The double chopped configuration in Figure 2.7 is commonly believed to have better pump leakage rejection. If the lock-in amplifier is phased locked at  $F_{pump} + F_{probe}$ , then perhaps the pump leakage at  $F_{pump}$  can be completely removed by the lock-in amplifier.

However, most of time, the double chopped configuration cannot provide better S/N ratio compared to the single chopped scenario. The reason is that the leaked pump light at  $F_{pump}$  can be mixed with the probe light at  $F_{probe}$  by

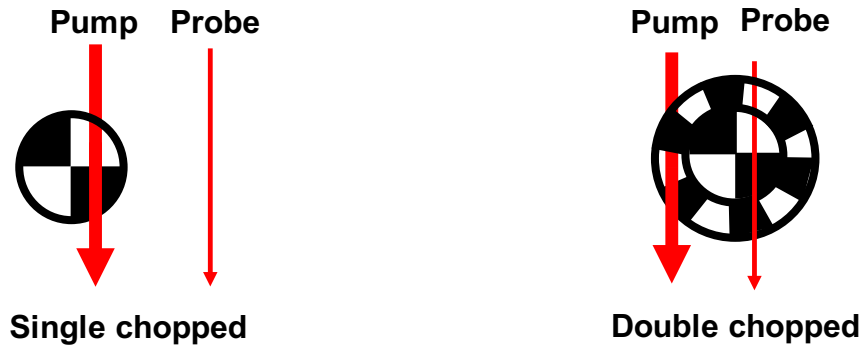


Figure 2.7: The single chopped and double chopped configuration.

the photodetector diode. The amplitude of the mixed signal at  $F_{pump} + F_{probe}$  is linearly proportional to the leaked pump light intensity.

Thus, for an unbalanced detection scheme, effort should be focused on the pump leakage reduction, not the chopping configuration. When the pump leakage is completely rejected, the double chopped configuration gives a signal at half the amplitude of the single chopped configuration (considering the sample as a mixer), with the same noise fluctuation (which is limited by electronic noise from the detector and lock-in amplifier). Ideally, the S/N ratio of a single chopped signal should be twice that of the double chopped configuration.

Pump leakage filtering techniques are illustrated in Figure 2.8. These techniques work for both non-degenerate and degenerate Optical-Pump Optical-Probe(OPOP) experiments. The majority of the pump beam is blocked by the iris and the razor blade as shown in Figure 2.8. Without the sample in place, the pump should be completely blocked after the iris. When the sample is in place, the sample scatters the pump beam such that a small amount of the scattered pump light closely follows the recollimated probe beam.

The remaining scattered pump beam is further filtered out by the long travel

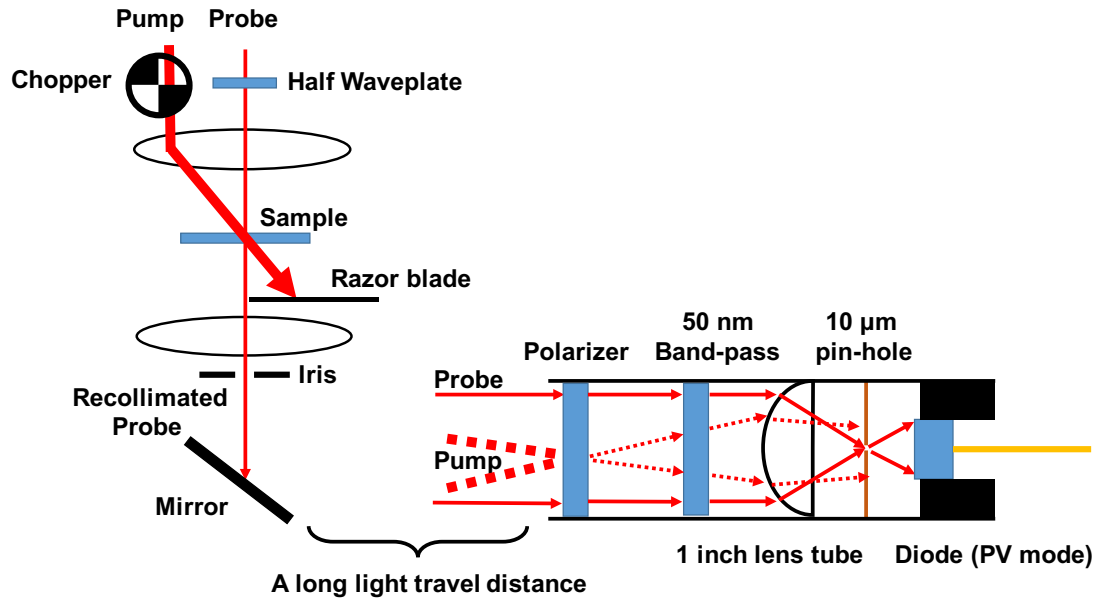


Figure 2.8: OPOP pump leakage filtering. The combination of optical and spatial filtering techniques can efficiently reject the pump beam leakage. By careful implementation of the illustrated filtering techniques, a single chopped OPOP measurement should provide a better S/N than the double chopped OPOP configuration.

distance between the detector stack and the mirror. The scattered pump light is then significantly attenuated by the polarizer, and eventually completely stopped by the  $10\mu\text{m}$  pinhole, which serves as the last stage spatial filter. The  $50\text{nm}$  band-pass filter is used to filter out the room light (also the pump in the non-degenerate scenario). If the above procedure is correctly implemented, without balanced detection, a  $10^{-6}$  probe detection sensitivity can be routinely achieved in the degenerate OPOP experiments, and a  $10^{-8}$  probe detection sensitivity is possible in the non-degenerate experiments. One easy way to test the pump leakage is to check if the lock-in reading is zero in the single chopped configuration when the probe beam is blocked. Note that this testing technique does not work for the double chopped configuration, as a large portion of the lock-in

reading comes from the pump-probe mixing at the photodetector diode. Thus blocking the probe beam results in a zero lock-in reading at the sum frequency regardless of how much the pump leakage is.

To minimize the chopper noise, it is best to use phased-locked optical choppers. There is an optimum chopping frequency that provides the best measurement S/N ratio. The electronic noise from the photodetector diode in Figure 2.8 can be minimized by using bare photodiode in its photovoltaic mode. The lock-in amplifier should always be set to the low-noise setting, and the detection phase should be set such that the probe signal is completely placed into one of the detection quadrature ( $x$  or  $y$ ), leaving the other quadrature to collect only noise. If an integration time constant beyond  $300\text{ ms}$  is required, averaging multiple fast scans provides a better S/N ratio and less signal drift than a single long scan.

Lastly, the two most commonly encountered OPOP experiment issues are: losing mode-lock and a bad overlapping between the pump and probe beams.

## 2.7 Spatially-resolved ultrafast measurements

Time-resolved non-local properties of nanostructured materials can be studied by ultrafast techniques as well. Many OPOP set-ups implement the  $4F$  configuration, in which the objective back-aperture is at the image plane of the beam-splitter as shown in Figure 2.9. In the  $4F$  configuration, the separation between the two optical beams is controlled by the incident angle of the beam that is reflected by the beam-splitter.

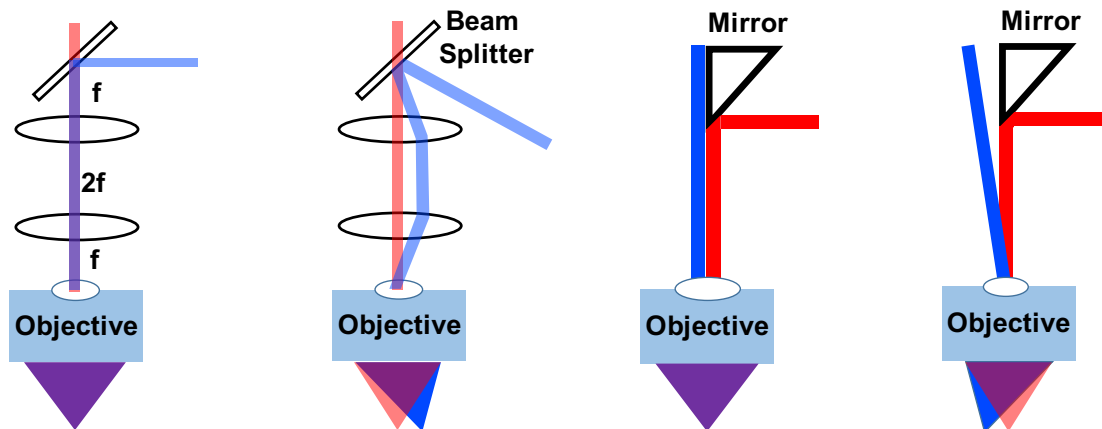


Figure 2.9: Non-overlapping OPOP experiment. The  $4F$  configuration has advantages in spatial resolution and flexibility, but suffers from interference problems at zero pump-probe delay.

The other possible configuration uses a prism mirror to bring the two beams as close to each other as possible. When the two beams are parallel, they focus at the same spot on the sample. The spatially resolved OPOP experiment is done by controlling the incident angle of one of the beams as shown in Figure 2.9. The advantage of the  $4F$  configuration is apparent: as high magnification and high numerical aperture (NA) objectives have very small back apertures, it is not possible to bring two parallel beams into an high NA objective in the prism mirror configuration. However, the  $4F$  configuration usually has interference spikes at the zero pump-probe delay. Although this problem can be mitigated by cross-polarizing the two beams, the prism mirror configuration is preferred if a clean measurement is the first priority in the OPOP experiment.

CHAPTER 3  
HOT CARRIER AND PHONON RELAXATION DYNAMICS IN  
GRAPHENE

### 3.1 Introduction

The performance of most demonstrated and proposed graphene-based electronic and optical devices depends critically on carrier and optical phonon scattering as well as relaxation dynamics [98, 149, 121, 176, 10]. Optical phonons in graphene can decay in two main ways as follows: (i) optical phonons can get absorbed by electrons or holes, or (ii) optical phonons can decay into other phonons via anharmonic interactions and lattice defects. In this letter, phonon lifetime refers to the lifetime due to the latter processes, the most important of which is the decay of an optical phonon into two acoustic phonons [14]. Optical phonon lifetimes in graphene can be estimated from frequency domain measurements, such as Raman spectroscopy. However, the measured Raman linewidths also contain contributions from pure dephasing processes and inhomogeneous broadening [139]. Direct measurement of the optical phonon lifetime in carbon nanotubes via time-resolved Raman anti-Stokes spectroscopy was performed by Song et al [139]. and a value of  $\sim 1.1$  ps was reported. Theoretical calculations of the hot optical phonon lifetimes in graphene due to anharmonic decay into acoustic phonons were carried out by Bonini et al. [14], and values between 23 ps were reported for both zone-center  $E_{2g}$  and zone-edge  $A_1'$  modes for phonon temperatures in the 500~900 K range. A much longer lifetime value of  $\sim 7$  ps was measured by Kampfrath et al [65]. via time-resolved measurements of the electronic temperature using optical-pump

<i>Sample</i>	$I_G/I_D$	$N$	$\tau_{ph}(ps)$	$n_o(cm^{-2})$
<i>A</i>	20.5	55	$2.55 \pm 0.08$	$1 \times 10^{11}$
<i>B</i>	57	16	$2.5 \pm 0.08$	$1 \times 10^{11}$
<i>C</i>	9.6	2	$2.55 \pm 0.1$	$6 \times 10^{11}$
<i>D</i>	19	$\sim 2$	$2.5 \pm 0.12$	$7 \times 10^{11}$

Table 3.1: Experimentally determined quantities. Ratio of Raman G-peak and D-peak intensities  $I_G/I_D$ , the number of graphene layers  $N$ , the extracted values of the optical phonon lifetime  $\tau_{ph}$ , and the average equilibrium carrier density per layer  $n_o$ .

terahertz-probe spectroscopy. Degenerate optical pump-probe studies of carrier dynamics in epitaxial graphene have been reported previously by the authors and others [31, 106]. In this letter, we use optical pump-probe spectroscopy to study optical phonon lifetimes in graphene, and we also present a theoretical framework for interpreting the results.

### 3.2 Sample preparation and experiment set-up

Graphene samples used in this work were grown on the silicon and carbon faces of semi-insulating silicon carbide 6H-SiC wafers by thermal decomposition epitaxial growth [5] and also by chemical vapor deposition(CVD) on nickel [67, 124]. Samples A and B were grown on the carbon face of SiC and Sample C was grown on the silicon face of SiC. Sample D was grown by CVD on nickel and then transferred onto a quartz substrate. Sample D was found to have patches in which the number of layers varied between 1 and 3. All samples were characterized via Raman spectroscopy(pump wavelength 488 nm) and optical/IR transmission spectroscopy. The characteristics are recorded in Table 4.1. For spectroscopy, the pump and the probe beams were obtained from a

Ti:Sapphire mode-locked laser with a 81 *MHz* pulse repetition rate and a 780 *nm* center wavelength. The pulse width [full width at half maximum (FWHM)] at the sample was measured to be  $\sim 100$  *fs*. The polarization of the probe was rotated 90° with respect to the pump such that scattered pump light could be filtered out of the probe beam before photodetection using a polarizer and a spatial filter. The differential transmission  $\Delta T$  of the probe due to the pump was obtained by chopping the pump and probe at different frequencies and recording the photodetector current at the sum frequency with a lock-in amplifier. The experiment set-up is illustrated in Figure 3.1.

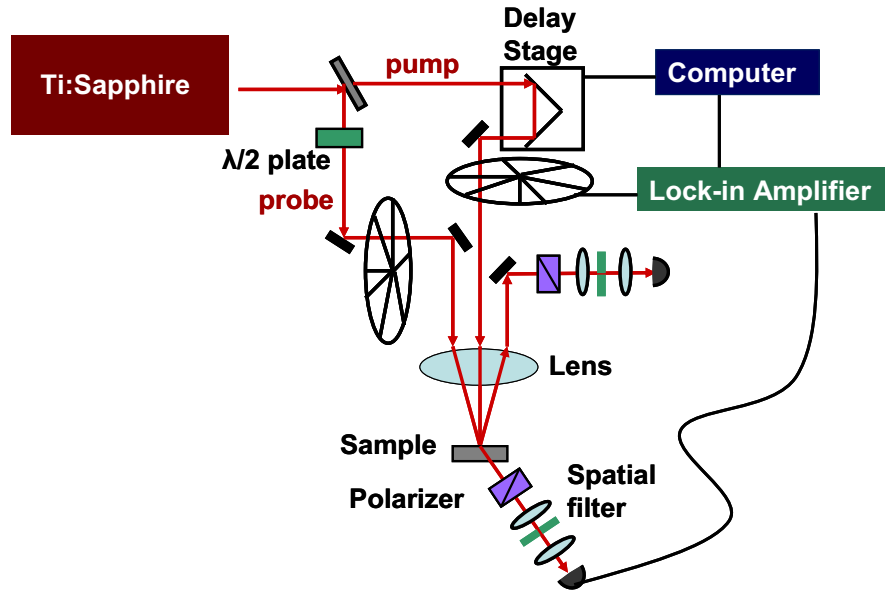


Figure 3.1: The ultrafast optical pump optical probe setup. Note that the double chopped configuration is actually done as in Figure 2.7.

The measured time-resolved  $\Delta T$  signals (normalized to their peak values) for all the four samples are shown in Figure 3.2 (solid circles). In each case, the pump energy was 14 *nJ* (fluence  $\sim 15$   $\mu\text{J}/\text{cm}^2$ ). The photoexcited carrier density was estimated to be  $5 \times 10^{11}/\text{cm}^2$  per layer for samples A through C (SiC substrate), and  $8 \times 10^{11}/\text{cm}^2$  per layer for sample D (quartz substrate). The measured

transients exhibit two distinct time scales. The  $\Delta T$  signal decreases rapidly to almost 10% of its peak value in the first 400~500 *fs*, and then it decreases much more slowly afterwards. These results can be qualitatively explained in the following way. We assume that the probe transmission is affected only by the change in the interband absorption caused by the pump pulse. Since the probe transmission is sensitive to the carrier occupation in the conduction and valence bands at energies  $\hbar\omega/2$  above the Dirac point (half of the pump photon energy) [32], it is also sensitive to the carrier temperature. Immediately after photoexcitation, the photogenerated electrons and holes thermalize with each other and the existing carriers, thereby acquiring FermiDirac distributions with high temperatures. Recent studies have shown that the thermalization times for the photoexcited carriers in graphite are extremely short and in the 20~40 *fs* range [15]. Due to the fast electron-hole scattering times, it is also reasonable to assume that the electron and hole temperatures are approximately the same. The thermalized electron and hole distributions then cool down via interaction with the optical phonons. The hot photoexcited carriers lose most of their energy to the optical phonons in the first ~500 *fs* after photoexcitation. This results in the generation of hot optical phonons, which then present a bottleneck to the subsequent cooling of the carriers. The relaxation dynamics of the carriers and the optical phonons are strongly coupled, and experimental data can be interpreted correctly only if this coupling is taken into account. The photoexcitation, relaxation and probe detection mechanisms are illustrated in Figure 3.3.

Below, we present a model that considers this coupling, and we use this model to extract the optical phonon lifetime from the data.

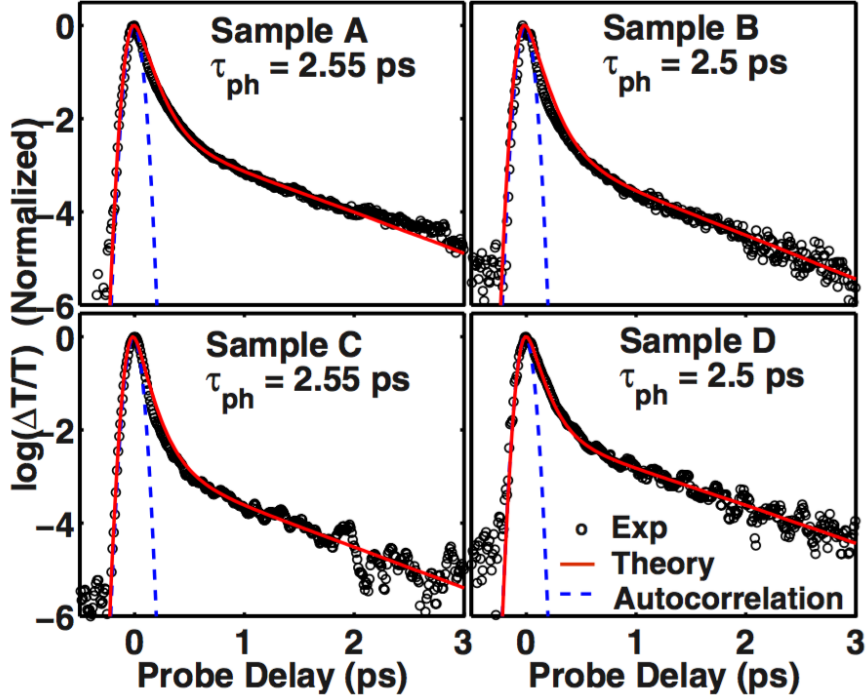


Figure 3.2: Graphene OPOP transients. Measured differential probe transmissions (normalized to peak value) (circles). The autocorrelation of the  $\sim 100fs$  pump and probe pulses(dashed lines), and the best-fit theoretical curves(solid lines) are plotted for different graphene samples. The extracted values of the average optical phonon lifetime  $\tau_{ph}$  are indicated for each graphene sample.

### 3.3 The electron-phonon scattering model

Intraband electron-phonon scattering can be intravalley (due to the  $\Gamma$ -point  $E_{2g}$  optical phonons or intervalley (due to the  $K(K')$ -point  $A'_1$  phonons). The intravalley and intervalley phonon scattering processes in graphene are illustrated in Figure 3.4. Using the matrix elements for electron-phonon scattering given by Rana et al. [122], the net optical phonon emission rates,  $R_{\Gamma_c}$  and  $R_{K_c}$  unit:  $cm^{-2}s^{-1}$ , due to intraband intravalley and intervalley electron-phonon scattering, respectively, can be expressed as:

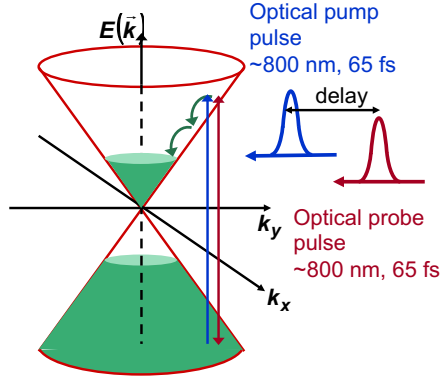


Figure 3.3: Cartoon illustration of an OPOP experiment on graphene. The curved green arrows represents the subsequent hot carrier thermalization and relaxation after the pump photoexcitation.

$$R_{\Gamma_e} \approx 9 \frac{(dt/db)^2}{\pi \rho \omega_{\Gamma} \hbar^4 v^4} \int_{\hbar\omega_{\Gamma}}^{\text{inf}} dE \times E(E - \hbar\omega_{\Gamma}) \times \{f_c(E)[1 - f_c(E - \hbar\omega_{\Gamma})](1 + n_{\Gamma}) - f_c(E - \hbar\omega_{\Gamma}) \times [1 - f_c(E)]n_{\Gamma}\} \quad (3.1)$$

The integrand in the above equation is the distribution in energy of the electron-phonon scattering events. The expression for  $R_{Ke}$  is the same as above except for the replacement  $\Gamma$  to  $K$ . Here,  $dt/db$  equals  $\sim 45 \text{ eV/nm}$  [122, 115] is the density of graphene and equals  $\sim 7.6 \times 10^{-7} \text{ kg/m}^2$ ,  $\omega_{\Gamma}(n_{\Gamma})$  and  $\omega_{\Gamma}(n_{\Gamma})$  are the frequencies (average occupation numbers) of the  $E_{2g}$  and  $A'_1$  phonons, respectively,  $v = 10^6 \text{ m/s}$ , and  $f_c(E)$  is the FermiDirac distribution function for conduction band electrons. Similar expressions as above can be written for the optical phonon emission rates,  $R_{\Gamma h}$  and  $R_{Kh}$ , due to hole phonon intraband scattering.

The carrier temperature  $Tc$  and the optical phonon occupation numbers,  $n_{\Gamma}$  and  $n_K$ , obey the coupled rate equations:

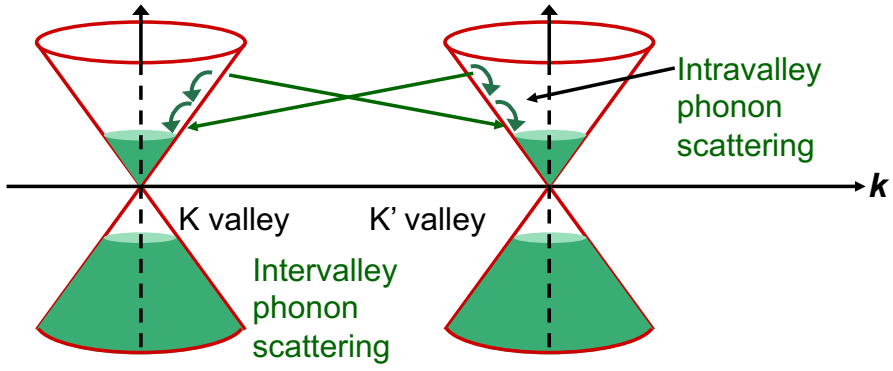


Figure 3.4: Intravalley and intervalley electron-phonon scattering in graphene.

$$\frac{dT_c}{dt} = -\frac{(R_{\Gamma e} + R_{\Gamma h})\hbar\omega_{\Gamma} + (R_{K e} + R_{K h})\hbar\omega_K}{C_e + C_h} \quad (3.2)$$

$$\frac{dn_{\Gamma}}{dt} = \frac{R_{\Gamma e} + R_{\Gamma h}}{M_{\Gamma}} - \frac{n_{\Gamma} - n_{\Gamma}^o}{\tau_{ph}} \quad (3.3)$$

$$\frac{dn_K}{dt} = \frac{R_{K e} + R_{K h}}{M_K} - \frac{n_K - n_K^o}{\tau_{ph}} \quad (3.4)$$

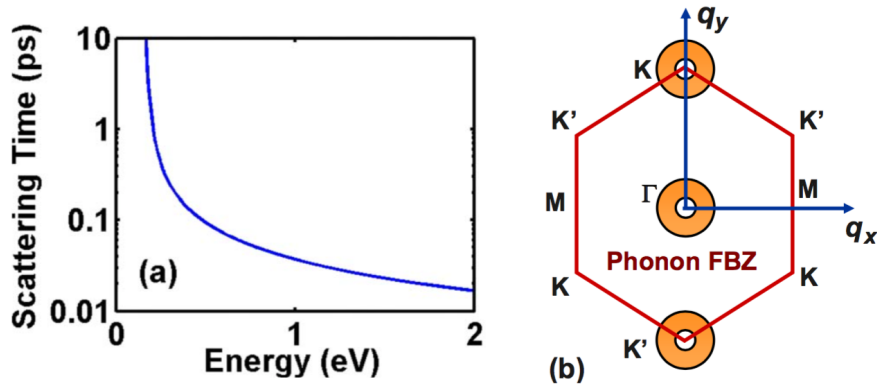


Figure 3.5: Scattering rates and phase space of carrier-phonon interactions. (a) The electron intraband scattering time due to optical phonon scattering is plotted as a function of the electron energy [122]. (b) The phonon Brillouin zone is shown together with the annular regions (not to scale) at the  $\Gamma$  and  $K(K')$  points, in which the optical phonons participate in electron-phonon scattering.

Here,  $C_e$  and  $C_h$  are the electron and hole heat capacities and  $\tau_{ph}$  is the average lifetime of the  $E_{2g}$  and  $A'_1$  optical phonons.  $n_\Gamma^o$  and  $n_K^o$  are the phonon numbers in equilibrium (at  $T = 300\text{ K}$ ).  $M_\Gamma$  and  $M_K$  are the number of phonon modes (per unit area) at the  $\Gamma$  and  $K(K')$  points, respectively, that participate in carrier-phonon interaction. At the  $\Gamma$  point, only phonons with wave vector magnitudes  $q$  in a certain range (dictated by momentum and energy conservation) participate in carrier-phonon interaction. If an electron with wave vector  $k$  emits an optical phonon, then the smallest value of  $q$  is  $\omega_\Gamma/v$  and most of the emitted phonons have wave vectors smaller than  $k$ . For carrier densities in the  $10^{11} \sim 10^{12}\text{ cm}^{-2}$  range, and carrier temperatures in the  $300 \sim 3000\text{ K}$  range, most of the electrons that emit optical phonons have energies less than  $E_{max} \approx 0.8\text{ eV}$  [see Figure 3.6 (a)]. Therefore, the largest value of  $q$  can be approximated by  $E_{max}/\hbar v$ . These estimates have been verified by detailed calculations using wave vector dependent distributions for the phonons [16]. The value of  $M_\Gamma$  then corresponds to the number of phonon modes that are in the annular region [see Figure 3.5(b)] defined by the minimum and maximum values of  $q$  and equals  $2 \times [(E_{max}/\hbar v)^2 - (\omega_\Gamma/v)^2]/4\pi$ . The factor of 2 in the front stands for the two degenerate LO and TO phonon bands at the  $\Gamma$  point. Similarly,  $M_K$  equals  $2 \times [(E_{max}/\hbar v)^2 - (\omega_K/v)^2]/4\pi$ . Here the factor of 2 in the front stands for the two degenerate phonon valleys at the  $K$  and  $K'$  points. Since the optical phonon emission time for an electron at an energy  $\hbar\omega/2\text{ eV}$  above the Dirac point is less than  $\sim 50\text{ fs}$  [see Figure 3.5(a)], the initial carrier temperature is computed by assuming that during the first  $100\text{ fs}$  after photoexcitation all the photogenerated carriers emit  $\sim 2$  optical phonons. The set of coupled rate equations (3.2, 3.3, 3.4) were solved to obtain the carrier temperature and the phonon numbers as a function of time. It is assumed that no significant carrier recombination oc-

curs in the first few picoseconds [50]. The carrier distributions were then used to compute the optical transmission using the expressions given by Dawlaty et al [31], and the results were convolved with a probe pulse assumed to be Gaussian with a FWHM of 100  $fs$  (see Figure 5.3, solid lines). The only two fitting parameters in the model are  $\tau_{ph}$ , and the equilibrium carrier density per layer,  $n_o$ . Their extracted values are given in Table 4.1. The extracted values of  $\tau_{ph}$  are not sensitive to the extracted values of  $n_o$  nor to the photoexcited electron-hole densities. Figure 3.6(b) shows the agreement between the theory and the data for different pump pulse energies. In each case, the average best fit value for  $\tau_{ph}$  was found to be 2.5  $ps$ .

Figure 3.6(c,d) show the calculated carrier and phonon temperatures and phonon occupation numbers plotted as a function of time after photoexcitation  $\tau_{ph}$  was assumed to be 2.5 ps. We assumed that the phonons were initially at room temperature (300 K) and the equilibrium electron density was  $10^{11} cm^{-2}$ . In the first 500  $fs$ , the electron temperature rapidly decreases and the phonon temperature rapidly increases. For photoexcited carrier densities in the  $10^{11} \sim 2 \times 10^{12}$  range, the maximum phonon temperatures were found to be in the 550~1550  $K$  range, in agreement with the earlier findings of Song et al. [139]. As the temperature of the carriers and the phonons approach each other, the net energy exchange between the electrons and the phonons also decreases. The hot optical phonons then become the main bottleneck for further carrier cooling. It should be noted that the subsequent cooling of the coupled carrier-phonon system is not determined by the phonon lifetime alone. The coupling of the hot carriers to the phonons retards the cooling of the phonons. Figure 3.6(d) shows that the phonon occupation numbers exhibit decay times that are slightly longer than the value of  $\tau_{ph}$  and in the 2.9~3.5  $ps$  range.

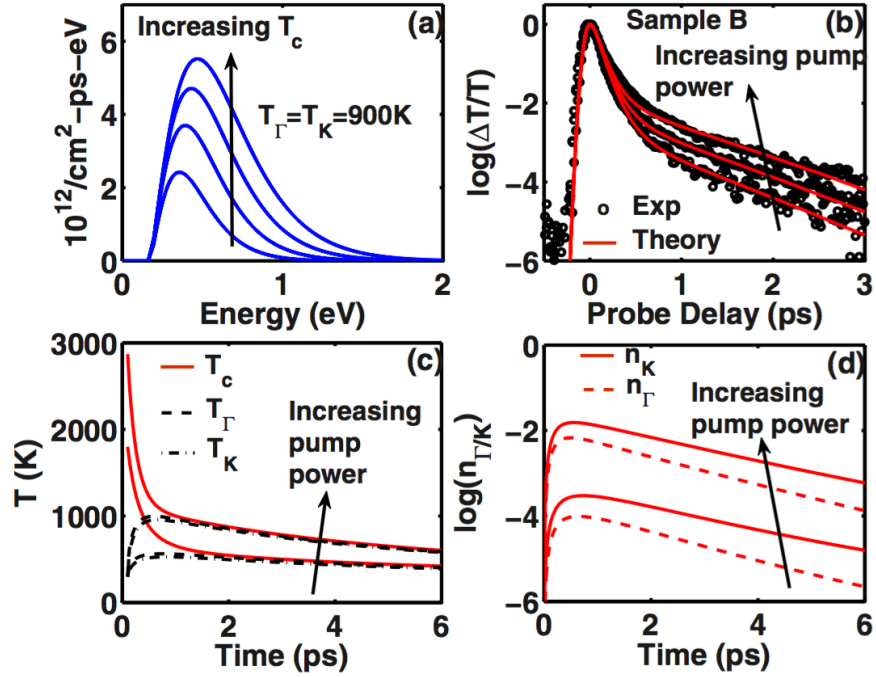


Figure 3.6: Hot carrier cooling simulation results. (a) Calculated electron-phonon scattering rate vs electron energy is plotted for values of  $T_c$  equal to 1250, 1500, 1750, and 2000 K: total electron density is assumed to be  $7 \times 10^{11} \text{cm}^{-2}$ . Phonon temperature is fixed at 900 K. (b) Measured differential probe transmissions (normalized to the peak value) (circles) and the best-fit theoretical curves (lines) are plotted for different pump pulse energies (2.5, 6, and 9.8 nJ). [(c) and (d)] The calculated electron and phonon temperatures and the phonon occupation numbers are plotted as a function of time after photoexcitation. The photoexcited electron-hole densities are assumed to be  $2 \times 10^{11}$  and  $7 \times 10^{11} \text{cm}^{-2}$ . The equilibrium electron density is assumed to be  $10^{11} \text{cm}^{-2}$ .

### 3.4 Conclusion

Experimental results show that the optical phonon cooling rates on short time scales are independent of the growth technique, the number of graphene layers, and the type of the substrate. On the fast time scales relevant to our experiments energy transport among the graphene layers, or between the graphene layers and the substrate, is not the bottleneck for hot optical phonon relaxation.

Measured optical phonon lifetimes agree very well with the theory based on anharmonic phonon interactions developed by Bonini et al [14]. Contrary to expectations [41], the substrate (SiC and quartz) optical phonons do not seem to play noticeable or distinctive role in hot carrier relaxation. This could be because the samples used in this study were not single-layer.

CHAPTER 4  
DEFECT ASSISTED CARRIER RECOMBINATION DYNAMICS IN  
MONOLAYER  $\text{MoS}_2$

## 4.1 Introduction

In this chapter, we present the non-degenerate ultrafast optical pump optical probe (OPOP) studies of the carrier recombination dynamics in monolayer  $\text{MoS}_2$ . The time-resolved ultrafast OPOP experiment was designed to study the recombination dynamics of the total excited electron and hole populations, including both the mobile charges and the quasi-particles, such as excitons and trions. A rendered image illustration of the OPOP experiment is given in Figure 4.1.

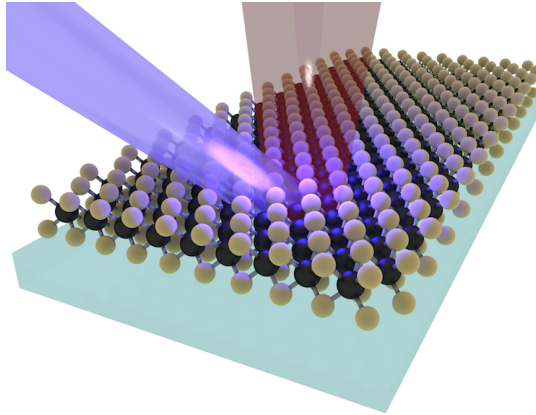


Figure 4.1: Rendered image illustration of the ultrafast OPOP experiment. Monolayer  $\text{MoS}_2$  samples were exfoliated onto quartz substrates. The strong blue pulses were used to excite electron-hole pairs, and the weak red pulses were designed to measure the carrier recombination dynamics after the pump excitation.

The goal of the project is to answer the following questions: what are the electron hole pair recombination time scales? what are the dominant recom-

bination mechanisms? Why quantum efficiency of the direct gap monolayer TMDs are generally very low (see Chapter 1)?

Last but not least, we will also compare our results to the published data based on different experimental technique. The proposed carrier recombination processes in this chapter not only explain our OPOP observations, but are consistent with the results obtained by other time-resolved techniques as well.

## 4.2 Sample preparation

Our monolayer samples were mechanically exfoliated from bulk MoS<sub>2</sub> (obtained from SPI Supplies and 2D Semiconductors) and transferred onto quartz substrates. Sample thickness was confirmed by both Raman and transmission/reflection spectroscopy and monolayers were identified [79]. The samples were found to be n-doped. The electron density was estimated from Raman measurements to be in the  $2\text{-}3\times 10^{12}\text{cm}^{-2}$  range [185, 21]. Electrical measurements on similar samples on oxide-coated doped silicon substrates (with electrostatic gating) yielded intrinsic electron densities in the same range [185]. The samples were placed in a helium-flow cryostat. In the optical pump-probe experiments,  $\sim 80$  fs pulses at 905 nm wavelength (1.37 eV photon energy) from a Ti-Sapphire laser were frequency doubled to 452 nm (2.74 eV) by a beta-BaB<sub>2</sub>O<sub>4</sub> crystal. The 2.74 eV pump pulses were used to excite electrons from the valence band into the conduction band in the sample, and the differential transmission ( $\Delta T/T$ ) of the time-delayed 1.37 eV pulses were used to probe the sample after photoexcitation. A 20X objective was used to focus the pump and the probe beams onto the sample. From direct pump absorption measurements, 1

$\mu J cm^{-2}$  pump fluence is estimated to generate an electron (and hole) density of  $\sim 2.5 \times 10^{11} cm^{-2}$ . The measurement time resolution was  $\sim 400 fs$ , and was limited by the dispersion of the optics in the setup.

### 4.3 Measuring photoexcited carrier recombination dynamics

Measuring photoexcited carrier recombination dynamics in semiconducting monolayer TMDs is not trivial. Differing from III-V semiconductors, which generally have exciton binding energies in the few  $meV$  to few tens of  $meV$  range due to the weak electron-hole interactions[100], semiconducting TMDs have extremely large exciton binding energies on the order of several hundreds of  $meV$ [94, 185, 155]. Such large exciton binding energies raise questions regarding the state of the photoexcited electron-hole pairs, and the validity of the experimental techniques in measuring the carrier recombination dynamics.

In time-resolved ultrafast experiments, electron-hole pairs are created by strong optical pulses with photon energies exceeding the bandgap of the material under study. For monolayer  $MoS_2$ , the direct gap energy is between  $2.0 \sim 2.3 eV$ [94, 185, 155], hence we chose to use  $450 nm$  blue pulses ( $2.74 eV$ ) to excite electrons from the valence band into the conduction band. The band structure, and the real/imaginary parts of the optical conductivity of monolayer  $MoS_2$  are shown in Figure 4.2. The optical conductivity was obtained as described in Chapter 2.

Ultrafast OPOP experiments should be designed such that the carrier recombination dynamics directly relate to the collected time-resolved data. In our case, the collected time-resolved data is the change in the probe transmittance

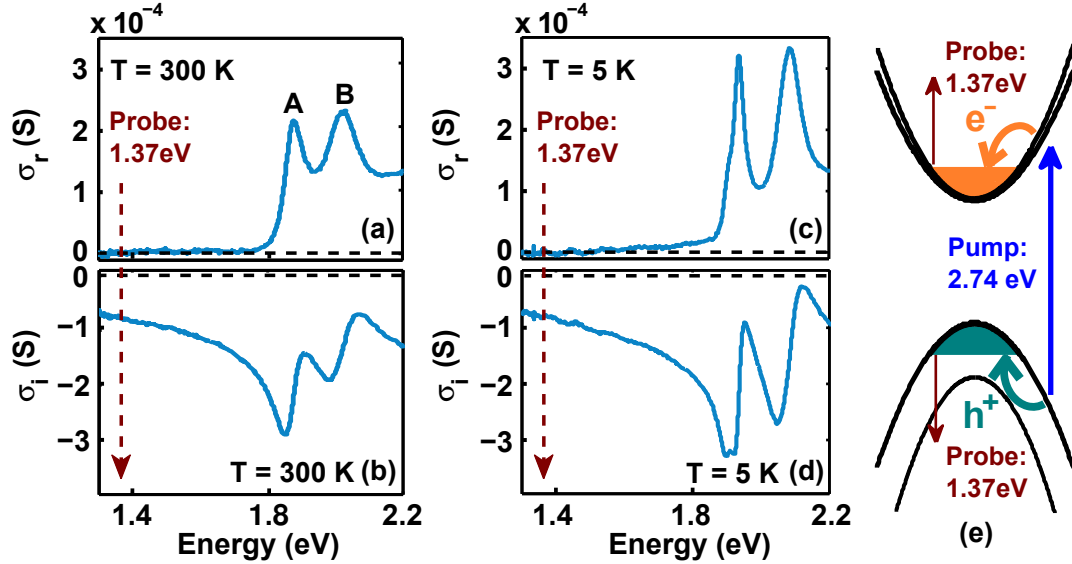


Figure 4.2: Optical conductivity of monolayer MoS<sub>2</sub>. (a,b,c,d) The measured real and imaginary parts of the optical conductivity of a monolayer MoS<sub>2</sub> sample are plotted for 5 K and 300 K. The A and B exciton resonances, as well as the probe photon energy are also indicated. (e) Schematic of the optical pump-probe scheme is shown. The probe differential transmission is affected predominantly by changes in the real part of the optical conductivity due to intraband absorption (intra-conduction band and intra-valence band absorption).

after the pump excitation. The challenge is to find the proper wavelength of the probe pulse to correctly measure the electron-hole recombination dynamics. Free carrier response is best measured by exploiting the intraband absorption of optical pulses consisting of low energy photons, and hence the optical-pump THz-probe (OPTP) technique is popular in measuring the recombination dynamics of mobile charges [50, 143]. However, for semiconducting TMDs, the electron-hole pairs are strongly correlated, and the exciton binding energy is so large ( $\sim 300$  meV) that THz photons ( $\sim 5$  meV) do not have enough energy to separate the excitons, making the excitons transparent to the THz photons. To correctly analyze OPTP data, researchers need information regarding the exci-

ton dynamics in addition to the mobile carrier dynamics. Next, we will discuss the reason why a 1.37 eV probe can detect carrier recombination dynamics in monolayer MoS<sub>2</sub>, including both mobile and immobile carriers.

By solving the electromagnetic boundary problem at the 2D-substrate interface[32, 50], the differential transmission of the probe relates to  $\sigma_r$  and  $\sigma_i$  as:

$$\frac{\Delta T}{T} \approx -2\eta_o \frac{\Delta\sigma_r}{1+n_s} - 2\eta_o^2 \frac{(\sigma_r\Delta\sigma_r + \sigma_i\Delta\sigma_i)}{(1+n_s)^2} \quad (4.1)$$

Where,  $\sigma_r$  ( $\sigma_i$ ) is the real (imaginary) part of the sample optical conductivity,  $n_s \approx 1.45$  is the refractive index of the substrate, and  $\eta_o$  is the free-space impedance. The optical conductivities were measured by broadband transmission and reflection spectroscopies, and are shown in Figure 4.2(a)-(d), at 5 and 300 K, respectively. When the probe energy is either near an exciton resonance or near a band-edge, the sign and magnitude of the changes in the optical conductivities following photoexcitation, due to excitonic optical nonlinearities and band-filling effects, can have a complicated dependence on the probe energy. This makes quantitative interpretation of pump-probe data a difficult task [23]. We therefore chose the probe energy to be much smaller than the exciton resonance. No detectable optical absorption or photoluminescence was observed in the samples at the probe energy (1.37 eV) indicating that the sample had no optically active midgap defect states at this energy. Changes in the imaginary part of the optical conductivity after photoexcitation due to excitonic optical non-linearities and band filling effects are expected to be positive at the probe energy [23], thereby making  $\Delta T/T$  positive, which is contrary to our experimental observations discussed below. In addition, since  $\eta_o\sigma_r$  and  $\eta_o\sigma_i$  are both  $\ll 1$  at

the probe energy (see Figure 4.2), the second term on the right hand side in Eq. 4.1 is expected to be much smaller than the first term. The differential transmission of the probe is expected to be affected predominantly by changes in the real part of the optical conductivity as given by the first term on the right hand side in Eq. 4.1 due to intra-conduction band and intra-valence band absorption [38]. Therefore,  $\Delta T/T$  is expected to be negative.

To measure the recombination dynamics of photoexcited electron-hole pairs, the photon energy of the optical probe must be much bigger than the exciton binding energy, while at the same time, much smaller than the exciton photoexcitation energy. For monolayer MoS<sub>2</sub>, we chose to use 905 nm probe pulses. Because the exciton binding energy is much smaller than the 1.37 eV probe, intraband probe pulse absorption of the correlated electrons and holes is similar to mobile charges, and the intraband optical conductivity at the probe wavelength is Drude like:

$$\Delta\sigma_r(\omega) \approx \left( \frac{\Delta n}{m_e} + \frac{\Delta p}{m_h} \right) \frac{e^2\tau}{1 + \omega^2\tau^2} \quad (4.2)$$

where  $\omega$  is the probe frequency,  $\tau$  is the damping rate,  $m_e$  and  $m_h$  are the electron and hole effective masses (assumed to be equal to  $0.5m_o$  [185]), and  $\Delta n$  and  $\Delta p$  are the photoinduced changes in the total electron and hole densities including both free and bound (excitons) carriers. Therefore, the probe transmission in our experiments is sensitive to the total carrier population, and enables studies of the carrier recombination dynamics and mechanisms, which is the focus of our work.

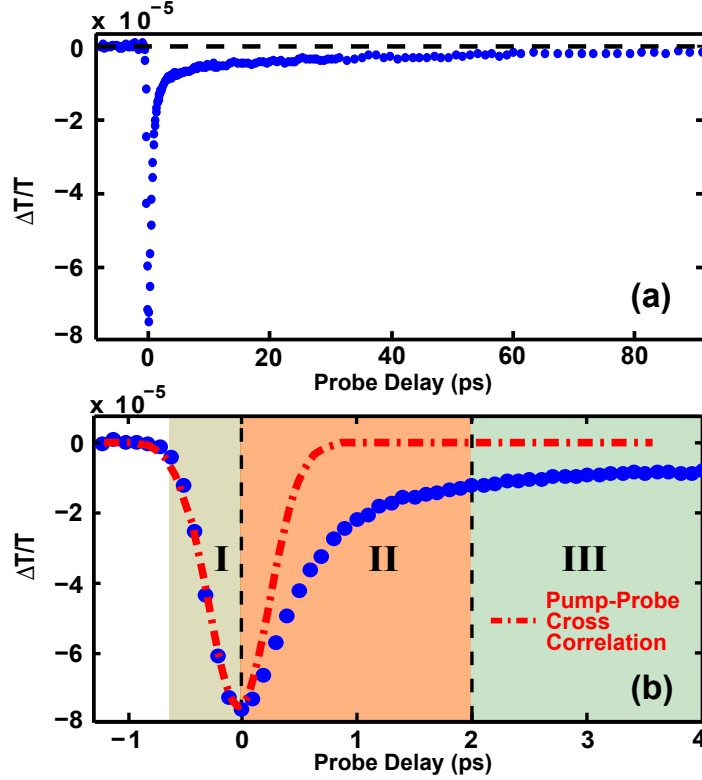


Figure 4.3: OPOP transient of monolayer  $\text{MoS}_2$ . (a) The measured differential transmission  $\Delta T/T$  of the probe pulse is plotted as a function of the probe delay with respect to the pump pulse. The pump fluence is  $\sim 16 \mu\text{Jcm}^{-2}$  and  $T=300 \text{ K}$ . (b) A zoomed-in plot of the data in (a) shows three different temporal regions: (I)  $\Delta T/T$  reaches its negative maximum within  $\sim 500 \text{ fs}$ . (II) A fast recovery of the negative  $\Delta T/T$  then occurs within  $\sim 2 \text{ ps}$ . (III) Finally, a slow recovery of the negative  $\Delta T/T$  lasts for more than a hundred picoseconds.

#### 4.4 Experimental results and discussion:

A differential transmission transient measured at room temperature is shown in Figure 4.3 for  $16 \mu\text{Jcm}^{-2}$  pump fluence ( $T = 300 \text{ K}$ ).  $\Delta T/T$  is observed to be negative, as expected from the intraband absorption of the probe photons by the photoexcited electron and hole populations. Three different time scales (or temporal regions) are observed and marked in Figure 4.3(b): (I) Upon photoexcitation by

the pump pulse,  $\Delta T/T$  reaches its maximum negative value within  $\sim 500$  fs. (II) A fast recovery of the negative  $\Delta T/T$  then occurs within  $\sim 2$  ps. (III) Finally, a slow recovery of the negative  $\Delta T/T$  lasts for more than hundred picoseconds. Figure 4.4 shows  $\Delta T/T$  for different pump fluences (1, 2, 4, 8, 16, and  $32 \mu J cm^{-2}$ ) at  $T=300$  K. The slow transient in region (III) appears to be nearly exponential with a time constant of 60-70 ps. The data presented here was reproducible in different samples exfoliated from both natural and synthetic bulk crystals obtained from different vendors (SPI Supplies and 2D Semiconductors) with less than 10% variation in the observed time scales across samples. The samples were found to be permanently damaged by pump fluence values exceeding  $\sim 50 \mu J cm^{-2}$ . Once damaged in this way, the measured transients changed dramatically, non-repeatably, and exhibited much longer time scales.

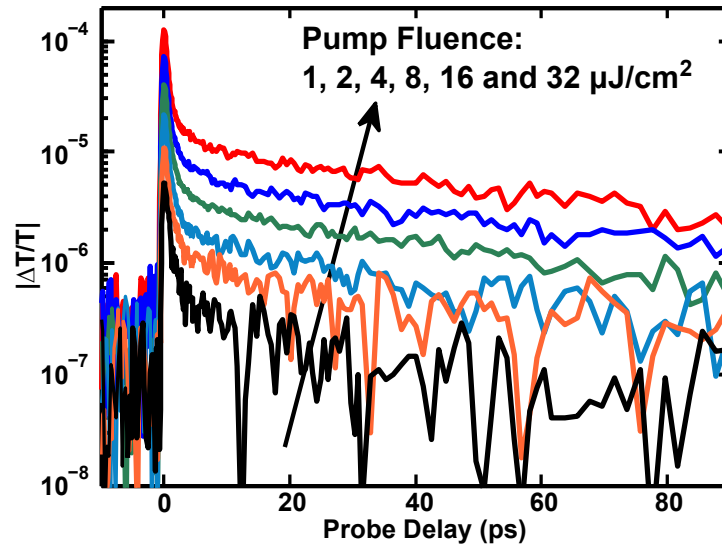


Figure 4.4: Pump fluence dependent OPOP transients. (a) The measured  $|\Delta T/T|$  of the probe pulse is plotted as a function of the probe delay for different pump fluences (1, 2, 4, 8, 16, and  $32 \mu J cm^{-2}$ ) at  $T=300$  K. The slow transient in region (III) appears to be nearly exponential with a time constant of 60-70 ps.

We now discuss the processes that contribute to the observed transients. Pos-

sible thermal diffusion of hot photoexcited carriers out of the pump or probe focus spots was ruled out as a contributing factor to the observed transients by changing the focus spot size in measurements [171]. Although carrier generation by the pump pulse and subsequent hot carrier intraband relaxation can contribute to the observed transient in region (I), our measurement is limited by the temporal resolution of the setup as indicated by the good fit of the transient in region (I) with the pump-probe cross-correlation curve. The asymmetry of the observed transient in (I) and (II) shows that two-photon absorption (TPA) between the pump and the probe pulses does not contribute in any significant way to the measured differential transmission of the probe pulse. The recovery of the negative  $\Delta T/T$  occurs over very different time scales in regions (II) and (III). These two different time scales have been observed in previous ultrafast studies [135, 73, 76]. The fast initial decay in region (II) cannot be attributed to intraband thermalization or hot carrier intraband relaxation since similar fast initial decay was also observed in ultrafast PL measurements by Lagarde et al. [76] (limited by the  $\sim 4$  ps time resolution in their experiments) and PL is likely to increase as the carriers thermalize and cool. Also, the intraband carrier relaxation times for electrons were measured by Tanaka et al. [151] in bulk MoS<sub>2</sub> using two-photon photoemission spectroscopy and times shorter than  $\sim 50$  fs were obtained for electrons with energies a few tenths of an eV from the conduction band edge [151]. It is therefore reasonable to assume that the photoexcited electrons and holes thermalize and lose most of their energy (via optical phonon emission) in the first few hundred femtoseconds after photoexcitation in a manner similar to what happens, for example, in graphene [163].

The small absolute values, as well as the pump intensity dependence, of

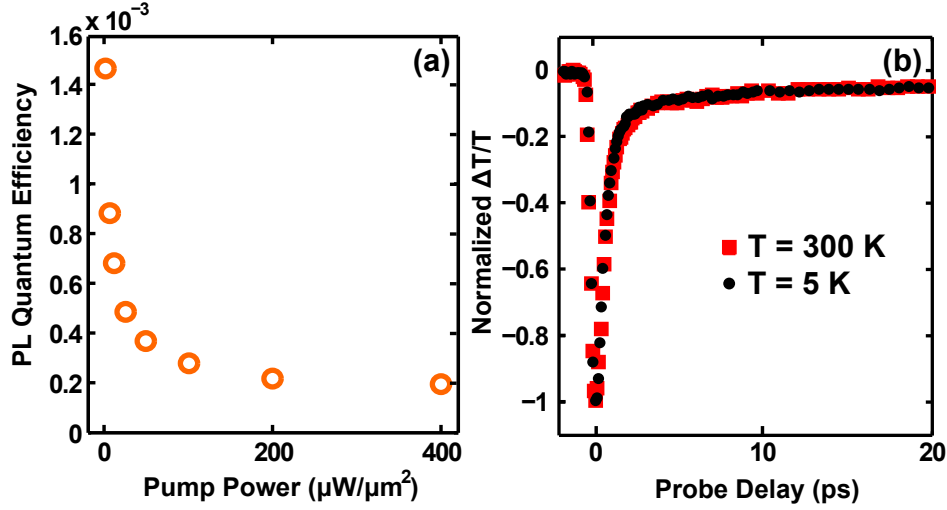


Figure 4.5: Quantum efficiency and temperature dependent OPOP transients. (a) Radiative quantum efficiency of a suspended monolayer  $\text{MoS}_2$  sample, obtained by integrating the photoluminescence (PL) spectra, is plotted as a function of the optical pump power (pump wavelength was  $532\text{ nm}$ ).  $T=300\text{ K}$ . (b) The measured  $\Delta T/T$  (normalized) of the probe pulse is plotted as a function of the probe delay for two different temperatures ( $5\text{ K}$  and  $300\text{ K}$ ). The data shows no significant temperature dependence of the time scales associated with the transient. The pump fluence was  $\sim 32\mu\text{Jcm}^{-2}$  in both cases.

the radiative quantum efficiencies in our samples provide a clue to interpret the transient in regions (II) and (III). Figure 4.5(a) shows the measured radiative quantum efficiency of a suspended monolayer  $\text{MoS}_2$  sample, obtained by integrating the PL spectra, plotted as a function of the optical pump intensity (pump in this case was a  $532\text{ nm}$  wavelength continuous-wave laser and  $T = 300\text{ K}$ ). The quantum efficiency was estimated based on the amount of actual light collected by a 100X objective [94]. The small values of the quantum efficiencies, in agreement with the previously reported values [94], show that most of the photoexcited carriers recombine non-radiatively. The decrease of the quantum efficiency with the pump intensity indicates that the steady state non-radiative recombination rates increase faster with the photoexcited electron

and hole densities compared to the radiative recombination rates. In addition, radiative lifetimes of excitons and trions were recently reported by us [165] and were found to be generally much longer compared to the picosecond scale dynamics observed in region (II). Based on these observations and considerations we attribute the measured transient in regions (II) and (III) to the non-radiative capture and recombination of photoexcited carriers.

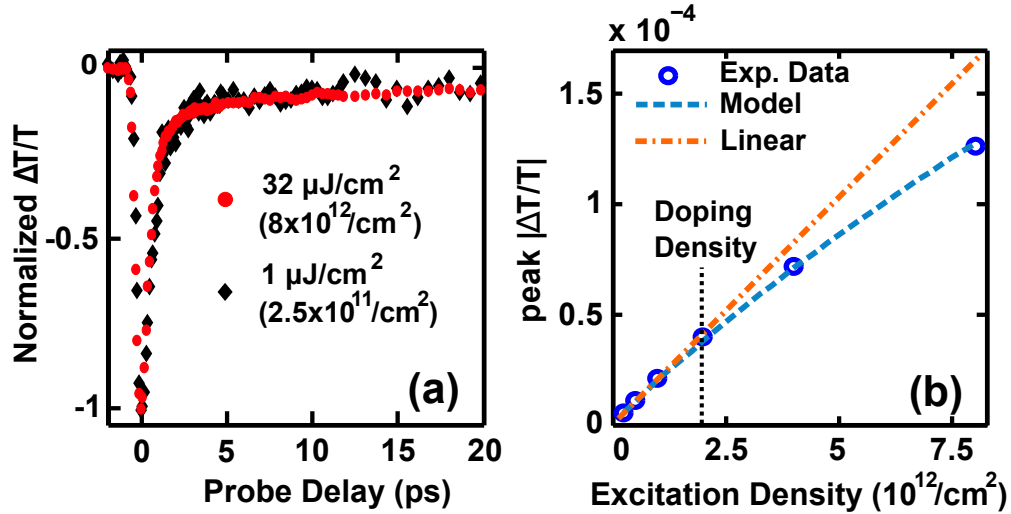


Figure 4.6: Normalized pump fluence transients. (a)  $\Delta T/T$  (normalized) is plotted for two different pump fluences, 1 and  $32 \mu\text{J}/\text{cm}^2$ , at  $T=300 \text{ K}$ . Whereas the slow time scale in region (III) is completely independent of the pump fluence, the fast time scale in region (II) becomes marginally faster (by 10-15%) at highest pump fluence compared to at the lowest pump fluence. (b) The peak value of  $|\Delta T/T|$  is plotted as a function of the photoexcited carrier density (estimated from the pump fluence) showing a mildly sub-linear dependence. The fit obtained from the Auger carrier capture model is also shown.  $T=300 \text{ K}$ .

In order to determine the non-radiative capture and recombination mechanisms we look at the temperature and pump fluence dependence of the time scales observed in the transients. Interestingly, the time scales in  $\Delta T/T$  exhibited no observable temperature dependence over the entire temperature range 5-300 K. In Figure 4.5(b), normalized  $\Delta T/T$  is plotted as a function of the probe delay

for two different temperatures (5 K and 300 K) and shows no significant temperature dependence in the time scales (the pump fluence was fixed at  $\sim 32 \mu J cm^{-2}$  in both cases). In Figure 4.6(a), the normalized transients for two extreme pump fluence values, 1 and  $32 \mu J cm^{-2}$ , are plotted (T=300 K). The data shows that the time scales in the transient are largely independent of the pump fluence in the entire range of the pump fluence values used in our experiments. A more careful examination reveals that while the time scale of the slow transient in region (III) is indeed independent of the pump fluence, the time scale of the fast transient in region (II) becomes marginally faster (by 10-15%) at highest pump fluence compared to at the lowest pump fluence. Figure 4.6(b) shows the peak value of  $|\Delta T/T|$  plotted as a function of the photoexcited carrier density (estimated from the pump fluence).  $|\Delta T/T|$  shows a mildly sub-linear behavior with the pump fluence. Below we show that defect-assisted recombination via Auger carrier capture explains all features of our data.

## 4.5 Auger carrier capture model

Recombination via direct band-to-band Auger scattering is generally slow for large bandgap materials [126] and it also cannot explain the sharp transition in the time scales observed in the transient between regions (II) and (III). Electron and hole capture by defects in defect-assisted non-radiative recombination occurs mainly by two mechanisms: (a) phonon-assisted processes, and (b) Auger processes. Phonon-assisted processes can be single-phonon processes or multi-phonon processes, including phonon-cascade processes [55, 78, 126]. The carrier capture rates in all phonon-assisted processes depend strongly on the lattice temperature [55, 78, 126]. For example, the rates of activated multi-phonon

capture processes depend exponentially on the lattice temperature [55, 126]. In contrast, the rate of carrier capture by defects via Auger processes is largely temperature independent and consistent with our observations [125, 77, 127, 52]. Figure 4.7 shows the four basic Auger processes for the capture of electrons ((a) and (b)) and holes ((c) and (d)) at defects and the approximate dependence of the capture rates on the electron and hole densities [125, 77, 127]. The corresponding emission processes are the just the inverse of the capture processes shown. The carrier density dependence of the capture rates shown in Figure 4.7 holds approximately for both bound (excitons) and free carriers. In our n-doped samples, process (a) and (c) are expected to dominate for electron and hole capture, respectively, at low to moderate pump fluence values.

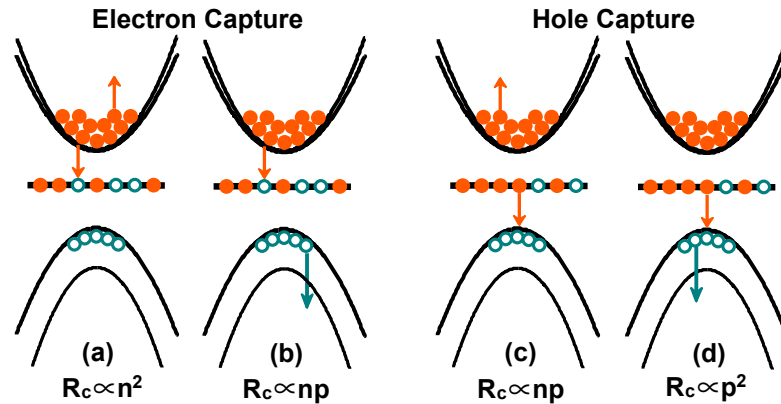


Figure 4.7: Four basic Auger Processes. Four basic Auger processes for the capture of electrons ((a) and (b)) and holes ((c) and (d)) at defects are depicted. The approximate dependence of the capture rates on the electron and hole densities is also indicated for each process [125, 77, 127]. In n-doped samples, processes (a) and (c) are expected to dominate for electron and hole capture, respectively, for low to moderate photoexcited carrier densities.

A simple rate equation model based on Auger carrier capture by defects can be developed that explains all features of our data. We note that the sudden transition from the fast time scale in region (II) to the slow time scale in region

(III) in the measured transients cannot be explained by saturation of the defects states alone since, as already discussed, the measured time scales in Figure 4.6 do not exhibit strong pump fluence dependence. Most semiconductors contain defect levels with very different carrier capture rates [56, 53, 11, 27, 173]. Monolayer MoS<sub>2</sub> is known to have several different kinds of point defects, such as sulfur and molybdenum vacancies and interstitials, in addition to grain boundaries and dislocations [42, 71, 37, 190, 107, 181, 85, 159]. We assume two different deep midgap defect levels in our samples; a fast defect level and a slow defect level, labeled by subscripts  $f$  and  $s$ , respectively. In our n-doped samples, the defect levels are assumed to be fully occupied in thermal equilibrium. Keeping only the most important Auger capture processes in n-doped materials ((a) and (c) in Figure 4.7), and ignoring electron and hole emission from the deep defects, we obtain the following rate equations for the electron and hole densities,

$$\frac{dn}{dt} = -A_f n_f n^2 (1 - F_f) - A_s n_s n^2 (1 - F_s) + gI(t) \quad (4.3)$$

$$\frac{dp}{dt} = -B_f n_f n p F_f - B_s n_s n p F_s + gI(t) \quad (4.4)$$

$$n_{f/s} \frac{dF_{f/s}}{dt} = A_{f/s} n_{f/s} n^2 (1 - F_{f/s}) - B_{f/s} n_{f/s} n p F_{f/s} \quad (4.5)$$

Here,  $n$  and  $p$  are the electron and hole densities and include both free electrons and holes as well as bound electrons and holes (excitons),  $n_f$  ( $n_s$ ) is the density of fast (slow) defect levels, and  $F_f$  ( $F_s$ ) is the electron occupation of the fast (slow) defect level.  $A_{f/s}$  ( $B_{f/s}$ ) is the rate constant for the Auger capture of electrons (holes) by the defects.  $I(t)$  is the pump pulse intensity (units:  $\mu J cm^{-2}$ -s) and  $g$  equals  $\sim 2.5 \times 10^{11} \text{ 1}/\mu J$  (from measurements). Change in the probe pulse transmission through the photoexcited sample is assumed to be given by Eq. 4.1 and Eq. 4.2. The essential dynamics captured by the above Equations are presented in Figure 4.8 and consist of three main steps corresponding to the three temporal regions in Figure 4.3: (I) After photoexcitation, the carriers thermalize and

cool. This is assumed to happen instantly in our model. (II) Most of the holes, followed by the electrons, are captured by the fast defects within a few picoseconds. This fast capture process is responsible for the fast time scale observed in region (II) in Figure 4.3. A small fraction of the photoexcited holes is also captured by the slow defects. (III) After all the photoexcited holes have been captured and the electrons have filled the fast traps completely, the remaining photoexcited electrons are captured by the slow defects. This last step is slow and is responsible for the slow time scale observed in region (III) in Figure 4.3.

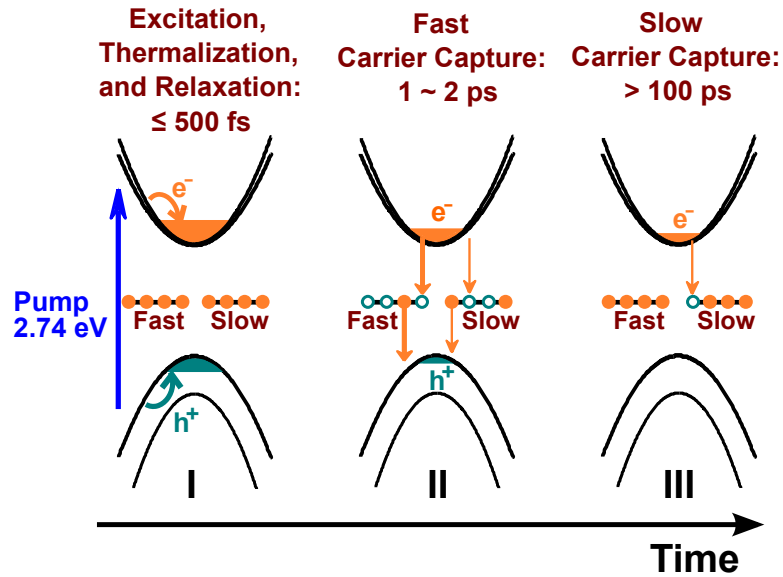


Figure 4.8: Cartoon illustration of the ultrafast carrier dynamics in monolayer MoS<sub>2</sub>. (I) After photoexcitation, the carriers thermalize and cool and form a correlated electron-hole plasma. (II) Most of the holes, followed by the electrons, are captured by the fast defects within 1-2 ps. A small fraction of the photo-generated holes is also captured by the slow defects. (III) After all the photoexcited holes have been captured and the electrons have filled the fast traps completely, the remaining photoexcited electrons are captured by the slow defects on a 60-70 ps time scale and the slow transient lasts for more than 100 ps.

The choice of the values of the parameters in Eq. 4.3-4.5 can be aided by the data. Assuming small pump fluence and knowing the equilibrium electron

$B_f n_f$	$0.73 \pm 0.05 \text{ cm}^2/s$
$B_s n_s$	$9.3 \pm 1 \times 10^{-2} \text{ cm}^2/s$
$A_s$	$9.5 \pm 1 \times 10^{-15} \text{ cm}^4/s$
$A_f$	$(1.0 \pm 0.2)B_f$
$n_f$	$0.3 \times 10^{12} \text{ to } 10^{12} \text{ cm}^{-2}$
$n_s$	$10^{12} \text{ to } 2.0 \times 10^{13} \text{ cm}^{-2}$
$n_o$	$2.0 \times 10^{12} \text{ cm}^{-2}$

Table 4.1: Parameter values used in the simulations to fit the transient data.

density  $n_o$  and the fact that immediately after photoexcitation  $F_f \approx F_s \approx 1$ , the value of the product  $B_f n_f$  in Eq. 4.4 is chosen to match the time scale of the fast transient in region (II) in Figure 4.3. The value of the product  $B_s n_s$  is chosen to adjust the fraction of the holes that is captured by the slow defects in region (II) in order to fit the relative value of  $|\Delta T/T|$  in the beginning of region (III) compared to the peak value. From our data,  $B_s n_s$  should be 7.5-8 times smaller than  $B_f n_f$ . Knowing the hole density captured by the slow defects in region (II) (which equals  $n_s(1 - F_s)$  at the end of region (II)), the value of  $A_s$  is chosen to match the time scale of the slow transient in region (III) in Figure 4.3. Finally, the value of  $A_f$  is chosen to match the dependence of the peak value of  $|\Delta T/T|$  on the pump fluence, as show in Figure 4.6(b). Parameter values obtained this way are shown in Table 1. Once the parameter values have been chosen in this way, we find that the simulations fit the data very well for a small range of values of the defect densities,  $n_f$  and  $n_s$ , as indicated in Table 1. These defect density values compare well with the theoretically predicted and observed point defect densities in MoS<sub>2</sub> [42, 71, 190, 107, 181, 85, 159].

The agreement between the simulation results for  $\Delta T/T$  and the measurements are presented in Figure 4.9 and Figure 4.6(b). In Figure 4.9(a,b), the mea-

sured and calculated  $\Delta T/T$  (pump fluence normalized) are plotted as a function of the probe delay. The calculations are done for two different and extreme values of the pump fluence, 1 and  $32 \mu Jcm^{-2}$ , used in our experiments. The model not only reproduces the very different time scales observed in  $\Delta T/T$  measurements in regions (II) and (III), it achieves a very good agreement with the data over the entire range of the pump fluence values, 1 to  $32 \mu Jcm^{-2}$ , used in our experiments. The near exponential appearance of the measured transient in region (III) (see Figure 4.4) is also reproduced by our model despite the fact that the Auger capture rates are not linear functions of the carrier density. This can be understood as follows. In region (III), if at any time the hole density in the slow traps equals  $n_s(1 - F_s)$  then this is also equal to the photoexcited electron density  $n - n_o$  left in the conduction band. Therefore, in region (III) the rate equation for the electron density becomes,

$$\frac{dn}{dt} \approx -A_s n_s n^2 (1 - F_s) = -A_s n^2 (n - n_o) \approx -A_s n_o^2 (n - n_o) \quad (4.6)$$

The last approximate equality above follows from the fact that in region (III) the remaining photoexcited electron density  $n - n_o$  is much smaller than the doping density  $n_o$  for all pump fluence values used in our experiments. The above Equation shows that in region (III) the transient will behave almost like a decaying exponential with an inverse time constant given by  $A_s n_o^2$ . Figure 4.9(b) and (c) show the calculated carrier densities and the defect occupations for the maximum pump fluence of  $32 \mu Jcm^{-2}$  used in our experiments. The carrier and the defect state dynamics depicted in Figure 4.8 are reproduced by the model using the parameter values given in Table 1. From the computed carrier densities, one can obtain the scaling of the peak value of  $|\Delta T/T|$  with the pump fluence. Figure 4.6(b) shows the measured and the calculated dependence of the peak value of  $|\Delta T/T|$  on the pump fluence, and the model is again seen to agree well with

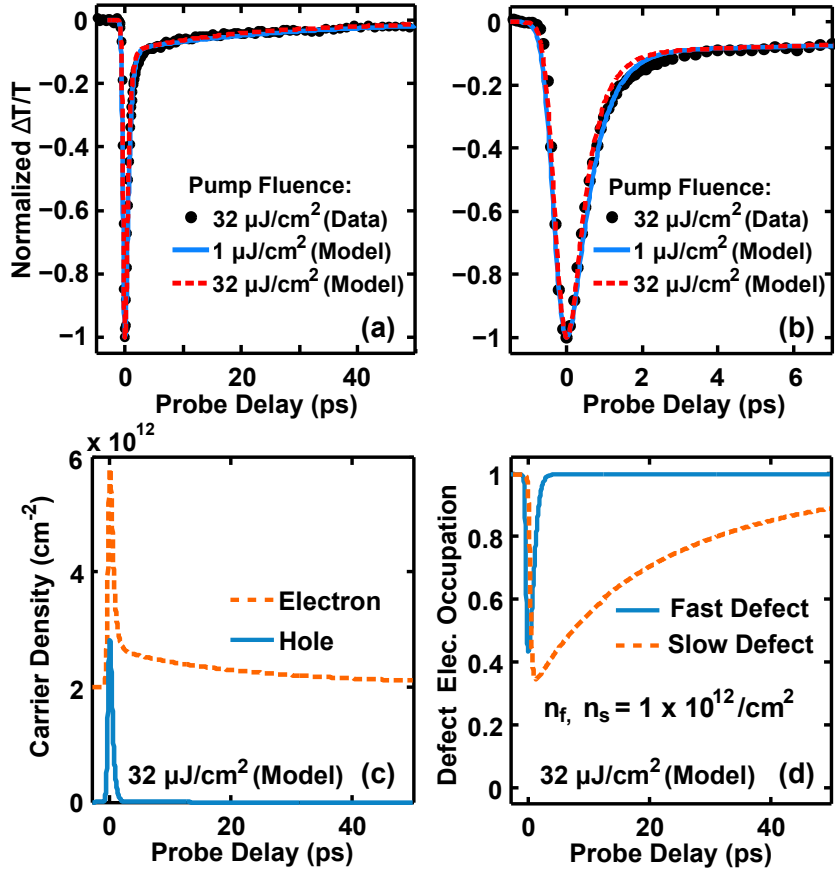


Figure 4.9:  $\Delta T/T$  transient simulations. (a, b) The measured and calculated  $\Delta T/T$  (pump fluence normalized) are plotted as a function of the probe delay. The calculations are done for two different and extreme values of the pump fluence, 1 and  $32 \mu\text{J}/\text{cm}^2$ , used in our experiments. The Auger carrier capture model reproduces all the time scales observed in the measurements over the entire range of the pump fluence values used. (c) The simulated electron and hole densities are plotted as a function of time after photoexcitation for  $32 \mu\text{J}/\text{cm}^2$  pump fluence. (d) The simulated electron occupations,  $F_f$  and  $F_s$ , of the fast and slow traps are plotted as a function of time after photoexcitation for  $32 \mu\text{J}/\text{cm}^2$  pump fluence.

the measurements. Finally, the calculated values of  $\Delta T/T$ , using Eq. 4.2, agree very well with the measurements if one assumes a carrier mobility,  $e\tau/(0.5m_0)$ , of  $\sim 35 \text{ cm}^2/\text{V}\cdot\text{s}$ , which is in the range of the values reported for exfoliated  $\text{MoS}_2$

monolayers [61].

## 4.6 Optically induced sample damage

In our experiments we found that exfoliated MoS<sub>2</sub> monolayers (SPI Supplies and 2D Semiconductors) could easily get damaged permanently when pump fluences in excess of  $\sim 50 \mu J cm^{-2}$  were used (452 nm wavelength). Once damaged in this way, the optical characteristics of the sample would change completely. So care needed to be exercised in ensuring that samples were not damaged during pump-probe, photoluminescence, or absorption measurements. An optical microscope image and a Raman spectroscopy image of a sample damaged by pump pulses is shown in Figure 4.10(a) and (b). The energy splitting between  $A_{1g}$  and  $E_{2g}$  mode is much larger at the damaged spots compared to the surrounding intact areas. Similar enhancement of the mode splitting in optically damaged samples has been reported previously [18].

In addition, damaged samples exhibited large optical absorption throughout the bandgap, as shown in Figure 4.10(c), indicating creating of midgap states. Finally, the transmission of the probe pulse at 905 nm wavelength in a damaged sample gets overwhelmed by the increased absorption inside the bandgap and, consequently, the dynamics observed by the probe pulse become completely different compared to the dynamics observed in an undamaged sample. A damaged sample shows a large slow component in the transient that has a time scale much longer than any of the time scales observed in an undamaged sample, as shown in Figure 4.10(d). The magnitude of the slow component in the measured transient is larger in samples damaged with a higher pump fluence. We

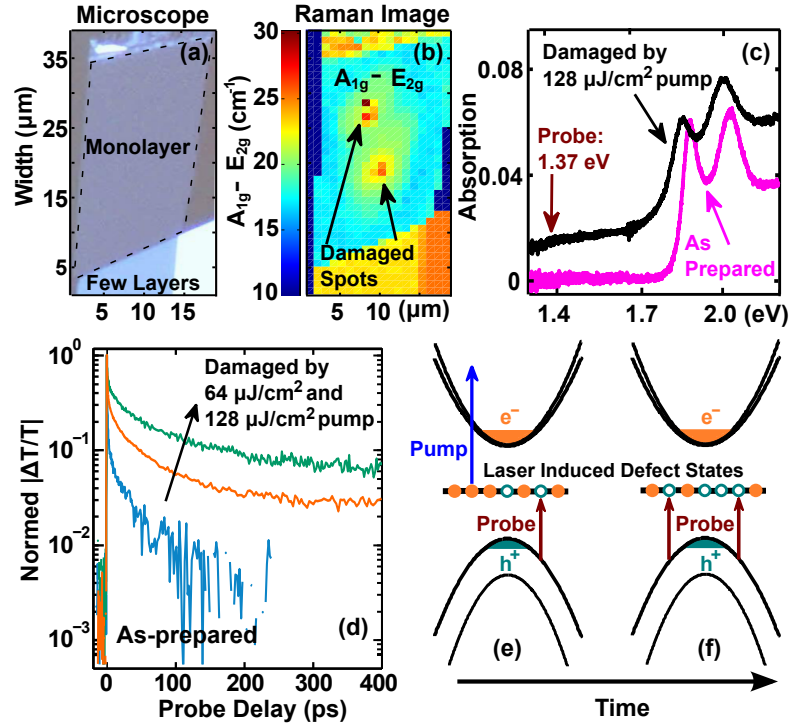


Figure 4.10: Optically induced damage in monolayer MoS<sub>2</sub>. (a) Optical microscope image of a sample damaged by a  $\sim 128 \mu\text{Jcm}^{-2}$  pump pulse is shown. No sign of damage is visible. (b) A scanned Raman image corresponding to the energy splitting between the  $A_{1g}$  and  $E_{2g}$  modes is shown for a sample damaged by a  $\sim 128 \mu\text{Jcm}^{-2}$  pump pulse. (c) A sample damaged by a  $\sim 128 \mu\text{Jcm}^{-2}$  pump pulse shows large absorption throughout the bandgap. (d) The transmission of the probe pulse at  $905 \text{ nm}$  wavelength in a damaged sample gets overwhelmed by the increased absorption inside the bandgap and, consequently, the dynamics observed by the probe pulse become completely different compared to the dynamics observed in an undamaged sample. A damaged sample shows a large slow component in the transient that has a time scale much longer than any of the time scales observed in an undamaged sample. (e,f) Possible probe absorption through optically induced defect states.

strongly feel that it is very important that the absence or presence of optically induced sample damage is checked before/after optical measurements in order to ensure that reliable data has been obtained.

## 4.7 Parameter space of Auger capture coefficients

The parameter fitting analysis given in the previous sections provides an intuitive understanding of the parameter fitting process of the Auger capture coefficients. Here, we provide a brute force approach to demonstrate that the parameters given in Table 4.1 cover the entire parameter fitting space.

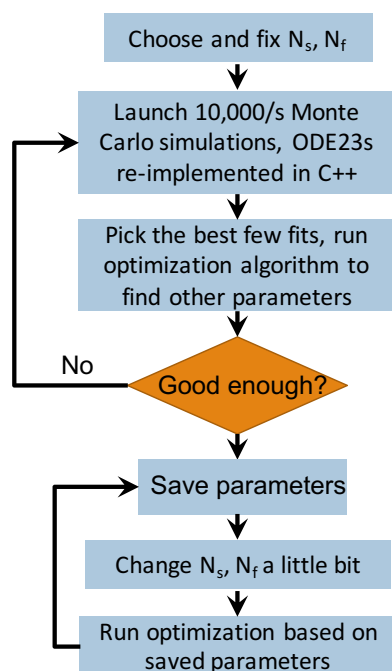


Figure 4.11: A C++ parameter solver. The flow diagram demonstrates how the fitting parameters were found by a C++ ODE parameter solver.

The basic algorithm is explained in Figure 4.11. For a given set of slow and fast trap densities, the algorithm finds the Auger parameters automatically through a multi-variable optimization method based on the best solutions found by Monte-Carlo simulations. Figure 4.12 illustrates the parameter space of the slow and fast trap density found by the C++ ODE parameter solver. To compare the Auger capture coefficients in Table 4.1 with the computer gener-

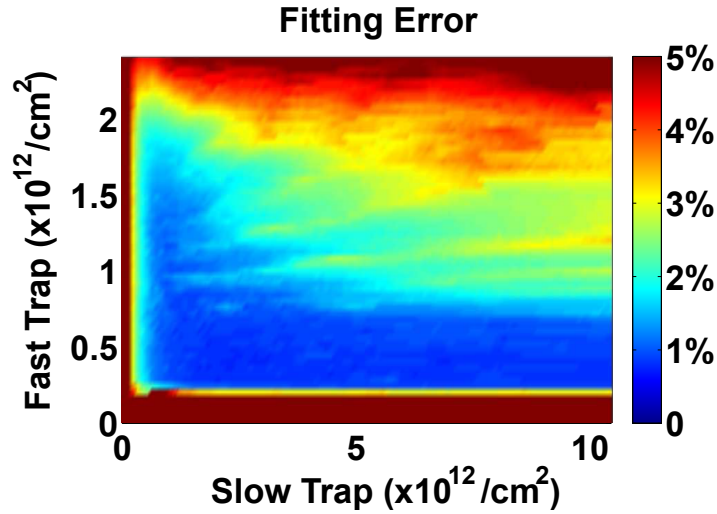


Figure 4.12: Fitting error given by the C++ parameter solver. This plot shows the Least Mean Square error given by the automatic ODE parameter solver in Figure 4.11 as a function of the slow and fast trap density. Good fitting exists for a wide range of slow and fast trap densities.

ated parameters, we plot the values in Table 4.1 against the optimization results in Figure 4.13. The computer generated Auger capture coefficients match the values in Table 4.1 very well.

## 4.8 Two Photon Absorption OPOP measurements

It would be interesting to confirm the photoexcited carrier recombination dynamics in monolayer MoS<sub>2</sub> using a different ultrafast technique. Instead of using the frequency doubled blue pulses as the pump, we used strong 905 nm near-IR pulses to serve as the pump. Although the 905 nm pulses cannot directly excite electrons from the valence band into the conduction band in monolayer MoS<sub>2</sub>, the photoexcitation is still possible through the Two Photon Absorption (TPA) process. TPA is a third-order process but has a quadratic dependence on

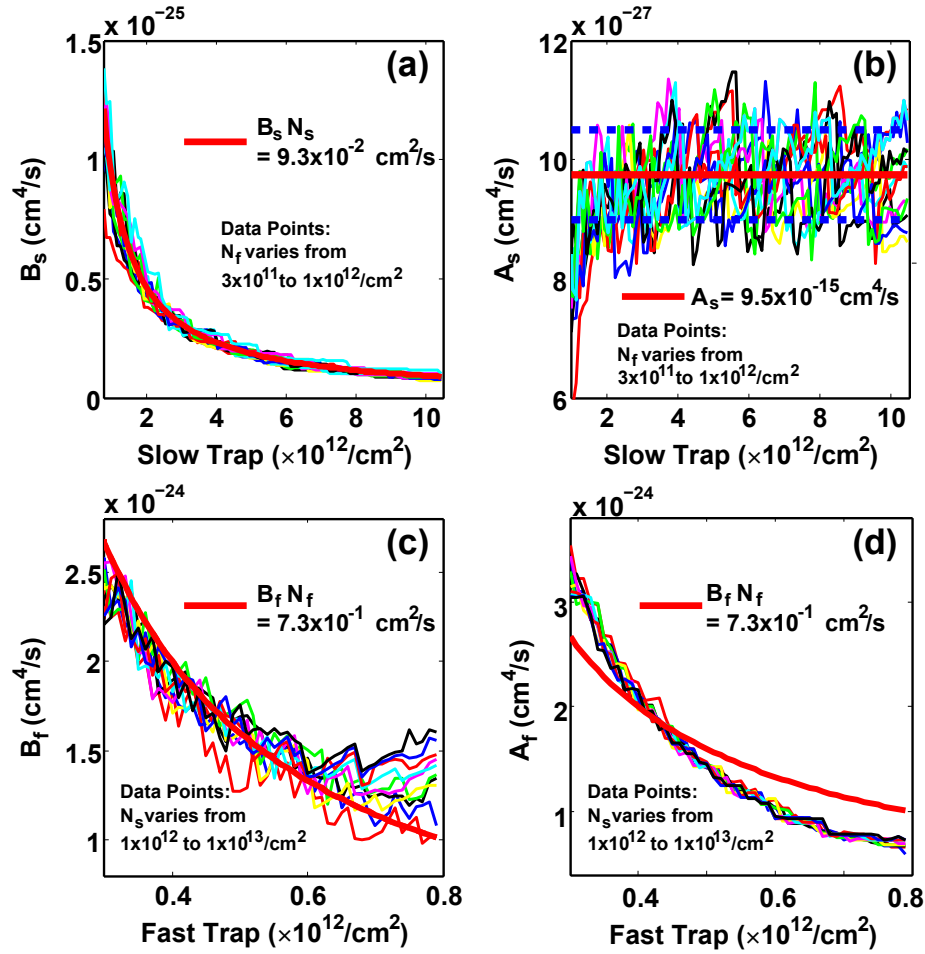


Figure 4.13: Optimized fitting parameters given by the C++ parameter solver. The fitting values given in Table 4.1 are plotted against the automatically generated parameter values given by the C++ ODE parameter solver.

the pump fluence (the absorption coefficient of the 3rd electric field scales as the product of the other two electric fields, details can be found in Boyds *et al.* [96]).

On the other hand, if the strong 905 *nm* pulses can directly excite the electrons trapped in the mid-gap states into the conduction band, and the measured transients in previous sections contain the defect dynamics, the amplitude of the OPOP defect transients should scale linearly as a function of pump fluence.

Therefore, by studying the pump fluence dependence in 905 nm degenerate OPOP measurements, we can figure out the contribution of the defect dynamics to the measured transients. In Figure 4.14(a), OPOP transients of three different pump fluences are plotted. It is very interesting to observe that, the  $3 \text{ mJ cm}^{-2}$  transient has a much larger carrier absorption signal compared to the  $0.6 \text{ mJ cm}^{-2}$  transient, implying that the photoexcited carrier density has a highly nonlinear pump fluence dependence. In Figure 4.14(b), we decompose the measured  $1.8 \text{ mJ cm}^{-2}$  transient into 2 parts: a TPA component and a carrier absorption (CA) component. By using the CA data in Figure 4.14(b), we are able to reconstruct the  $0.6$  and  $3 \text{ mJ cm}^{-2}$  transients as shown in Figure 4.14(c) by assuming that the photoexcited carrier density has a quadratic dependence on the pump fluence.

Because the defect TPA  $\chi^{(3)}$  is likely to be smaller than the band-to-band TPA  $\chi^{(3)}$  [186], the TPA OPOP transients confirm our non-degenerate OPOP experiments. The non-degenerate OPOP transients are indeed due to the intraband absorption of photoexcited electron-hole pairs, and the defect dynamics do not have a significant contribution to the measured transients. By using the same reconstruction method as in Figure 4.14(c), we can extract the CA component of the TPA OPOP transient, and plot it against the measured non-degenerate transient as shown in Figure 4.14(d). Other than a slight difference in time resolution, the non-degenerate and degenerate techniques are consistent with each other.

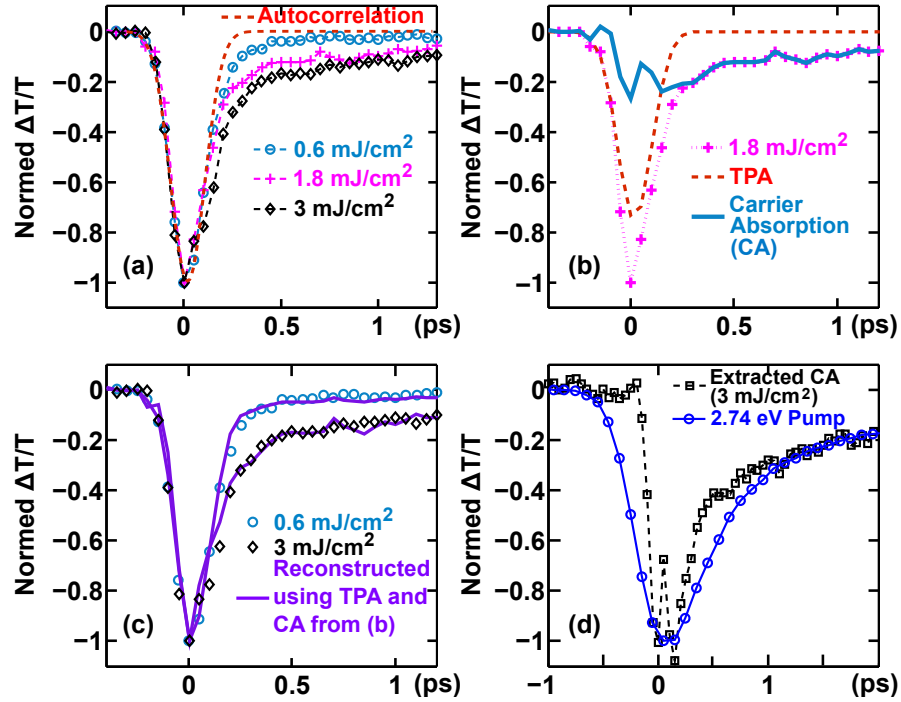


Figure 4.14: TPA OPOP transients. (a) OPOP transients of three different pump fluences are plotted. (b) we decompose the measured  $1.8 mJ/cm^2$  transient into 2 parts: a TPA component and a carrier absorption component (CA). (c) By using the CA data in (b), we are able to reconstruct the  $0.6$  and  $3 mJ/cm^2$  transients by assuming that the photoexcited carrier density has a quadratic dependence on the pump fluence. (d) Other than a slight difference in time resolution, the non-degenerate and degenerate techniques are consistent with each other.

## 4.9 Comparison with other ultrafast techniques

The experimental work published by Docherty et al. [34] on ultrafast PL and optical-pump THz-probe measurements of monolayer  $MoS_2$  are shown in Figure 4.15. Their general observations are in very good agreement with our experimental and theoretical results, and show that both electron and hole populations decay in the first 1-2  $ps$  after photoexcitation and that one carrier type (holes in our case) is almost entirely captured by defects in the first 1-2  $ps$

with only a small fraction of the other carrier type (electrons in our case) being captured over much longer time scales. Finally, we note here that our measurements might not have detected the charge trapping dynamics occurring on much longer time scales ( $\gg 10$  ns) as recently observed in MoS<sub>2</sub> photoconductive devices[26].

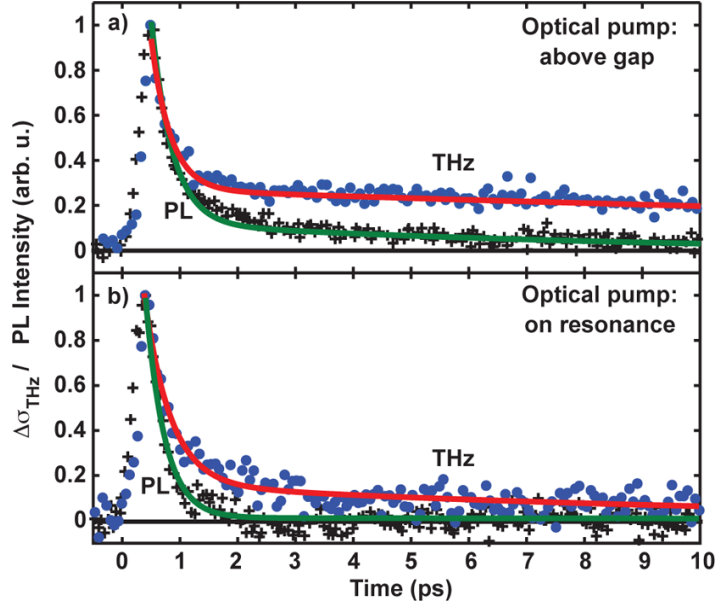


Figure 4.15: OPTP and PL transients of monolayer MoS<sub>2</sub> by Docherty **et al.** [34]. Results reported by Callum [34] are in very good agreement with our experimental and theoretical results, and show that both electron and hole populations decay in the first 1-2 ps after photoexcitation, and that one carrier type (holes in our case) is almost entirely captured by defects in the first 1-2 ps with a small fraction of the other carrier type (electrons in our case) being captured over much longer time scales.

## 4.10 Conclusion

In this chapter, we presented experimental results on the ultrafast dynamics of photoexcited carriers in monolayers of MoS<sub>2</sub> and showed that defect as-

sisted electron-hole recombination, in which carrier capture by defects occurs via Auger scattering, explains our observations very well. Based on the dependence of the measured data on the temperature and the pump fluence, we ruled out other mechanisms of non-radiative recombination and carrier capture by defects. Strong Coulomb interactions in two dimensional materials make Auger scattering effective. Our results will be helpful in understanding and evaluating the performance of MoS<sub>2</sub>-based electronic and optoelectronic devices.

CHAPTER 5  
ULTRAFAST PHOTORESPONSE OF MONOLAYER  $\text{MoS}_2$   
PHOTODETECTOR

## 5.1 Introduction

The strong light emission and absorption exhibited by single atomic layer transitional metal dichalcogenides in the visible to near-infrared wavelength range makes them attractive for optoelectronic applications. In this chapter, using two-pulse photovoltage correlation technique, we show that monolayer molybdenum disulfide photodetector can have intrinsic response times as short as  $3 \text{ ps}$  implying photodetection bandwidths as wide as  $300 \text{ GHz}$ . The fast photodetector response is a result of the short electron-hole and exciton lifetimes in this material. Recombination of photoexcited carriers in most two-dimensional metal dichalcogenides is dominated by non-radiative processes, most notable among which is Auger scattering. The fast response time, and the ease of fabrication of these devices, make them interesting for low-cost ultrafast optical communication links.

## 5.2 Motivations to use the TPPC technique

Two dimensional (2D) transition metal dichalcogenides (TMDs) have emerged as interesting materials for low-cost opto-electronic devices, including photodetectors, light-emitting diodes, and, more recently, lasers [94, 140, 170, 93, 89, 128, 180, 147, 4, 185, 174]. In the case of photodetectors, the response time and the

quantum efficiency are two important figures of merit. The intrinsic response time of TMD photodetectors and the ultimate limits on the speed of operation are unknown. The reported quantum efficiencies of TMD materials and devices are typically in the .0001-0.01 range [89, 180, 168, 147, 128, 7, 44, 4, 43], indicating that most of the electrically injected or optically generated electrons and holes recombine nonradiatively. Understanding the nonradiative carrier recombination mechanisms, as well as the associated time scales, is therefore important. Previously, ultrafast optical/THz pump-probe as well as ultrafast photoluminescence techniques have been used, by the authors and others, to study the ultrafast carrier dynamics in metal dichalcogenides and in molybdenum disulfide ( $\text{MoS}_2$ ) in particular [168, 135, 171, 137, 145, 76, 73, 34]. In these measurements, free-carrier recombination dynamics, exciton formation and recombination dynamics, refractive index changes, optical/THz intraband and interband conductivity changes, as well as the dynamics associated with carriers trapped in optically active midgap defects are all expected to play a role to varying degrees and, consequently, the results have been difficult to interpret and reconcile.

### 5.3 TPPC technique

In Two-pulse Photovoltage correlation (TPPC) measurements, a photodetector is excited with two identical optical pulses separated by a time delay and the integrated detector photoresponse (either photovoltage or photocurrent response) is recorded as a function of the time delay. TPPC thus uses the photodetector to perform an optical correlation measurement. The nonlinearity of the photoresponse with respect to the optical pulse energy enables one to determine

ultrafast intrinsic temporal response of the detector with sub-picosecond resolution [156, 116, 117, 51, 45, 146].

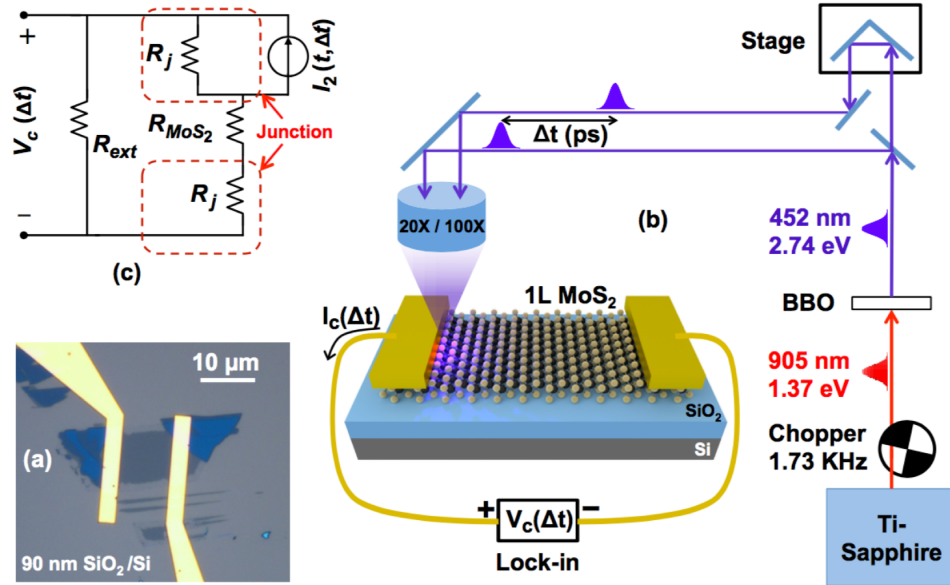


Figure 5.1: TPPC experiment setup. (a) Optical micrograph of a fabricated back-gated monolayer metal-MoS<sub>2</sub> photodetector on SiO<sub>2</sub>/Si substrate is shown. (b) A schematic of the two-pulse photovoltage correlation (TPPC) experiment is shown. Two time-delayed 452 nm optical pulses, both obtained via upconversion from a single Ti:Sapphire laser, are focused at one of the metal-semiconductor Schottky junctions. The generated DC photovoltage is recorded as a function of the time delay between the pulses. A lock-in detection scheme is used to improve the signal-to-noise ratio. The arrow indicates the positive direction of the photocurrent (and the sign of the measured photovoltage) from the illuminated metal contact. (c) A low-frequency circuit model of the device and measurement. The current source  $I_2(t, \Delta t)$  represents the short circuit current response of the junction in response to two optical pulses separated by time  $\Delta t$ .  $R_j$  is the resistance of the metal-MoS<sub>2</sub> junction.  $R_{\text{MoS}_2}$  is the resistance of the MoS<sub>2</sub> layer.  $R_{\text{ext}}$  is the external circuit resistance (including the  $\sim 10 M\Omega$  input resistance of the measurement instrument).

Microscope image of a monolayer metal-MoS<sub>2</sub> photodetector is shown in

Figure 5.1(a), and the schematic in Figure 5.1(b) depicts the setup for a two-pulse photocurrent/photovoltage correlation (TPPC) experiment. A  $\sim 80$  fs, 905 nm (1.37 eV) center wavelength, optical pulse from a  $\sim 83$  MHz repetition rate Ti-Sapphire laser is frequency doubled to 452 nm (2.74 eV,  $\sim 150$  fs) by a beta-BaB<sub>2</sub>O<sub>4</sub> crystal, then mechanically chopped at 1.73 KHz, and then split into two pulses by a 50/50 beam splitter. The time delay  $\Delta t$  between these two pulses is controlled by a linear translation stage. The resulting voltage across the photodetector is measured as a function of the time delay between the pulses using a lock-in amplifier with a 10 M $\Omega$  input resistance. In experiments, the maximum photoresponse was obtained when the light was focused on the sample near one of the metal contacts of the device, and the photoresponse decayed rapidly as the center of the focus spot was moved more than half a micron away from the metal contact. The direction of the DC photocurrent, and the resulting sign of the measured DC photovoltage are shown in Figure 5.1(b), and were determined without using the lock-in. Photovoltage was always positive at the contact near which the light was focused. Figure 5.1(c) shows a low-frequency circuit model of the device and the measurement. The circuit model shown can be derived from a high-frequency circuit model. If the time-dependent short circuit current response of the illuminated junction to a single optical pulse is  $I_1(t)$ , and to two optical pulses separated by time  $\Delta t$  is  $I_2(t, \Delta t)$ , and the external resistance  $R_{\text{ext}}$  is much larger than the total device resistance, then the measured DC voltage  $V_c(\Delta t)$  is approximately equal to  $(R_j/T_R) \int I_2(t, \Delta t) dt$ , where  $T_R$  is the pulse repetition period,  $R_j$  is the resistance of the metal-MoS<sub>2</sub> junction, and the time integral is over one complete period. As the time delay  $\Delta t$  becomes much longer than the duration of  $I_1(t)$ , one expects  $V_c(\Delta t)$  to approach  $(2R_j/T_R) \int I_1(t) dt$ .

## 5.4 Device fabrication and characterization

Monolayer MoS<sub>2</sub> samples were mechanically exfoliated from bulk MoS<sub>2</sub> crystal (obtained from 2D Semiconductors Inc.) and transferred onto highly n-doped Si substrates with 90 nm thermal oxide. Monolayer sample thickness was confirmed by Raman and reflection spectroscopies [79]. Au metal contacts (with a very thin Cr adhesion layer) were patterned and deposited onto the samples using electron-beam lithography. The doped Si substrate acted as the back gate. Microscope image of a 10×10 μm<sup>2</sup> area device is shown in Figure 5.1(a). Carrier densities and mobilities in the devices were determined using electrical transport measurements on devices of different dimensions. The devices were found to be n-doped with electron densities around  $1 \times 10^{12}$ - $2 \times 10^{12}$  cm<sup>-2</sup> (under zero gate bias). The intrinsic doping was attributed to impurities and defect levels [147]. The electron mobility in the devices was found to be in the 15 – 20 cm<sup>2</sup> V<sup>-1</sup>s<sup>-1</sup> range at 5K. The zero gate bias device resistance was typically less than 1 MΩ at all temperatures for a 10×10 μm<sup>2</sup> area device. While the device resistance decreased under a positive gate bias, no signature of hole conduction was observed even when a large negative gate bias was applied indicating that the Fermi level in the MoS<sub>2</sub> layer was likely pinned at defect levels within the bandgap under a negative gate bias. The devices were mounted in a helium-flow cryostat and the temperature was varied between 5K and 300K during measurements. The zero gate bias device resistance was found to be a function of the temperature and decreased almost linearly with the temperature from ~1 MΩ at 5K to values 5-7 times smaller at 300K. The total device resistance was dominated by the metal Schottky contacts to the device. For example, at 5K the resistance contributed by the 10×10 μm<sup>2</sup> area MoS<sub>2</sub> strip is estimated

to be in the 0.10-0.20  $M\Omega$  range (from the measured mobility values), which is approximately only one-tenth to one-fifth of the total device resistance. The reported Schottky barrier heights between similarly n-doped monolayer MoS<sub>2</sub> and Au/Cr contacts are in the 100-300  $meV$  range [147]. Depending on how strongly the Fermi level gets pinned at the defect levels in the bandgap, the lateral potential drop in the MoS<sub>2</sub> layer at the metal-MoS<sub>2</sub> interface (depicted in Figure 5.3(a)) could be equal to or smaller than the Schottky barrier height.

## 5.5 Experimental results

Figure 5.2(a) shows the measured two-pulse photovoltage correlation signal  $V_c(\Delta t)$  plotted as a function of the time delay  $\Delta t$  between the pulses. The substrate temperature is 5K, the gate bias is 0 V, and the pump fluence is  $8 \mu J cm^{-2}$ .  $V_c(\Delta t)$  is minimum when the two pulses completely overlap in time (i.e. when  $\Delta t = 0$ ). This implies, not surprisingly, that the photovoltage response of the detector to an optical pulse is a sublinear function of the optical pulse energy. As  $\Delta t$  increases from zero,  $V_c(\Delta t)$  also increases from its minimum value at  $\Delta t = 0$ . As  $\Delta t$  becomes much longer than the duration of the response transient of the detector to an optical pulse,  $V_c(\Delta t)$  approaches a constant value. The timescales over which  $V_c(\Delta t)$  goes to the constant value are related to the timescales associated with the response transient of the detector to an optical pulse. These timescales are better observed in the measured data if the magnitude of  $\Delta V_c(\Delta t)$ , defined as  $V_c(\Delta t) - V_c(\infty)$ , is plotted on a log scale, as shown in Figure 5.2(b). The plot in Figure 5.2(b) shows two distinct timescales: (i) a fast timescale of  $\sim 4.3 ps$ , and (ii) a slow timescale of  $\sim 105 ps$ . In different devices, the fast timescales were found to be in the 3-5  $ps$  range, and the slow timescales were in the 90-110  $ps$

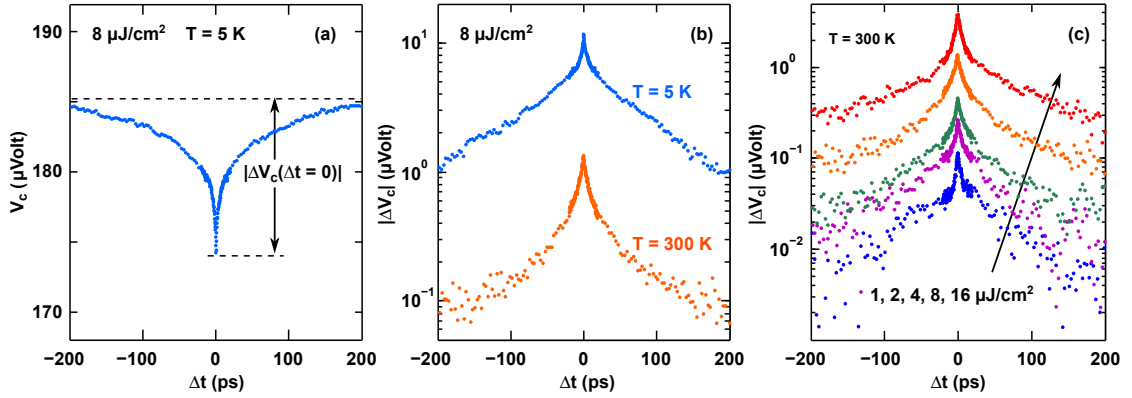


Figure 5.2: TPPC experiment results. (a) The measured two-pulse photovoltage correlation (TPPC) signal  $V_c(\Delta t)$  is plotted as a function of the time delay  $\Delta t$  between the pulses.  $T = 5\text{ K}$ . Gate bias is  $0\text{ V}$ . The pump fluence is  $8\ \mu\text{J}/\text{cm}^2$ . The quantity  $\Delta V_c(\Delta t)$  is the difference between  $V_c(\Delta t)$  and its maximum value which occurs when  $\Delta t \rightarrow \infty$ . (b)  $|\Delta V_c(\Delta t)|$  is plotted on a log scale as a function of the time delay  $\Delta t$  between the pulses in order to show the two distinct timescales exhibited by  $V_c(\Delta t)$ . The two curves are for two different extreme temperatures:  $T = 5\text{ K}$  and  $T = 300\text{ K}$ . The plot shows two distinct timescales: (i) a fast timescale of  $\sim 4.3\text{ ps}$ , and (ii) a slow timescale of  $\sim 105\text{ ps}$ . Gate bias is  $0\text{ V}$ . The pump fluence is  $8\ \mu\text{J}/\text{cm}^2$ . The two different timescales are observed at both temperatures and these timescales are largely temperature independent. (c) The measured two-pulse photovoltage correlation (TPPC) signal  $|\Delta V_c(\Delta t)|$  is plotted as a function of the time delay  $\Delta t$  between the pulses for different pulse fluences: 1, 2, 4, 8, and  $16\ \mu\text{J}/\text{cm}^2$ .  $T = 300\text{ K}$ . Gate bias is  $0\text{ V}$ . The two different timescales are observed at all values of the pump fluence and these timescales are not very sensitive to the pump fluence.

range. The fast timescales imply (8 dB) current modulation bandwidths wider than  $300\text{ GHz}$ . Measurements were performed at different temperatures and using different pump pulse fluences in order to understand the mechanisms behind the photoresponse and the associated dynamics. Figure 5.2(b) shows  $|\Delta V_c(\Delta t)|$  plotted for two different extreme temperatures:  $T = 5\text{ K}$  and  $T = 300\text{ K}$ . Gate bias is  $0\text{ V}$ . The pump fluence is  $8\ \mu\text{J}/\text{cm}^2$ . Two distinct timescales are ob-

served at both temperatures and these timescales are largely independent of the temperature. Measurements performed at intermediate temperatures provided the same results.  $|\Delta V_c(\Delta t)|$  was found to be larger at smaller temperatures. We attribute this to the increase in the metal-semiconductor junction resistance  $R_j$  at lower temperatures. Figure 5.2(c) shows  $|\Delta V_c(\Delta t)|$  plotted for different values of the pump pulse fluence. The pump pulse fluence was varied from 1 to 16  $\mu J cm^{-2}$ . Higher values of the pump fluence were not used in order to avoid optical damage to the sample [168].  $T = 300K$  and gate bias is 0 V. Figure 5.2(c) shows that the same two timescales are observed for all values of the pump fluence and these timescales are not very sensitive to the pump fluence. The observed timescales also did not change in any significant way under a positive or a negative gate bias. The internal and external detector quantum efficiencies were estimated from the measured values of  $V_c(\infty)$  and the junction resistance  $R_j$  to be in the 0.008-0.016 and 0.001-0.002 ranges, respectively.

The two different timescales observed in our two-pulse photovoltage correlation experiments match well with the two different timescales observed previously in ultrafast optical/THz pump-probe studies of carrier dynamics as well as in ultrafast photoluminescence studies of MoS<sub>2</sub> monolayers [168, 34]. It is therefore intriguing if the model for defect-assisted carrier recombination reported previously by the authors [168, 164] for explaining the ultrafast carrier dynamics in MoS<sub>2</sub> monolayers can be used to obtain photovoltage correlations that are in good agreement with the experimental results reported in this letter. We show below that this is indeed the case.

## 5.6 Ultrafast photoresponse of the metal-MoS<sub>2</sub> junction

Understanding the ultrafast photoresponse of the detector, and in particular the short circuit current response  $I_2(t, \Delta t)$ , is important for interpreting the experimental results. Figure 5.3(a) depicts the band diagram of the metal-MoS<sub>2</sub> junction (plotted in the plane of the MoS<sub>2</sub> layer) after photoexcitation with an optical pulse. Given the Schottky barrier height of 100-300 *meV* [147], the width of the MoS<sub>2</sub> region near the metal with a non-zero lateral electric field is estimated to be to  $\sim 100\text{-}300$  *nm* [112]. As a result of light diffraction from the edge of the metal contact, light scattering from the substrate, and plasmonic guidance, a portion of the MoS<sub>2</sub> layer of length equal to a few hundred nanometers is photoexcited even underneath the metal. The photoresponse of graphene photodetectors has been explained in terms of contributions from photovoltaic and photothermoelectric contributions [156, 116, 117, 51, 146, 59]. In our MoS<sub>2</sub> samples, the carrier mobilities and diffusivities are 2-3 orders of magnitude smaller than in graphene and the time period in which most of the photoexcited carriers recombine and/or are captured by defects is in the few picoseconds range [168, 164, 34, 76, 73]. Assuming similar mobilities and diffusivities of electrons and holes in MoS<sub>2</sub>, the photoexcited carriers, both free and bound (excitons), move, either by drift in the junction lateral electric field or by diffusion, less than  $\sim 10$  *nm* in 5 *ps* before they recombine and/or are captured by defects. The photoexcited carrier distributions therefore do not change significantly in space during their lifetime.

The ultrafast current response  $I_2(t, \Delta t)$  of a short circuited junction in response to two time-delayed optical pulses is expected to be fairly complicated. In TPPC experiments the quantity measured is the time integral  $\int I_2(t, \Delta t) dt$  ( $\propto$

$V_c(\Delta t)$ ). The motion of the photoexcited electrons and holes in a short circuited junction causes capacitive (i.e. displacement) currents in the external circuit in order to keep the potential across the shorted junction from changing in accordance with the Ramo-Shockley theorem [136, 120]. However, if the photoexcited carriers recombine before they make it out into the circuit then the net contribution of the capacitive currents to the integral  $\int I_2(t, \Delta t) dt$  is identically zero.

Photoexcited electrons and holes can be separated before they form excitons by the lateral electric field in the junction and this constitutes the standard drift current contribution to the detector short circuit current response  $\int I_2(t, \Delta t) dt$ . A photoexcited electron and a hole (free or belonging to an exciton) in the MoS<sub>2</sub> layer underneath the metal can also be separated at the metal-MoS<sub>2</sub> heterojunction. The hole can tunnel into the metal leaving behind the electron which is then swept by the lateral electric field to the opposite side of the junction. The electron can also tunnel into the metal leaving behind the hole which will then have a difficult time traversing the lateral field region (moving against the electric field) and making it to the opposite side of the junction. This argument shows that even if the probabilities of the electron and the hole tunneling into the metal are similar, the lateral field in the junction ensures that the process in which the hole tunnels into the metal makes the dominant contribution to the short circuit current response  $\int I_2(t, \Delta t) dt$ . The experimentally measured sign of the photovoltage, and the photocurrent (see Figure 5.1(b)), agrees with the above arguments.

The discussion above shows that the short circuit current response  $\int I_2(t, \Delta t) dt$  is proportional to the junction lateral electric field strength, and to the time integral of the photoexcited free electron and hole densities as well as to

the time integral of the bound (exciton) electron and hole densities. Assuming similar electron and hole mobilities, one may write,

$$\int I_2(t, \Delta t) dt \propto k_f \int [p'_f(t, \Delta t) + n'_f(t, \Delta t)] dt + k_b \int [p'_b(t, \Delta t) + n'_b(t, \Delta t)] dt \quad (5.1)$$

Here,  $n'_{f/b}(t, \Delta t)$  and  $p'_{f/b}(t, \Delta t)$  are the spatially-averaged free/bound (f/b) photoexcited electron and hole densities in the junction, respectively. Since photoexcited electrons and holes don't have time to move much before they recombine and/or are captured by defects, spatial dynamics of the carrier densities are not important. The constants  $k_f$  and  $k_b$  capture the difference in the relative contributions from free and bound carriers to the current response. If one assumes that  $k_f \approx k_b$  then,

$$\int I_2(t, \Delta t) dt \propto \int [p'(t, \Delta t) + n'(t, \Delta t)] dt \quad (5.2)$$

where  $n'(t, \Delta t)$  and  $p'(t, \Delta t)$  are the total photoexcited electron and hole densities in the junction, respectively, including carriers both free and bound (excitons). The assumption  $k_f \approx k_b$  will hold if the short circuit current is dominated by the free and bound electrons and holes that get separated at the metal-MoS<sub>2</sub> heterojunction. Since the junction resistance  $R_j$  is expected to be largely determined by the transport across the metal-MoS<sub>2</sub> heterojunction rather than by the transport across the MoS<sub>2</sub> region, the assumption  $k_f \approx k_b$  is a decent approximation if not an excellent one.

The above discussion, although simple, allows one to relate the measured photoresponse to the carrier dynamics and, as shown below, the results thus obtained are in excellent agreement with the experiments. We expect that on much longer timescales, when the photoexcited carriers have recombined or been captured, the photoresponse is entirely thermoelectric in nature, as is the

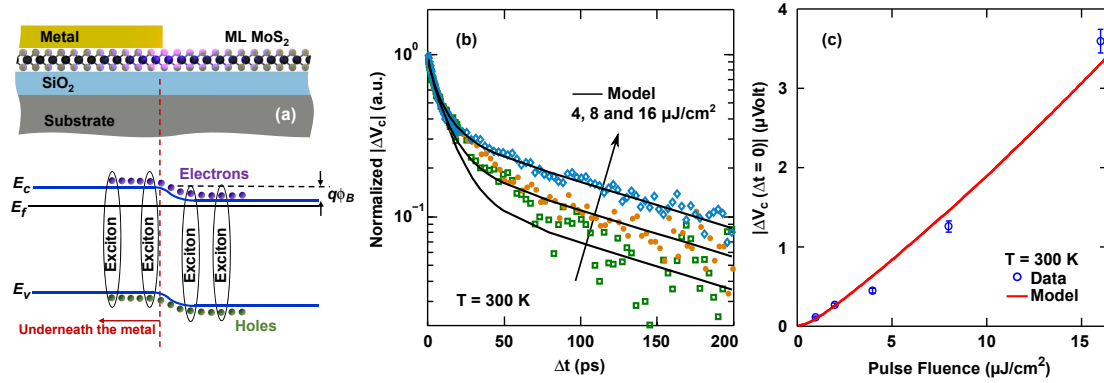


Figure 5.3: Theoretical modeling and fitting of TPPC experiment results. (a) The energy band diagram (bottom) of the the metal-MoS<sub>2</sub> junction (top) is plotted as a function of the position in the plane of the MoS<sub>2</sub> monolayer after photoexcitation with an optical pulse. The Schottky barrier height is  $\phi_B$ . The Figure is not drawn to scale. (b) The measured (symbols) and computed (solid lines) photovoltage correlation signals  $|\Delta V_c(\Delta t)|$ , normalized to the maximum value, are plotted as a function of the time delay  $\Delta t$  for different pump fluence values: 4, 8, and 16  $\mu J cm^{-2}$ .  $T = 300 K$ . The carrier capture model reproduces all the timescales observed in the measurements over the entire range of the pump fluence values used. (c) The scaling of the measured (symbols) and computed (solid line) values of  $|\Delta V_c(\Delta t = 0)|$  with the pump pulse fluence is shown. The error bars are the recorded peak-to-peak noise level of lock-in amplifier during each measurement.

case in metal-graphene photodetectors [156, 117, 51, 146, 59]. But in this letter we focus on the dynamics occurring on only short timescales.

## 5.7 Carrier capture/recombination model

It is known that most of the photoexcited carriers in monolayer MoS<sub>2</sub> recombine non-radiatively [168, 164, 43]. The temperature independence as well as the sample dependence of the recombination rates in previously reported works

suggested that free and bound (excitons) carriers recombine via capture by defects through Auger scattering [168, 164]. Monolayer MoS<sub>2</sub> can have several different kinds of defects, including grain boundaries, line defects, interstitials, dislocations and vacancies [42, 71, 37, 190, 107, 181, 85]. The strong electron and hole Coulomb interaction in monolayer TMDs makes defect capture via Auger scattering very effective [164]. The time constants observed in this work in the photovoltage correlations are also temperature independent (see Figure Figure 5.2(b)) and also match well with the time constants observed previously in optical/THz pump-probe and photoluminescence measurements [168, 34]. We therefore use the model for carrier capture by defects via Auger scattering in MoS<sub>2</sub> presented by Wang et al. [168, 164] to model our TPPC experimental results. The model assumes carrier capture by two different defect levels, one fast and one slow [168]. The essential dynamics captured by the model, and their relationships to the experimental observations, are as follows [168]. After photoexcitation, electrons and holes thermalize and lose most of their energy on a timescale much shorter than our experimental resolution ( $\sim 0.5\text{-}1.0$  ps) and, therefore, thermalization is assumed to happen instantly in our model [64]. Most of the photoexcited holes (both free and bound), followed by most of the electrons, are captured by the fast defects within the first few picoseconds after photoexcitation. During the same period, a small fraction of the holes is also captured by the slow defects. This rapid capture of the photoexcited electrons and holes is responsible for the fast time constant observed in our photovoltage correlation experiments. The remaining photoexcited electrons are captured by the slow defects on a timescale of 65-80 ps and this slow capture of electrons is responsible for the slow time constant observed in our photovoltage correlation experiments. We should point out here that the two time constants observed

in the photovoltage correlation signal  $\Delta V_c(\Delta t)$  are always slightly longer than the corresponding two time constants exhibited by the carrier densities in direct optical pump-probe and measurements [168], as is to be expected in the case of correlation measurements. Finally, the superlinear dependence of the carrier capture rates on the photoexcited carrier densities in the model, and therefore on the optical pulse energy, results in the experimentally observed negative value of the photovoltage correlation signal  $\Delta V_c(\Delta t = 0)$  at zero time delay.

The rate equations for the carrier densities and defect occupation probabilities with photoexcitation by two time-delayed optical pulses can be written as follows [168],

$$\frac{dn(t, \Delta t)}{dt} = -A_f n_f (1 - F_f) n^2 - A_s n_s (1 - F_s) n^2 + g I_p(t) + g I_p(t - \Delta t) \quad (5.3)$$

$$\frac{dp(t, \Delta t)}{dt} = -B_f n_f F_f n p - B_s n_s F_s n p + g I(t) + g I(t - \Delta t) \quad (5.4)$$

$$n_{f/s} \frac{dF_{f/s}(t, \Delta t)}{dt} = A_{f/s} n_{f/s} n^2 (1 - F_{f/s}) - B_{f/s} n_{f/s} n p F_{f/s} \quad (5.5)$$

Here,  $n(t, \Delta t)$  and  $p(t, \Delta t)$  are the total electron and hole densities, respectively, including both free and bound (excitons) carriers and  $n(t, \Delta t) = n_o + n'(t, \Delta t)$ , where  $n_o$  is the doping density.  $F_{f/s}$  are the defect occupation probabilities.  $A_{f/s}$  and  $B_{f/s}$  are the Auger capture rate constants for electrons and holes, respectively.  $n_{f/s}$  are the defect densities.  $I_p(t)$  is the optical pulse intensity ( $\mu\text{W cm}^{-2}$ ) and  $g$ , determined from the measured MoS<sub>2</sub> optical absorption at the wavelength of the optical pulse excitation, equals  $\sim 2.5 \times 10^{11} \text{ cm}^{-2} \mu\text{J}^{-1}$  and corresponds to around 11% absorption in monolayer MoS<sub>2</sub> on oxide at 452 nm wavelength [168]. In our n-doped sample, the defects are assumed to be fully occupied before photoexcitation. The above rate equations can be solved in time and the resulting photoexcited carrier densities integrated in time to yield the measured photovoltage correlation signal (up to a multiplicative constant). The values of the

$B_f n_f$	$0.73 \pm 0.05 \text{ cm}^2 \text{ s}^{-1}$
$B_s n_s$	$2.79 \pm 1 \times 10^{-2} \text{ cm}^2 \text{ s}^{-1}$
$A_s$	$9.5 \pm 1 \times 10^{-15} \text{ cm}^4 \text{ s}^{-1}$
$A_f$	$(1.0 \pm 0.2) B_f$
$n_{f/s}$	$5.0 \times 10^{12} \text{ cm}^{-2}$
$n_o$	$8 \times 10^{11} \text{ cm}^{-2}$

Table 5.1: Fitting parameters. Parameter values used in the simulations to fit the photovoltage correlation data.

fitting parameters used in the theoretical model to fit the experimental data are given in Table 1 and are almost identical to the values extracted previously from direct optical pump-probe measurements of the carrier dynamics in monolayer MoS<sub>2</sub> [168].

The comparison between the data and the model are shown in Figure 5.3(b) which plots the measured and computed photovoltage correlation  $|\Delta V_c(\Delta t)|$  as a function of the time delay  $\Delta t$  for different pump fluence values: 4, 8, and 16  $\mu\text{cm}^{-2}$ . All curves are normalized to a maximum value of unity (since the model gives the photovoltage correlation signal up to a multiplicative constant). The model not only reproduces the very different timescales observed in  $|\Delta V_c(\Delta t)|$  measurements, it achieves a very good agreement with the data over the entire range of the pump fluence values used in our experiments for the same values of the parameters. Figure 5.3(c) shows the scaling of the measured and computed values of  $|\Delta V_c(\Delta t = 0)|$  with the pump pulse fluence. Again, a very good agreement is observed between the model and the data.

## 5.8 Gate dependent TPPC measurements

The effect of the gate voltage on the photoresponse and the TPPC measurements is discussed here. Increasing the back gate voltage increases the electron density in the MoS<sub>2</sub> layer and raises the Fermi level with respect to the conduction band edge. However, in the region of the MoS<sub>2</sub> layer which is underneath the metal the electron density as well as the position of the Fermi level with respect to the conduction band edge remains unchanged. This is because the metal on top screens all the extra charges on the gate as the gate voltage is increased. Consequently, the in-plane lateral electric field in the MoS<sub>2</sub> layer increases near

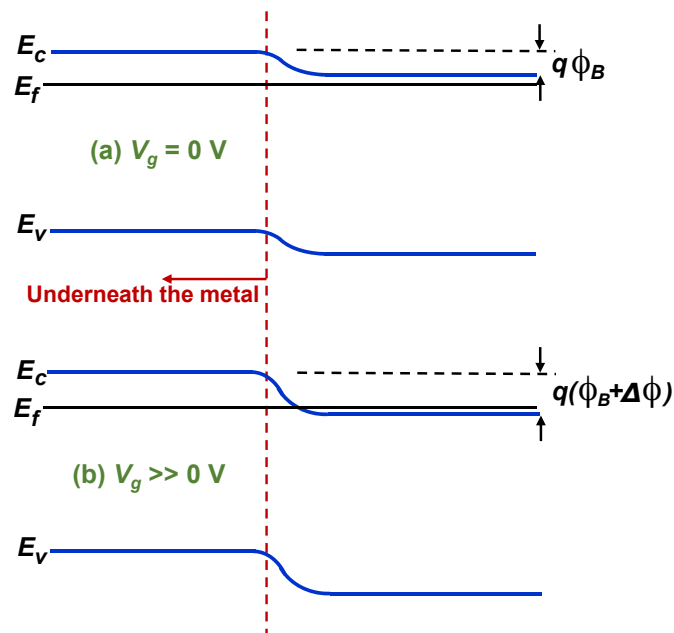


Figure 5.4: Band diagram of metal-MoS<sub>2</sub> junction. The effect of the gate voltage  $V_g$  on the energy band diagram of the the metal-MoS<sub>2</sub> junction is depicted when (a)  $V_g = 0$  V, and (b)  $V_g \gg 0$  V. The in-plane electric field increases near the metal junction with an increase in the gate voltage.

the metal junction with an increase in the gate voltage, as depicted in Figure

5.4. The exact magnitude of the increase in the in-plane electric field with the gate voltage is hard to predict since the result could depend on the degree of Fermi level pinning on defect states within the bandgap in MoS<sub>2</sub>. Nevertheless, one would expect the measured photoresponse to also increase with the gate voltage since, as argued in this paper, the photoresponse is proportional to the in-plane electric field [89].

Figure 5.5 shows the measured  $|\Delta V_c(\Delta t)|$  plotted as a function of the time delay  $\Delta t$  between the pulses for different gate bias values: -3, 0, 3, 6 V.  $T = 300K$ . The pump fluence is  $8 \mu Jcm^{-2}$ . As in Figure 5.2(b,c) in the article, two distinct time scales are observed in the dynamics and, within the accuracy of our measurements, these time scales are largely independent of the gate bias. As expected from our model, the overall signal level increases with the gate bias.

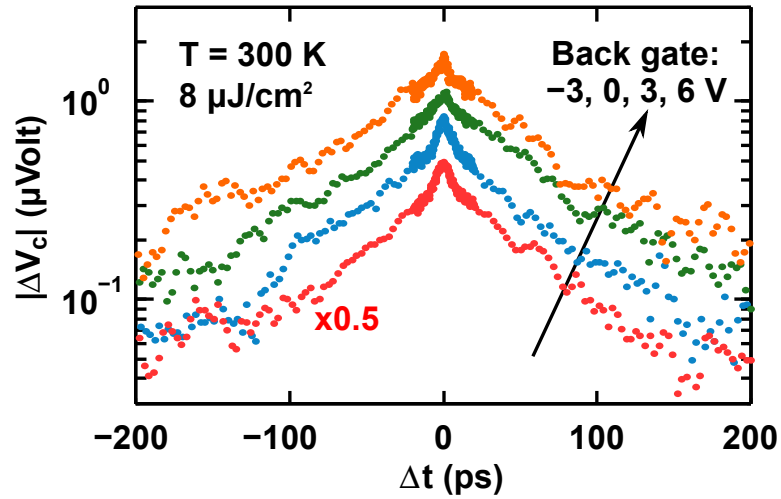


Figure 5.5: Gated TPPC experiment results. The measured two-pulse photovoltage correlation (TPPC) signal  $|\Delta V_c(\Delta t)|$  is plotted as a function of the time delay  $\Delta t$  between the pulses for different gate bias values: -3, 0, 3, 6 V.  $T = 300K$ . The pump fluence is  $8 \mu Jcm^{-2}$ . As in Figure 2(b,c) in the article, two distinct time scales are observed in the dynamics and these time scales are largely independent of the gate bias.

## 5.9 Simulation of photoexcitation at a metal-MoS<sub>2</sub> junction

A Finite Difference Time domain (FDTD) simulation of the optical excitation of a metal-MoS<sub>2</sub> junction by normally incident radiation is shown in Figure 5.6. The location of the MoS<sub>2</sub> layer is indicated by the dashed line. The simulation shows that as a combination of light diffraction from the edge of the metal contact, light scattering from the substrate, and plasmonic guidance, causes several hundred nanometers of MoS<sub>2</sub> to be photoexcited even underneath the metal.

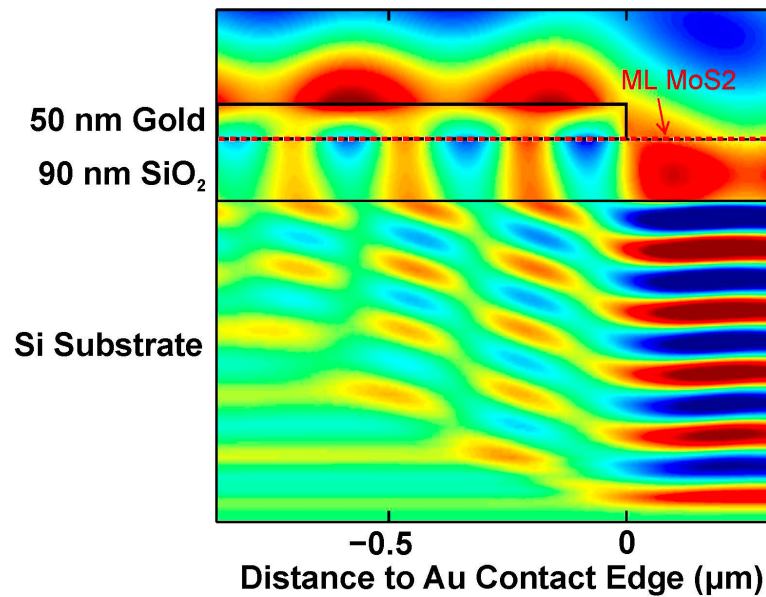


Figure 5.6: Numerical simulation of photoexcitation at metal-MoS<sub>2</sub> junction. Finite Difference Time domain (FDTD) simulation of the optical excitation of the metal-MoS<sub>2</sub> junction is shown. The location of the MoS<sub>2</sub> layer is indicated by the dashed line. The simulation shows that a portion of the MoS<sub>2</sub> layer of length equal to a few hundred nanometers is photoexcited even underneath the metal.

The photoexcitation simulations were performed by a C++ 2D/3D FDTD solver built from scratch. The motivation for building a new solver is that the commercial and open source FDTD solvers, such as Lumerical and MEEP, can-

not reach theoretical performance throughput due to their inefficient DRAM bandwidth utilization. Currently, the FDTD solver is still under active development, and is already 3 to 4 times as fast as commonly found numerical solvers.

## 5.10 Circuit models of the metal-MoS<sub>2</sub> junction

A circuit model of the photodetector is shown in Figure 5.7(a) and the resistances and capacitances associated with the metal-MoS<sub>2</sub> junction are shown in Figure 5.7(b). The time-dependent short circuit current response of the photodetector to two optical pulses separated by time  $\Delta t$  is  $I_2(t, \Delta t)$ . The short circuit current response  $I_2(t, \Delta t)$  represents the photocurrent measured if the illuminated junction were shorted. In our experiments, the quantity measured is the DC value  $V_c(\Delta t)$  of the open circuit voltage. Assuming periodic excitation of the device with the optical pulses,  $V_c(\Delta t)$  can be written as,

$$V_c(\Delta t) = \frac{1}{T_R} \frac{R_j R_{\text{ext}}}{R_d + R_{\text{ext}}} \int I_2(t, \Delta t) dt \approx \frac{R_j}{T_R} \int I_2(t, \Delta t) dt \quad (5.6)$$

Here, the total device resistance  $R_d$  equals  $2R_j + R_{\text{MoS}_2}$ ,  $T_R$  is the period of the optical excitation, and the time integrals above are performed over one complete period. The approximate equality above follows from the fact that in our experiments,  $R_{\text{ex}} \gg R_d$ . Note that all the capacitances drop out in the expression for  $V_c(\Delta t)$ . Therefore, one can use the low-frequency circuit model shown in Figure 5.1(c) when calculating  $V_c(\Delta t)$ .

It is instructful to determine whether the intrinsic device resistances and capacitances could fundamentally limit the high speed performance. The frequency dependent small-signal open circuit voltage response and short circuit current response of the detector can also be evaluated using the circuit shown

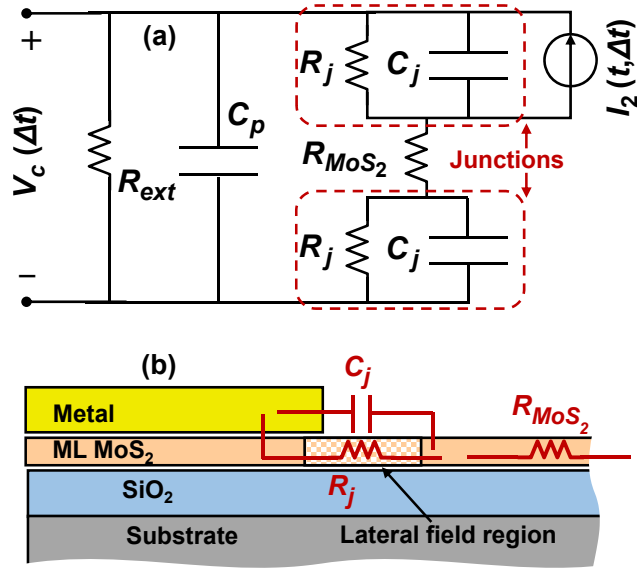


Figure 5.7: Circuit model of the metal-MoS<sub>2</sub> photodetector. A high-frequency circuit model of the photodetector is shown in (a). The resistances and capacitances associated with the metal-MoS<sub>2</sub> junction are depicted in (b).  $R_j$  and  $C_j$  are the resistance and the capacitance associated with the metal-MoS<sub>2</sub> junction.  $R_{\text{MoS}_2}$  is the resistance of the undepleted MoS<sub>2</sub> region.  $C_p$  is an external parasitic capacitance and  $R_{\text{ext}}$  is the external circuit resistance (including the input resistance of the measurement instrument).

in Figure 5.7(a) under the assumption that  $I_2(t) = \text{Re} \{i_2(\omega)e^{-i\omega t}\}$ . The open circuit voltage response is (assuming  $R_{\text{ext}} = \infty$ ),

$$\frac{v_c(\omega)}{i_2(\omega)} = \frac{R_j}{1 - i\omega C_j R_j - i\omega C_p(2R_j + R_{\text{MoS}_2}) + (i\omega)^2 C_p C_j R_j R_{\text{MoS}_2}} \quad (5.7)$$

If one ignores the parasitic capacitance  $C_p$  then the circuit bandwidth is set by the time constant  $R_j C_j$ . The junction resistance  $R_j$  is dominated by the metal-semiconductor contact resistance. In the case of MoS<sub>2</sub>, the contact resistance values are in the 1-10  $K\Omega\text{-}\mu\text{m}$  range at room temperature [66]. Because of the 2D nature of the metal-semiconductor junction, the junction capacitance  $C_j$  is very small and entirely due to the fringing fields. For a  $\sim 50$  nm thick metal contact

layer,  $C_j$  is estimated to be less than  $.03 \text{ fF}/\mu\text{m}$  [112]. Therefore, the relevant time constant is estimated to be shorter than a picosecond. The short circuit current response is (assuming  $R_{\text{ext}} = 0$ ),

$$\frac{i_{\text{ext}}(\omega)}{i_2(\omega)} = \frac{R_j}{2R_j + R_{\text{MoS}_2} - i\omega C_j R_j R_{\text{MoS}_2}} \quad (5.8)$$

In this case, the circuit bandwidth is set by the time constant  $C_j R_j R_{\text{MoS}_2} / (2R_j + R_{\text{MoS}_2})$ . If  $R_j \ll R_{\text{MoS}_2}$ , as would be the case if the doping in the  $\text{MoS}_2$  sheet is small, then the time constant equals  $\sim R_j C_j$ , which is the same as for the open circuit voltage response. If on the other hand  $R_j \gg R_{\text{MoS}_2}$ , then the time constant equals  $\sim 0.5 R_{\text{MoS}_2} C_j$ . Assuming an electron doping of  $\sim 2 \times 10^{12} \text{ cm}^{-2}$  (as in our devices) and a modest electron mobility of  $\sim 20 \text{ cm}^2/\text{V-s}$  (as in our devices), and a device length of  $1 \mu\text{m}$ , the value of  $R_{\text{MoS}_2}$  comes out to be  $\sim 150 \text{ K}\Omega\text{-}\mu\text{m}$  and the time constant comes out to be  $\sim 2.25 \text{ ps}$ . Finally, the capacitance  $C_p$  could come from the fringing fields between the two metal contacts and therefore its effect on the open circuit voltage response ought to be considered. For example, consider  $\sim 50 \text{ nm}$  thick metal contact layers that are one micron apart. The capacitance  $C_p$  is estimated to be less than  $.02 \text{ fF}/\mu\text{m}$  [46]. The relevant time constant is  $C_p(2R_j + R_{\text{MoS}_2})$  and, assuming  $R_j \ll R_{\text{MoS}_2}$ , the time constant is found to be  $\sim 3.0 \text{ ps}$ . Therefore, in all the cases the intrinsic device resistances and capacitances are not expected to fundamentally limit the speed of operation of the detectors considered in this work.

We have also performed electrostatic simulation to confirm our theoretical argument regarding the intrinsic device capacitance. The 2D electrostatic solver was built in Matlab, and the simulated electric field distribution is shown in Figure 5.8. From the electrostatic simulation in Figure 5.2, the intrinsic capacitance can be easily extracted by considering the electrostatic energy stored in

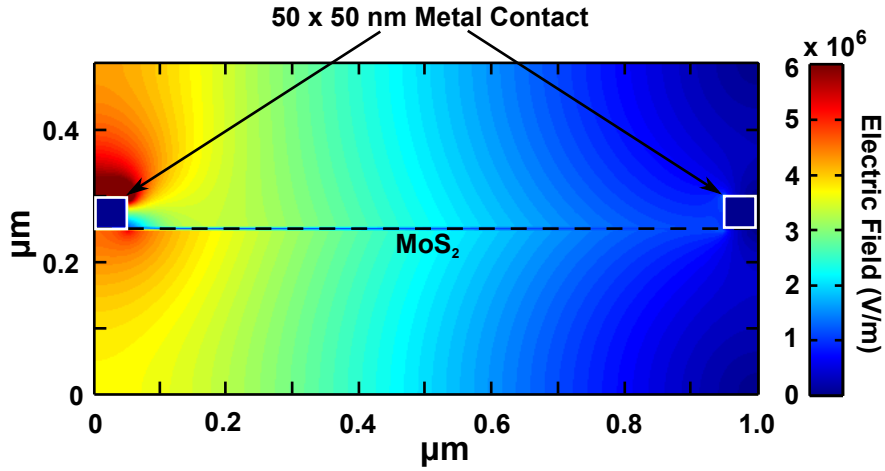


Figure 5.8: Electrostatic simulation of the monolayer MoS<sub>2</sub> photodetector. The bias voltage is 1V and symmetric boundary condition is used on the left boundary (the 1 V side), and zero field boundary condition was applied to the other three sides. The extracted intrinsic capacitance is  $\sim 0.03 \text{ fF}/\mu\text{m}$ .

the device:

$$E = \frac{1}{2}C \cdot V^2 = \frac{1}{2}\epsilon \int |E|^2 dx^3 \quad (5.9)$$

## 5.11 Sample variations

Lastly, we would like to discuss the TPPC experiments of the three samples we have measured. The time-resolved photovoltage data under  $8 \mu\text{J}/\text{cm}^2$  pump fluence at room temperature is show in Figure 5.9. Without changing the Auger capture coefficients, we were able to fit the transients from all three monolayer MoS<sub>2</sub> photodetectors using different slow trap densities:  $1 \sim 2 \times 10^{13}/\text{cm}^2$  for device A and B,  $\sim 5 \times 10^{12}/\text{cm}^2$  for device C. Defect density variation is random and could be caused by nano-fabrication processes. Note that the defect density of the fabricated monolayer MoS<sub>2</sub> photodetectors are higher than the as-exfoliated

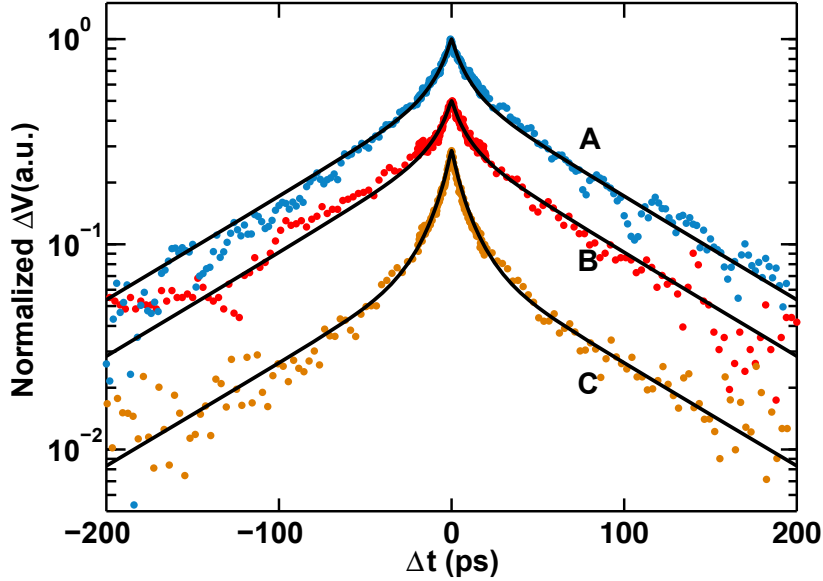


Figure 5.9: TPPC experiments on three different monolayer MoS<sub>2</sub> photodetectors. The experiments were performed under  $8 \mu\text{J}/\text{cm}^2$  pump fluence at room temperature. The black curves are the theoretical fittings with the same set of Auger capture coefficients but different slow trap densities:  $1 \sim 2 \times 10^{13}/\text{cm}^2$  for device A and B,  $\sim 5 \times 10^{12}/\text{cm}^2$  for device C.

samples in our OPOP work in Chapter 4. This result is a good indication that the Auger capture coefficients extracted from the theoretical model are physical.

## 5.12 Discussion

Our results reveal the fast response time and the wide bandwidth of metal-MoS<sub>2</sub> photodetectors and show that these detectors can be used for ultrafast applications. Our results also shed light on the carrier recombination mechanisms and the associated timescales. Although we focused mainly on the carrier dynamics in this paper, the device intrinsic resistances and capacitances are not expected to fundamentally limit the device speed because of the rather

small capacitances associated with the lateral metal-semiconductor junctions. An obstacle to using TMDs in practical light emission and detection applications is the small values of the reported quantum efficiencies in these materials [89, 180, 168, 147, 128, 7, 44, 4, 43]. In photodetectors, the response speed and the quantum efficiency are often inversely related [35]. In most semiconductor photovoltaic detectors with large carrier mobilities and long recombination times (e.g. group III-V semiconductor photodetectors [35]), the transit time of the photogenerated carriers through the junction depletion region determines the detector bandwidth [35]. Given the relatively small carrier mobilities and diffusivities in MoS<sub>2</sub>, the fast carrier recombination times determine the speed in our metal-MoS<sub>2</sub> detectors. The price paid for the the fast response time is the small internal quantum efficiency: most of the photogenerated carriers recombine before they make it out into the circuit. The best reported carrier mobilities in monolayer MoS<sub>2</sub> are an order of magnitude larger than in our devices and, therefore, metal-MoS<sub>2</sub> photodetectors with internal quantum efficiencies around 0.1 (approximately an order of magnitude larger than of our devices) are possible without sacrificing the wide bandwidth. Density of defects, which contribute to carrier trapping and recombination, is also a parameter that can be potentially controlled in 2D TMD optoelectronic devices to meet the requirements for ultrafast or high quantum efficiency applications. In addition, vertical heterostructures of 2D TMD materials can also be used to circumvent the transport bottleneck in high speed applications [97].

### 5.13 Conclusion

Our measurements show that the photovoltage is suppressed when the two optical pulses arrive together indicating a saturation of the photoresponse. As the time delay between the two pulses is increased from zero, the photovoltage recovers, and the recovery, as a function of the time delay, exhibits two distinct timescales: (i) a fast timescale of the order of 3 to 5 ps, and (ii) a slow timescale of around 80 to 110 ps. These two timescales are found to be largely independent of the temperature, exhibits only a mild dependence on the pump fluence, and varies a little from sample to sample. Between 50%-75% of the photovoltage correlation response recovers on the fast timescale implying that ultrafast TMD photodetectors with (8 dB) current modulation bandwidths in the 200-300 GHz range are possible. The fast response speed is a result of the short lifetime of the photoexcited carriers. Since TPPC measures the photovoltage (or photocurrent), this technique is sensitive only to the total photoexcited carrier population, including both bound (excitons) and free carriers, that contributes to the photoresponse. TPPC therefore also offers important and unique insights into the carrier recombination dynamics. The temperature and pump fluence dependence of our TPPC results are consistent with defect-assisted recombination as being the dominant mechanism, in which the the photoexcited electrons and holes, both free and bound (excitons), are captured by defects via Auger scattering [164]. Strong Coulomb interactions in 2D TMDs, including the correlations in the positions of free and bound electrons and holes arising from the attractive interactions, result in large carrier capture rates by defects via Auger scattering [164]. Our results underscore the trade-off between speed and quantum efficiency in TMD photodetectors.

CHAPTER 6  
SURFACE RECOMBINATION IN TRANSITION METAL  
DICHALCOGENIDES

## 6.1 Introduction

The ultrafast dynamics of photoexcited carriers and the non-radiative recombination mechanisms in monolayer TMDs, and in MoS<sub>2</sub> in particular, have been the subject of several recent experimental [168, 135, 171, 137, 145, 76, 73, 34] and theoretical studies [164]. Non-radiative electron-hole recombination in MoS<sub>2</sub> monolayers results in photoexcited carrier lifetimes in the few tens of picosecond range. In contrast, photoexcited carrier lifetimes in bulk MoS<sub>2</sub> have been shown to be in the few nanosecond range [142, 135]. This large difference between the carrier lifetimes in monolayer and multilayer 2D materials remains poorly understood. Shi et al. attributed this difference to the changes in the electronic bandstructure of MoS<sub>2</sub> going from monolayer, to few-layer, and to bulk [135].

Monolayer MoS<sub>2</sub> is known to have several different kinds of point defects, such as sulfur and molybdenum vacancies, interstitials, and adsorbed impurity atoms, in addition to grain boundaries and dislocations [42, 71, 37, 190, 107, 181, 85, 118, 159]. Recently, defect-assisted electron-hole recombination was proposed as the dominant non-radiative recombination mechanism in monolayer and bulk MoS<sub>2</sub> [168, 142, 164, 43]. The carrier density and the temperature dependence of the observed recombination dynamics suggest that photoexcited carriers are captured by defects via Auger processes [168, 142, 164]. It is reasonable to expect that surface layers of few-layer TMDs have far more defects

and impurities than the inner layers and, consequently, if defect-assisted processes are indeed responsible for electron-hole recombination in TMDs, then the recombination time would scale in some meaningful way with the number of layers in few-layer TMDs.

In this chapter, we discuss results for ultrafast carrier dynamics from non-degenerate optical pump-probe studies of few-layer MoS<sub>2</sub>. Our results show that the photoexcited carrier lifetimes increase dramatically from ~50 ps in monolayer MoS<sub>2</sub> to ~1 ns in 10-layer MoS<sub>2</sub>. The lifetimes were found to be largely temperature independent in all few-layer MoS<sub>2</sub> samples irrespective of the number of layers. The evolution of the carrier lifetime with the number of layers matches extremely well with our analytical model. The analytical model assumes a fast recombination time for the two surface layers in a few-layer sample, and a slow recombination time for all the inner layers, and then estimates the actual recombination time for a few-layer sample by weighing the inverse lifetime with the probability of electron occupation of each layer as given by the electron wavefunction in a few-layer sample. The good agreement between the measurements and the model shows that electron-hole recombination in few-layer MoS<sub>2</sub> is dominated by defect-assisted recombination processes in which the surface layers play an important role. In addition, the temperature and pump fluence dependence of the measured lifetimes are consistent with carrier capture by defects via Auger scatterings [164, 168, 142]. Reduction of carrier lifetimes in more traditional semiconductor nanostructures, such as quantum wells and wires, due to very large surface recombination velocities is well known [150, 92, 103, 133, 70], and surface passivation schemes have proven to be critical in the operation of optoelectronic devices based on these materials [177, 172, 30]. Our work underscores the importance of developing similar

passivation schemes for optoelectronic devices based on monolayer and multi-layer TMDs.

## 6.2 Carrier recombination dynamics in bulk MoS<sub>2</sub>

The carrier recombination dynamics in bulk MoS<sub>2</sub> was studied by Strait *et al.* [142] using ultrafast Optical Pump THz Probe (OPTP) technique. Very different from the monolayer OPOP data, the carrier lifetime of bulk MoS<sub>2</sub> varies from a few nanoseconds to tens of nanoseconds (tens of picoseconds in monolayer MoS<sub>2</sub>), with apparent pump fluence dependence. Through temperature and pump fluence dependent experiments, Strait *et al.* conclude that the photoexcited electron-hole pairs recombine mainly through defect assisted Auger scattering processes. The apparent pump fluence dependence in bulk MoS<sub>2</sub> is due to the low photoexcited carrier density in OPTP experiments ( $\sim 10^{10}/\text{cm}^2$  per layer in bulk vs  $\sim 10^{12}/\text{cm}^2$  in monolayer) as well as the absence of background carrier doping in bulk ( $\sim 10^{12}/\text{cm}^2$  in monolayer).

OPTP transients of bulk MoS<sub>2</sub> are plotted in Figure 6.1(a). The main conclusion is that the carrier recombination rate scales linearly as a function of photoexcited carrier density, which is consistent with the defect assisted Auger trapping model proposed in the monolayer OPOP work in Chapters 4 and 5. The much longer carrier lifetimes in bulk MoS<sub>2</sub> compared to monolayer MoS<sub>2</sub> lifetimes are due to: (1) the photoexcited carrier density per layer is much lower in bulk, resulting in a smaller defect Auger trapping rate, which scales linearly with the photoexcited carrier density; (2) the defect density of bulk MoS<sub>2</sub> is much lower compared to monolayer MoS<sub>2</sub>, which suffers from surface defects.

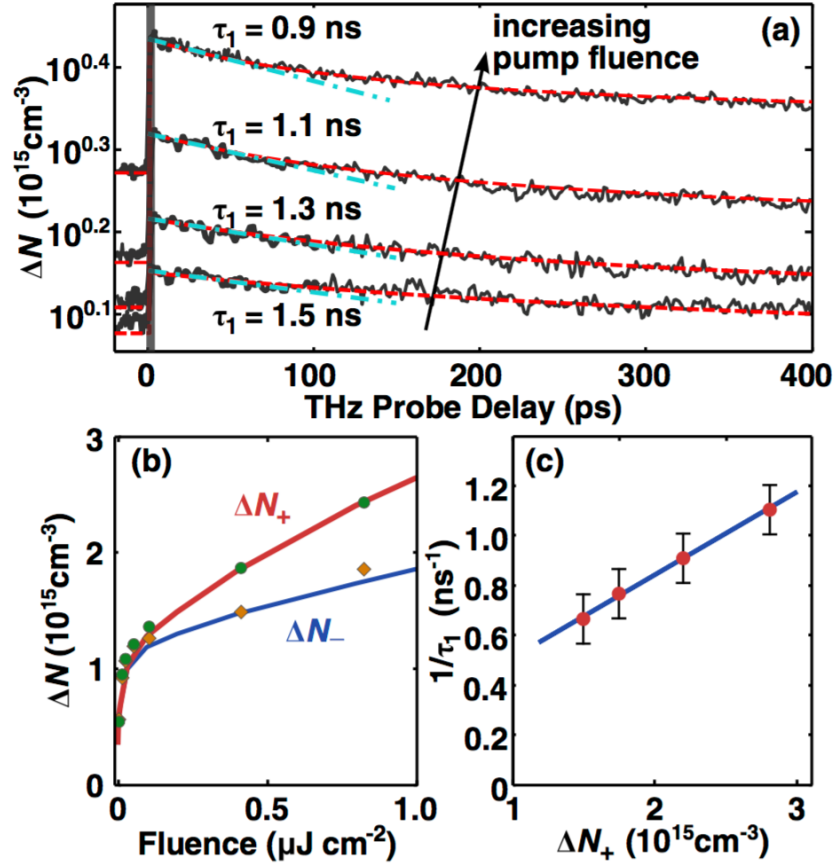


Figure 6.1: Pump fluence dependent OPTP measurements of bulk MoS<sub>2</sub> [142]. (a) OPTP transients for four pump fluences (0.2, 0.4, 0.8, 1.2  $\mu\text{J}/\text{cm}^2$ ) at 45 K. The time constants are the initial exponential relaxation time scale. (b) The Ti-sapphire laser has 81 MHz repetition rate, and pump pulses are separated by 12 ns in time. The slow carrier recombination (tens of nanoseconds) results in a background doping ( $\Delta N_-$ ) right before the photoexcitation.  $\Delta N_+$  is the photoexcited carrier density right after the photoexcitation. (c) Extracted carrier recombination rate has a linear dependence on the photoexcited carrier density.

Thus, we wonder if there is a consistent and unified model that can explain the carrier dynamics in MoS<sub>2</sub> samples from monolayer to bulk. The first task is to figure out at what thickness the MoS<sub>2</sub> sample can be considered to be bulk.

### 6.3 OPOP experimental set-up and sample preparation

Few-layer MoS<sub>2</sub> samples were mechanically exfoliated from bulk MoS<sub>2</sub> crystals (obtained from 2D Semiconductors Inc.) and transferred onto quartz substrates. Exfoliated samples were characterized electrically and optically, using transmission/reflection spectroscopies, to determine both the electronic and optical conductivities [168]. The monolayer samples were found to be moderately n-doped ( $> 10^{12} \text{ 1/cm}^2$ ) and the multilayer samples were found to be lightly n-doped ( $2\text{--}4 \times 10^{15} \text{ 1/cm}^3$ ), consistent with previously reported results [79, 142, 168, 185]. The thicknesses of the samples were measured by AFM to determine the number of layers [94]. In the nondegenerate ultrafast optical pump-probe (OPOP) experiments,  $\sim 80 \text{ fs}$  pulses at  $905 \text{ nm}$  ( $1.37 \text{ eV}$  photon energy) were frequency-doubled to  $452 \text{ nm}$  ( $2.74 \text{ eV}$ ) by a beta-BaB<sub>2</sub>O<sub>4</sub> crystal. The  $452 \text{ nm}$  pump pulses were used to excite electrons from the valence band into the conduction band in the samples. The differential transmission ( $\Delta T/T$ ) of time-delayed  $905 \text{ nm}$  probe pulses was measured using a chopped lock-in technique. A 20X objective was used to focus the pump and the probe pulses onto the samples. The OPOP experiment is illustrated in Figure 6.2(a). The bandstructure of multilayer MoS<sub>2</sub> is shown in Figure 6.2(b), which depicts the carrier excitation process [94, 188].

The measured optical conductivities (real part) for different layer numbers are normalized to the layer number and shown in Figure 6.2(c). The real and imaginary parts,  $\sigma_r$  and  $\sigma_i$ , respectively, of the optical conductivity of few-layer TMDs can be obtained by measuring their transmission and reflection spectra. Measured transmission and reflection spectra of few-layer MoS<sub>2</sub>, with respect to the quartz substrate, are shown in Figure 6.3(a,b) for different layer numbers. The real part of the 2D optical conductivity  $\sigma_r$  can be expressed in terms of these

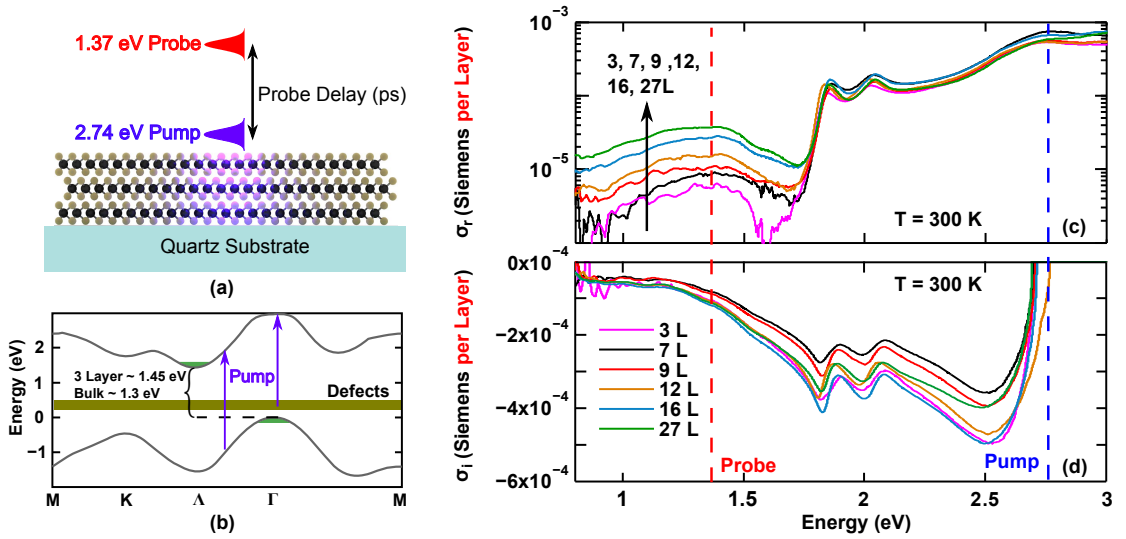


Figure 6.2: Optical conductivity and photoexcitation in few layer MoS<sub>2</sub>. (a) Nondegenerate ultrafast optical-pump optical-probe (OPOP) experiment on few-layer MoS<sub>2</sub>. (b) Bandstructure of few-layer MoS<sub>2</sub> and depiction of electron photoexcitation from the valence band and midgap defect states into the conduction band. (c)(d) The measured optical conductivities (real part(c) and imaginary part(d)) of few-layer MoS<sub>2</sub> samples are normalized to their layer numbers and plotted.

two measurements as follows (details can be found in Chapter 2):

$$\sigma_r(\omega) = \frac{(1 + n_s)^2 - (1 - n_s)^2 R(\omega)}{4\eta_o T(\omega)} - \frac{n_s}{\eta_o} \quad (6.1)$$

The interband optical conductivity (above ~1.9 eV) is seen to scale almost linearly with the number of layers. A weak absorption band was observed in all multilayer samples in the 0.8-1.6 eV range. Interestingly, this absorption band was not observed in monolayer samples [168]. We rule out indirect interband absorption as being solely responsible for this absorption band as the band extends to energies much smaller than the indirect bandgap even in our thickest samples [36, 94]. Since all our samples were n-doped, this absorption could be due to optical transitions from midgap defect states to the conduction band, or

to the optical transitions from the lowest conduction band to higher conduction bands.

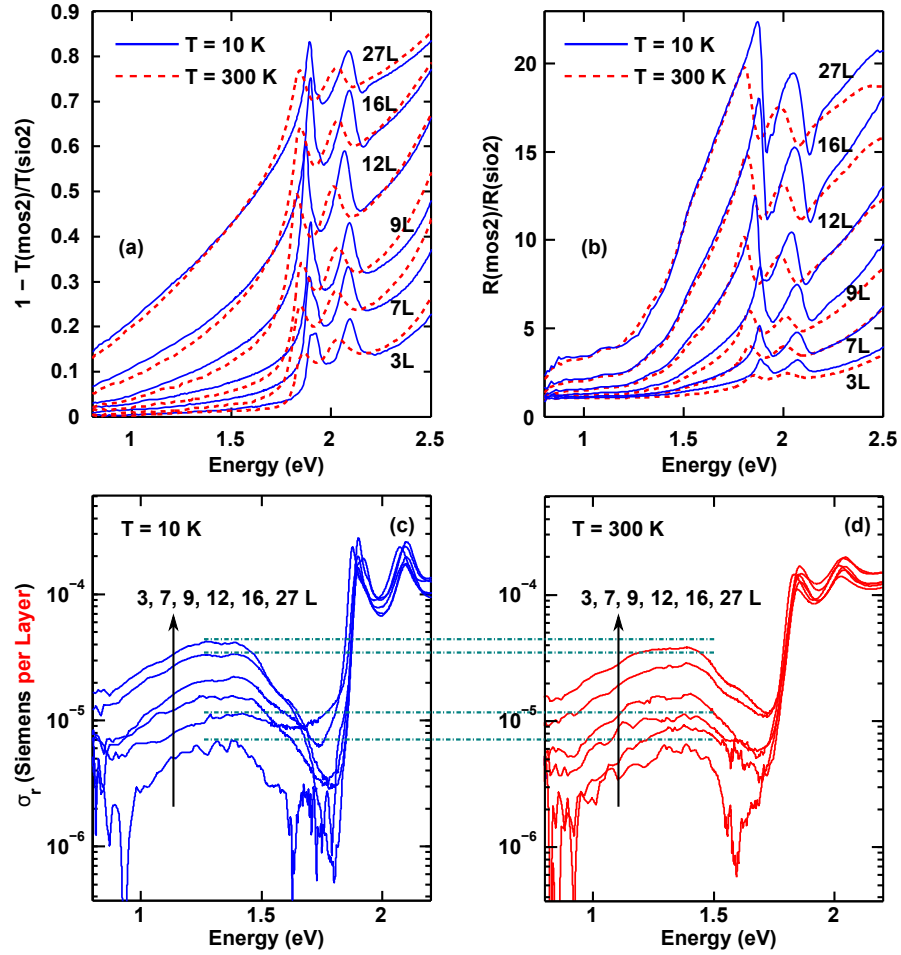


Figure 6.3: Temperature dependent optical conductivity measurements. (a,b) Temperature dependent transmission and reflection measurements on few-layer MoS<sub>2</sub>. (c,d) Real part of the optical conductivity of few-layer MoS<sub>2</sub>. Temperature dependent  $\sigma_r$  is normalized to the number of layers and obtained from transmission and reflection measurements.

The temperature dependent optical conductivity in Figure 6.3(c,d) is consistent with the scenario that the below band gap  $\sigma_r$  comes from the midgap defect state absorption. At cryogenic temperatures, the background carrier doping density is lower since dopants cannot be easily ionized thermally. If the

midgap  $\sigma_r$  came from inter-subband transitions,  $\sigma_r$  should be smaller at 10 K due to the lower carrier density. From Figure 6.3(c,d),  $\sigma_r$  is actually larger at 10 K compared to the data at 300 K. The alternative explanation is that, since the defect state is more filled with electrons at 10 K, the midgap defect absorption is stronger.

Lastly, from the optical conductivity measurements, a  $1 \mu J cm^{-2}$  fluence pump pulse is estimated to generate an electron (and hole) density that varies from  $\sim 2.5 \times 10^{11} cm^{-2}$  in monolayer to  $\sim 1.5 \times 10^{11} cm^{-2}$  per layer in a 10-layer MoS<sub>2</sub> sample. The measurement time resolution was  $\sim 300$ - $350$  fs, and was limited by the dispersion of the optics in the setup. The maximum probe delay was limited by our setup to  $\sim 1$  ns. The goal of the experiment was to use the free-carrier absorption of the probe pulse by the photoexcited electrons and holes to monitor their temporal dynamics. The same technique was used in Chapter 4 to study the ultrafast dynamics of photoexcited carriers in monolayer MoS<sub>2</sub> [168].

## 6.4 Experimental results and discussion

Measured differential transmission transients  $\Delta T/T$  for few-layer samples (4-layer and 10-layer) are shown in Figure 6.4(a)-(b) for two different temperatures. The results for monolayer samples were reported in previous work [168], and the results shown in Figure 6.4(a)-(b) are representative of all multilayer samples studied in this work. The results for multilayer samples exhibit the following three prominent features: (a) Near zero probe delay,  $\Delta T/T$  dips negative for a duration shorter than  $\sim 0.5$  ps. We attribute this dip to two-photon absorption between the pump and probe pulses when they overlap. The duration and

shape of the dip are both consistent with this interpretation. The magnitude of the dip is very sensitive to the degree of overlap between the pump and probe pulses. (b)  $\Delta T/T$  then immediately turns positive for a duration that can last anywhere from a few picoseconds to more than ten picoseconds and the duration was found to have no meaningful dependence on the layer number. This portion of the transient is temperature dependent, becoming larger at smaller temperatures, and is absent in monolayer samples [168]. (c) Finally,  $\Delta T/T$  turns negative and this last portion of the transient exhibits time scales that are independent of the temperature and vary from tens of picoseconds to more than a nanosecond, becoming longer for samples with larger number of layers. These time scales can be seen more clearly in Figure 6.4(c) which plots the magnitude of the transients on a log scale (after rescaling them for clarity). The observed time scales exhibit an interesting relationship with the number of layers in the sample and this relationship is discussed in detail later in the paper.

We first discuss different physical mechanisms contributing to  $\Delta T/T$  in our measurements. The measured differential transmission  $\Delta T/T$  of the probe pulse can be expressed as [168],

$$\frac{\Delta T}{T} \approx -\frac{2\eta_o \frac{\Delta\sigma_r}{1+n_s} + 2\eta_o^2 \frac{\sigma_r \Delta\sigma_r + \sigma_i \Delta\sigma_i}{(1+n_s)^2}}{\left|1 + \eta_o \frac{\sigma_r + i\sigma_i}{1+n_s}\right|^2} \quad (6.2)$$

where  $\sigma_r(\sigma_i)$  is the real(imaginary) part of intraband optical conductivity (units: Siemens),  $n_s$  is the refractive index of  $\text{SiO}_2$  and  $\eta_o$  is the vacuum impedance. The positive part of the transient is attributed to the decreased probe absorption by the optically active midgap defect states due to pump induced ionization of these defect states, and it is described by a negative value of  $\Delta\sigma_r$ . The rather long relaxation times associated with the positive part of the transient rule out bleaching of the probe intraband absorptions by the pump pulse as the cause of

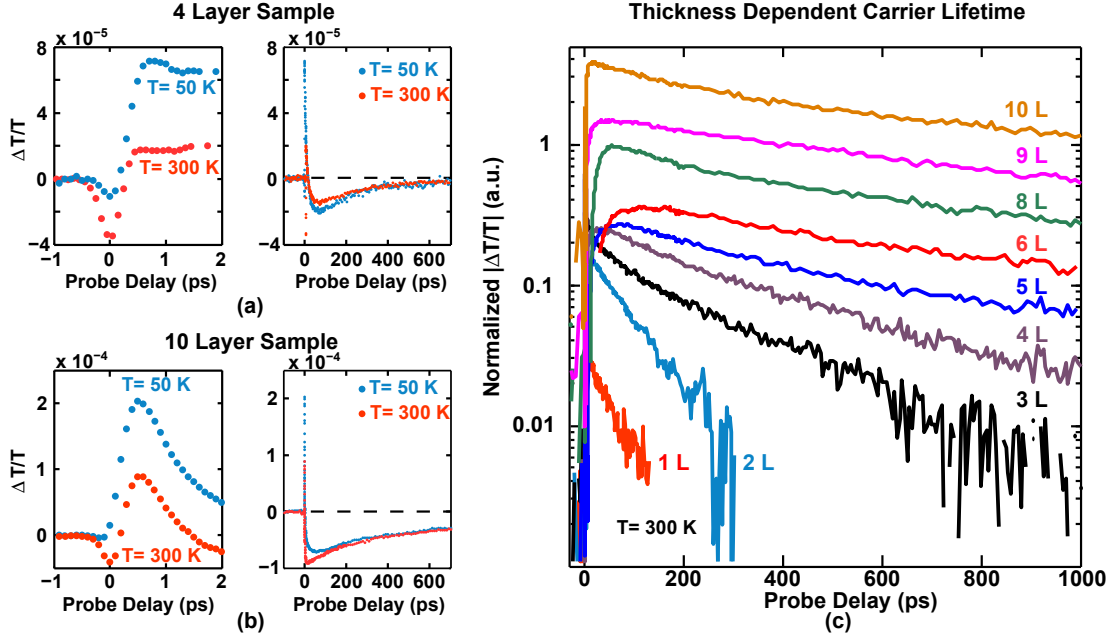


Figure 6.4: OPOP transients of few layer MoS<sub>2</sub> samples. (a,b) Measured differential transmission transients ( $\Delta T/T$ ) of few-layer MoS<sub>2</sub> ((a) 4-layer and (b) 10-layer as representatives of all measured samples) are plotted at different time scales and for different substrate temperatures. The negative dip in  $\Delta T/T$  near zero probe delay is attributed to two-photon absorption between the pump and probe pulses. The positive part of  $\Delta T/T$  right after photoexcitation comes from the decreased defect absorption of the probe pulse caused by the ionization of the defects by the pump pulse. The long negative part of  $\Delta T/T$ , which lasts from tens of picoseconds to nanoseconds, is due to the intraband absorption of the probe pulse by the photoexcited carriers. The time scales exhibited in the long negative part of  $\Delta T/T$  are temperature independent. (c) The magnitude of long negative  $\Delta T/T$  transients are plotted on a log scale to show the dependence of the time scales on the layer number. Different curves are scaled in magnitude for clarity. Pump fluence was  $32 \mu\text{J}/\text{cm}^2$  in all measurements.

the positive part of the transient. Another mechanism that can contribute to a negative value of  $\Delta\sigma_r$  is Pauli blocking of the indirect interband absorption of the probe pulse by the photoexcited carriers. The latter is ruled out because a

strong negative contribution to the value of  $\Delta\sigma_r$ , is observed even in bilayer and trilayer samples in which the measured indirect bandgaps (1.6 eV for bilayer and 1.45 eV for trilayer [94]) are much larger than the 1.37 eV probe photon energy. In addition, the positive part of the  $\Delta T/T$  transient is absent in monolayer samples [168], which is consistent with no measurable midgap defect absorption in monolayer MoS<sub>2</sub> [168]. The larger magnitudes of the positive part of  $\Delta T/T$  at lower temperatures, seen in Figure 6.4(a)-(b), are attributed to the larger initial occupation of the midgap defect states by electrons in our lightly n-doped materials at lower temperatures and this is consistent with a larger measured value of the real part of the optical conductivity for these midgap defects at lower temperatures (see Figure 6.3). The final negative part of the transient is attributed to intraband absorption of the probe pulse by the photoexcited carriers and is described by a positive value of  $\Delta\sigma_r$ . The Drude component of the intraband absorption by the photoexcited carriers is described by the conductivity change [168],

$$\Delta\sigma_r + i\Delta\sigma_i \approx e^2 \left( \frac{1}{\omega^2\tau_d} + \frac{i}{\omega} \right) \left( \frac{\Delta n}{m_e} + \frac{\Delta p}{m_h} \right) \quad (6.3)$$

Here,  $\Delta n$  ( $\Delta p$ ) is the photoexcited electron (hole) density in the conduction (valence) band,  $\omega$  is the probe optical frequency, and  $\tau_d$  is the carrier momentum scattering time (assumed to be the same for both electrons and holes). The final negative part of the transient is related directly to the density of the photoexcited electrons and holes in the bands and enables one to measure the time scales associated with electron-hole recombination, as discussed in detail below.

The refractive index response is given by the changes in the imaginary part of the optical conductivity which can affect the probe transmission through the term containing the product  $\sigma_i\Delta\sigma_i$  in Eq. 6.2. The measured imaginary part of the optical conductivity  $\sigma_i$  of MoS<sub>2</sub> for different number of layers is shown in

Figure 6.2(d).  $\sigma_i < 0$  at the probe wavelength. Since the intraband (see Eq. 6.3) as well as the interband contributions to  $\Delta\sigma_i$  from the photoexcited free-carriers are both positive [38, 17], the contribution to  $\Delta T/T$  from  $\Delta\sigma_i$  will also be positive which is not consistent with the long negative part of the measured  $\Delta T/T$  transient. Note that the magnitude of the product  $\eta_o\sigma_i$ , which appears with  $\Delta\sigma_i$  in Eq. 6.2, is much less than unity at the probe wavelength for all MoS<sub>2</sub> samples considered in this work. Therefore, the contribution from the real part of the conductivity, as given by the first term on the right hand side in Eq. 6.2, dominates the measured response. Finally, one also needs to consider the effect of the temperature on the refractive index or, equivalently, on the imaginary part of the optical conductivity. In most semiconductors, an increase in the temperature results in an increase in the refractive index and a decrease (more negative) in the imaginary part of the conductivity [62, 17]. Consequently, an increase in the sample temperature by the pump pulse would result in a negative contribution to the value of  $\Delta T/T$ . If the measured negative part of the  $\Delta T/T$  transient in our experiments were due to temperature relaxation, then the associated time scale, determined by the ratio of the material heat capacity and the relevant thermal conductivity, would be independent of the pump fluence. However, as we show below, the measured time scales depend on the pump fluence consistent with defect-assisted recombination of photoexcited carriers via Auger scatterings [168]. Therefore, temperature relaxation can also be ruled out as a dominant contributing factor to the measured  $\Delta T/T$  transients.

## 6.5 Carrier recombination model

Models for electron-hole recombination (involving free-carriers as well as excitons) by defect-assisted processes in which carrier capture by defects occurs via Auger scattering have been presented by the authors in previous works [168, 164, 142], and used successfully to model the carrier recombination dynamics in monolayer and bulk MoS<sub>2</sub> samples [168, 142]. A prominent feature of Auger scattering is recombination times that are independent of the temperature but depend on the carrier density (or the pump fluence). In all the MoS<sub>2</sub> samples studied in this work, we observe this feature in the long negative  $\Delta T/T$  transients. Therefore, following our earlier work [168, 142], we model the recombination dynamics with electron and hole defect capture rates,  $R_e$  and  $R_h$ , respectively, that are given by the following expressions valid for our n-doped samples:  $R_e = An^2n_d(1 - F_d)$  and  $R_h = Bnpn_dF_d$ . Here,  $n$  ( $p$ ) is the electron (hole) density,  $n_d$  is the defect density,  $F_d$  is the defect occupation probability, and  $A$  and  $B$  are rate constants for Auger scattering. Figure 6.5(a) shows the good agreement between the recombination model and the measured  $\Delta T/T$  transients for the long negative part of the transients for different pump fluence values. The details of the recombination model in Figure 6.5(a) are discussed in our previous work [142]. If the photoexcited carrier density is much larger than the defect density  $n_d$  and the equilibrium carrier density, then it can be shown that for multilayer samples the carrier recombination dynamics can be described by the following Equation (see the supplementary information),

$$\frac{dn}{dt} \approx \frac{dp}{dt} \approx -\frac{(An_d)(Bn_d)}{An_d + Bn_d} np \quad (6.4)$$

It is the product of the rate constant and the defect density that determines the recombination rates. According to the above Equation, the initial inverse

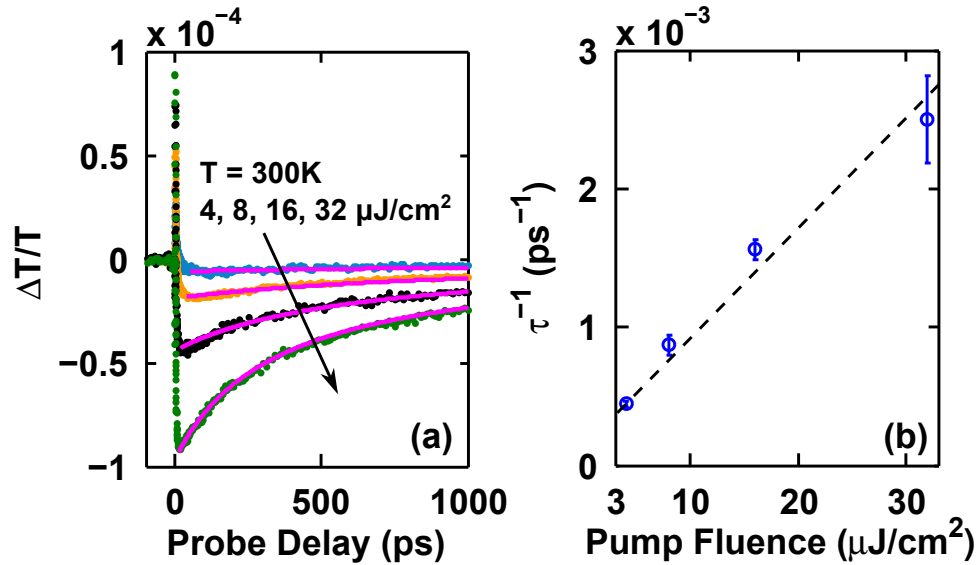


Figure 6.5: Pump fluence dependent OPOP experiments of a 10-layer  $\text{MoS}_2$  sample. (a) (Dots) Measured differential transmission transients  $\Delta T/T$  of a 10-layer  $\text{MoS}_2$  sample are plotted for different values of the pump fluence (4, 8, 16, 32  $\mu\text{J}/\text{cm}^2$ ).  $T=300\text{K}$ . (Solid lines) Theoretical model for electron-hole recombination by defect-assisted processes in which carrier capture by defects occurs via Auger scattering. (b) The observed inverse carrier lifetime  $1/\tau$  right after photoexcitation scales linearly with the photoexcited carrier density and, therefore, with the pump fluence. The recombination model fits the data very well. The vertical offset in the data at zero pump fluence is attributed to the light n-doping in our sample.

carrier lifetime  $1/\tau$  after photoexcitation is expected to scale linearly with the photoexcited carrier density and, therefore, with the pump fluence. The extracted initial inverse carrier lifetimes  $1/\tau$  plotted in Figure 6.5(b) are seen to scale almost linearly with the pump fluence, as expected from the model. The vertical offset in Figure 6.5(b) at zero pump fluence is attributed to the light n-doping in our samples. Note that none of our measurements rule out or affirm if the defects responsible for electron-hole recombination are the same midgap defects whose signature appears in the optical absorption spectra discussed above.

Photoexcited carrier dynamics in monolayer MoS<sub>2</sub> are not adequately described by the above Equation [168]. In the case of monolayer MoS<sub>2</sub>, fast defects contribute to rapid electron-hole recombination in the first few picoseconds and carrier recombination dynamics on long time scales are described by slow defects. A more detailed discussion of the carrier dynamics in monolayer samples is given previously by Wang et al. [168]. In Figure 6.4(c), only the portion of the transient governed by the slow defects is visible for the monolayer sample.

## 6.6 Scaling of the carrier Lifetime with the number of layers:

We now explore the dependence of the carrier lifetime  $\tau$  on the number of layers. The carrier lifetime, extracted from the data shown in Figure 6.4(c), is plotted in Figure 6.6(a) as a function of the number of layers. The lifetime increases rapidly from  $\sim 50$  ps in a monolayer sample to  $\sim 500$  ps in a 5-layer sample and then the rate of increase slows down and the lifetime value equals  $\sim 1.0$  ns in a 10-layer sample. These lifetime values are consistent with the results obtained earlier by the authors for monolayer and bulk samples [168, 142]. The question that arises is why the lifetimes vary so drastically between monolayer and multilayer samples and if any simple model can capture the seemingly complicated evolution of the lifetimes with the number of layers. Monolayer and multilayer MoS<sub>2</sub> samples have different bandstructures and, therefore, different conduction and valence band Bloch states for electrons and holes [94, 22, 188]. However, the bandstructures of few-layer MoS<sub>2</sub> for different number of layers are not that different from each other when the number of layers is greater than or equal to two, and even the bandgaps of few-layer MoS<sub>2</sub> quickly converge to the bulk values in just 4-5 layers [94]. Therefore, we rule out the variation in

the measured carrier lifetimes as coming from bandstructure changes with the layer number.

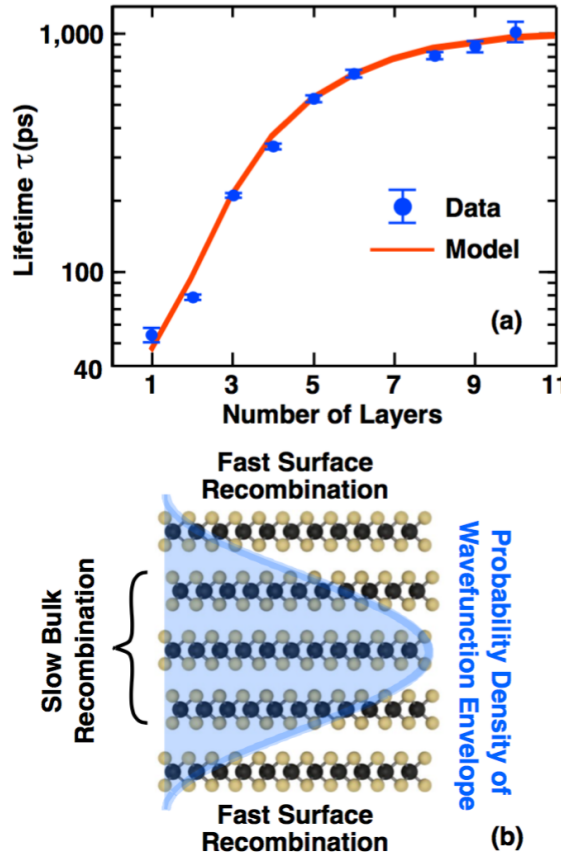


Figure 6.6: Carrier lifetime model. (a) (Dots) Carrier lifetime  $\tau$ , extracted from the data in Figure 6.4(c), is plotted as a function of the number of layers. For each data point the pump fluence used was  $32 \mu\text{J}/\text{cm}^2$  and  $T=300\text{K}$ . (Solid lines) Theoretical model. The evolution of the carrier lifetime with the number of layers can be explained well by the competition between surface and bulk recombination, as explained in the text. The errorbars represent upper and lower bounds of the extracted lifetimes. (b) A depiction of the different recombination times in the bulk and at the surfaces of a few-layer MoS<sub>2</sub> sample. The solid line shows the probability density associated with the carrier envelope wavefunction in the few-layer sample.

A possible difference between monolayer and few-layer MoS<sub>2</sub> is the possibility of substantially more defect states, acting as recombination centers, present

at the surfaces compared to in the bulk. Drastic reduction of carrier lifetimes and photoluminescence quantum efficiencies in more traditional semiconductor nanostructures, such as quantum wells and wires, due to very large surface recombination velocities is well known [150, 92, 103, 133, 70]. One might assume, as the simplest model, that all recombination occurs at the two surface layers in few-layer MoS<sub>2</sub> and no significant recombination occurs in the bulk. This would mean that the carriers photoexcited in the bulk would have to diffuse to the surfaces in order to recombine and carrier lifetimes would then be diffusion limited and sample thickness dependent. Diffusion time in a clean disorder-free material sample goes as the square of the sample thickness [138] whereas the lifetimes in Figure 6.6(a) have a very different, and much stronger, dependence on the film thickness (or the number of layers). Diffusion time in disordered materials (with correlated potential disorder) goes exponentially with the sample thickness but is also extremely temperature dependent [138], which is again inconsistent with our data.

We propose another model here based on the quantum mechanical wavefunction of the electrons and holes in few-layer samples. Since the few-layer samples used in our work are thin (all less than 6 *nm* in thickness) one would expect the quantum mechanical spatial coherence of the electron wavefunction to hold in the direction perpendicular to the layers even at room temperature. We assume a fast recombination time  $\tau_s$  (as given by the products of the Auger rate constants and the defect density) for the two surface layers in a few-layer sample, and a slow recombination time  $\tau_i$  for all the inner layers, and then estimate the actual recombination time for a few-layer sample by weighing the inverse lifetime with the probability of electron (or hole) occupation of each layer as given by the electron (or hole) wavefunction in a few-layer sample. This pro-

cedure is equivalent to assuming a spatially varying defect structure in a more formal calculation technique such as the one presented by Wang et al. [164]. The envelope of the electron (or hole) wavefunction of the lowest quantum confined state (confined in the direction perpendicular to the layers) can be obtained using the effective mass approximation (and assuming a discrete space),

$$\psi(x, y, k) = \phi(k) f(x, y) = \sqrt{\frac{2}{1+N}} \sin\left(\frac{\pi k}{1+N}\right) f(x, y) \quad (6.5)$$

where  $f(x, y)$  is the envelope wavefunction in the plane of a layer,  $\phi(k)$  is the envelope wavefunction in the direction perpendicular to the layers evaluated at the  $k$ -th layer, and  $N$  is the total number of layers. The lifetime  $\tau$  of the carriers in a few-layer ( $N \geq 2$ ) sample can be estimated as,

$$\frac{1}{\tau} = \frac{0.5 (|\phi(1)|^2 + |\phi(N)|^2)}{\tau_s} + \frac{1 - 0.5 (|\phi(1)|^2 + |\phi(N)|^2)}{\tau_i} \quad (6.6)$$

The results thus obtained are plotted in Figure 6.6(a) along with the data. We used values of  $\tau_s$  and  $\tau_i$  equal to 50 ps and 1.3 ns, respectively, to obtain a good fit. The excellent agreement between the model and the data for all layer numbers  $N$  shows that the model captures the essential physics. Note that we only considered the lowest quantum confined state in Eq.(6.5). There is a possibility that higher energy quantum confined states in our few-layer samples could be occupied by hot or thermally excited carriers. However, even in the 10-layer sample the second confined state is estimated to be 50-100 meV higher in energy [36] and is, therefore, not expected to have significant carrier population. Also, we see no temperature dependence in the measured lifetimes and this indicates that there is no significant error made in ignoring carrier spilling into the higher quantum confined states.

## 6.7 Defect refilling dynamics

In the previous sections, we have discussed the photoexcited electron-hole recombination dynamics in few layer MoS<sub>2</sub>, and proposed a surface-bulk recombination theory that can explain the experimentally observed carrier lifetimes from monolayer to bulk MoS<sub>2</sub>. The discussion has focused on the negative part of  $\Delta T/T$ , which represents the intraband absorption of the probe pulse due to the presence of the photoexcited carriers. In this section, the positive to negative transition of  $\Delta T/T$  immediately following the photoexcitation will be explained.

As demonstrated in Figure 6.3, the midgap  $\sigma_r$  per layer increases as the number of layers increase. This nonlinear  $\sigma_r$  dependence on sample thickness is consistent with the fact that (see Figure 6.4), the positive portion of  $\Delta T/T$  transient of the 10-layer sample is much larger than that of the 4-layer sample. In addition, the temperature dependent data in Figure 6.4 and Figure 6.3 suggest that the positive  $\Delta T/T$  signal likely comes from the photobleaching of the midgap states. The pump pulses excite the trapped charges in the midgap states to the conduction band, causing the midgap absorption of the probe pulses to decrease after the photoexcitation.

Given the above analysis, the positive to negative transition of the  $\Delta T/T$  transients represent the refilling of the midgap states by the electrons in the conduction band because the samples are N-doped. Once the photoexcited electron-hole recombination dynamics is correctly modeled, it can be subtracted away from the measured  $\Delta T/T$  to obtain the defect refilling dynamics as shown in Figure 6.7. In Figure 6.7, we have observed both carrier density and temper-

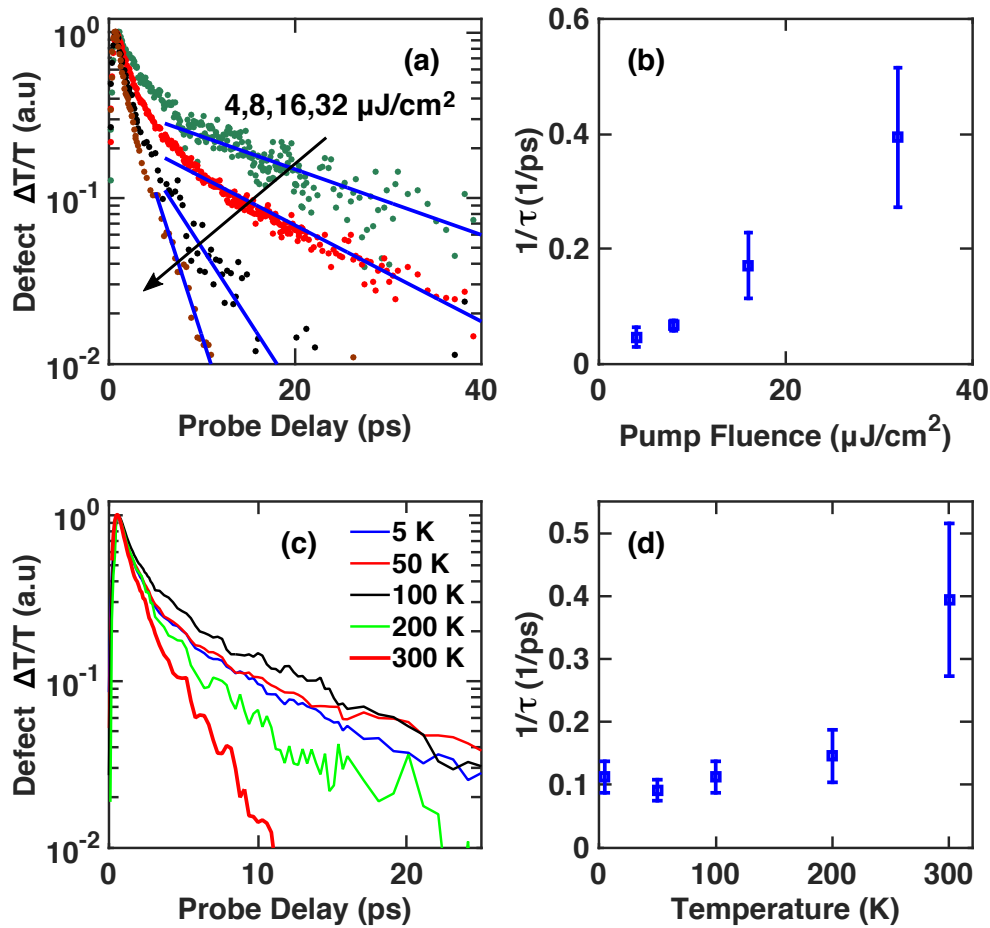


Figure 6.7: Defect refilling dynamics of a 10 layer sample. (a,b) Pump fluence dependent defect refilling dynamics at room temperature. The dynamics was obtained by extracting away the simulated free carrier dynamics. The defect refilling dynamics has a super-linear dependence on the pump fluence. (c,d) The temperature dependent defect refilling dynamics shows that, there is a thermal activation energy for defect refilling, which is  $\sim 200$  K.

ature dependent defect refilling dynamics. The temperature dependent defect refilling transients are very different from the measured temperature independent electron-hole recombination transients in Figure 6.4. This result suggests

that the midgap states refilling and carrier recombination dynamics are likely decoupled processes.

## 6.8 Conclusion

Our results for the photoexcited carrier lifetimes in few-layer MoS<sub>2</sub> suggest that carrier recombination is dominated by defect-assisted processes that have much higher rates at the surface layers than in the inner layers. The excellent agreement between the data and the model for the scaling of the carrier lifetimes with the number of layers points to the validity of treating the electron and hole states in few-layer TMDs as quantum confined states describable by envelope wavefunctions in the effective mass approximation in the same way as is done in the case of more traditional semiconductor nanostructures, such as quantum wells. The exact nature of the defects that contribute the most to carrier recombination in TMDs remains unclear. Sulfur vacancies in MoS<sub>2</sub> were considered a strong candidate in a recent theoretical work by Wang et al. [164] and, given the low formation energies of sulfur vacancies [107], surface layers are expected to have more of them than the inner layers in few-layer samples. Our work also shows that monolayer light emitting and detecting TMD devices will pay a high penalty in terms of the quantum efficiency unless suitable schemes for controlling and/or reducing surface defects are developed.

CHAPTER 7  
THz MECHANICAL OSCILLATIONS IN TRANSITION METAL  
DICHALCOGENIDES

## 7.1 Introduction

Layered 2D materials such as graphene and MoS<sub>2</sub> have promising potential for nano and micromechanical applications. The strong light-matter interaction and the 2D crystal structure make layered materials ideal candidates for membrane resonators in the *MHz* range with coupled optical, electrical and mechanical properties [8, 39, 182, 175, 81, 19]. However, the possibility of using layered TMDs as Microelectromechanical Systems (MEMS) devices in the *GHz* and *THz* ranges has not been explored yet. Compared with the traditional MEMS technology, the advantage of using layered materials as ultra-high-frequency MEMS devices is in the ease of producing high quality thin films without fabrication [157, 132, 40]. Recent Raman studies show that the rigid-layer longitudinal acoustic (LA) modes in bilayer MoS<sub>2</sub> can reach up to  $\sim 1.3$  THz [189]; these coherent oscillations of the rigid-layer LA phonons have also recently been observed in time domain [166, 48].

In this chapter, we present the study of excitation, detection and dissipation mechanisms of coherent THz mechanical oscillations in few-layer MoS<sub>2</sub>. We found that, in few-layer MoS<sub>2</sub>, the out-of-plane LA phonons (rigid-layer breathing mode) can be coherently created by Displacive Excitation due to the strong light absorption of ultrafast optical pump pulses at 2.74 eV. Excited coherent phonons were detected by using 1.37 eV probe pulses through index oscillations as the result of the mechanical motions. These mechanical oscillations

have quality factors that do not depend on substrate temperature, pump fluence, or sample thickness. However, a continuous degradation of oscillation lifetime was observed as a function of accumulated laser exposure time. Our experimental results lead us to the conclusion that the lifetime of the rigid-layer LA phonon is surface scattering limited. Our results highlight the possibility of using few-layer MoS<sub>2</sub> samples as THz MEMS devices, which could operate at THz frequencies with FQ (frequency-quality factor) products over  $\sim 1 \times 10^{13} \text{ Hz}$  at room temperature.

Because MEMS rely on the coherent mechanical motions, we will first introduce basic concepts of high frequency MEMS and then discuss the coherent THz mechanical oscillations in few layer MoS<sub>2</sub> samples.

## 7.2 Introduction to high frequency MEMS

Microelectromechanical Systems (MEMS) are devices that utilize coherent mechanical motions. The MEMS markets are worth over \$10B[63], and covers a broad range of commercial and research applications, for example: timing oscillators/frequency filters[157], gyroscopes[12], and biosensors[161]. Moreover, MEMS devices are extremely useful in studying fundamental scientific phenomena as well. For instance, macroscopic quantum states were demonstrated in MEMS devices[109]; also, MEMS devices were used to detect single spin state[129].

In all MEMS resonator/filter applications, the single most important property is the mechanical resonant frequency, also known as the harmonic frequency. The resonant frequency is determined by the geometry and material

of the MEMS device, as well as the nature of the mechanical oscillation. We will demonstrate how the aforementioned factors affect the resonant frequency by examining two commercially successful high frequency MEMS designs: surface acoustic wave (SAW) devices and bulk acoustic wave (BAW) devices, which are illustrated in Figure 7.1.

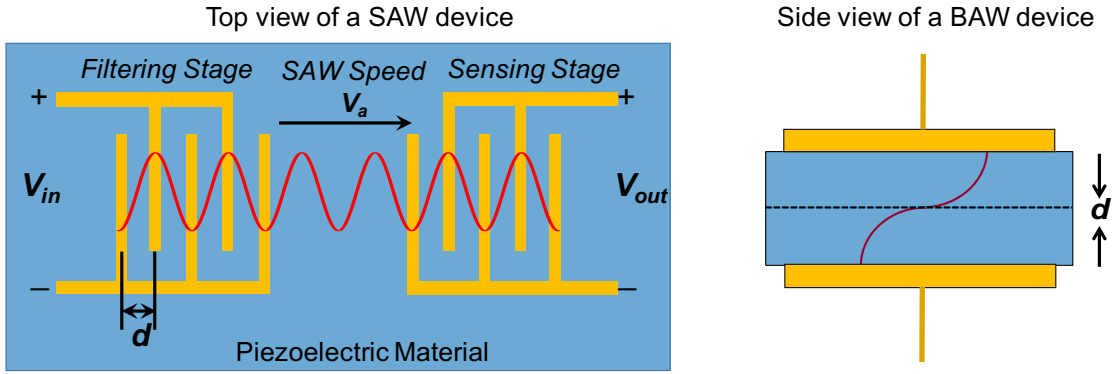


Figure 7.1: SAW and BAW devices.

The filtering stage in a SAW device (shown in Figure 7.1) is composed of alternating tensile and strain regions created by the opposite voltage polarities of adjacent electrodes through the piezoelectric effect. The filtering stage can only coherently launch surface acoustic waves with wavelength  $d$  at frequency  $V_a/2d$ , where  $V_a$  is the surface acoustic wave phase velocity and  $d$  is the pitch of the metal electrodes. Hence, other frequency components of the voltage signal  $V_{in}$  are filtered out. Unlike SAW devices, BAW devices utilize the standing wave mode instead of the propagating wave mode. The wavelength of the fundamental mode of a BAW filter is twice the thickness of the thin film. To summarize, resonant frequencies of both SAW and BAW filters and resonators can be described as:

$$f = \frac{V}{2d} \tag{7.1}$$

In SAW devices,  $V$  is the phase velocity of the surface acoustic wave and  $d$  is the metal pitch. In BAW devices,  $V$  is the longitudinal acoustic wave velocity and  $d$  is the thin film thickness. The acoustic wave velocity  $V$  is determined by both material properties and vibrational mode used in a MEMS device, while the parameter  $d$  is determined by the geometry of the device.

### 7.2.1 MEMS oscillations in the time and frequency domain

At resonant frequency, MEMS devices can support coherent mechanical (harmonic) oscillations with little energy loss. In most cases, the rate of this energy loss is linearly proportional to the energy stored in the oscillator, meaning the dynamics of the stored energy can be described by a simple ordinary differential equation:

$$\frac{dE_{osc}}{dt} = -2\tau E_{osc} \quad (7.2)$$

where  $E_{osc}$  is the stored oscillation energy and  $\tau$  is the decay time constant. The solution of the  $E_{osc}$  dynamics is a simple exponential decay:  $E_{osc} = E_o \exp(-2t/\tau)$ . For a harmonic oscillator, the energy stored is linearly proportional to the square of the peak oscillation amplitude  $A_o$ , hence the dynamics of the harmonic oscillation  $A_{osc}(t)$  can be described as:

$$A_{osc}(t) = A_o e^{-t/\tau} \times \sin(\omega_o t) \times \mu(t) \quad (7.3)$$

where we have assumed a *sine* phase oscillation, and  $\mu(t)$  is the Heaviside step function. If we perform a Fourier transform on  $A_{osc}(t)$ , we have the oscillation amplitude function in the frequency domain:

$$A_{osc}(\omega) = \frac{A_o \tau}{\sqrt{2\pi}} \times \frac{\omega_o \tau}{\omega_o^2 \tau^2 + (1 - i\omega\tau)^2} \quad (7.4)$$

Note that the definition of the Fourier transform is  $\frac{1}{\sqrt{2\pi}} \int A_{osc}(t)e^{i\omega t} dt$ . In Figure 7.2, the real part, imaginary part, and the magnitude of  $A_{osc}(\omega)$  are plotted with  $A_o = 1$ ,  $\omega_o = 50 \text{ rad/s}$  and  $\tau = 1 \text{ s}$ . It is very clear that the real part of  $A_{osc}$  has a

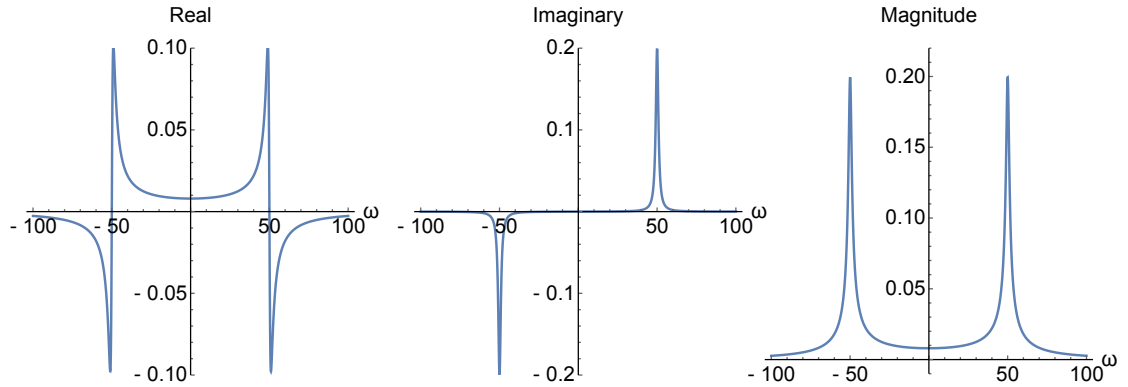


Figure 7.2: Real, imaginary and magnitude of  $A_{osc}(\omega)$

zero crossing at  $\omega_o$ , while both the imaginary part and the magnitude of  $A_{osc}$  are centered at  $\omega_o$ . This is an important conclusion: **due to the exponential decay  $A_o \exp(-t/\tau)$ , the magnitude of  $A_{osc}(\omega)$  has a Lorentzian shape**, and the center of the Lorentzian is determined by the resonant frequency of the oscillator.

## 7.2.2 Quality factor

It is also worthwhile to discuss the definition of the quality factor  $Q$  of a mechanical resonator based on the previous simple time and frequency domain analysis (Chapter 7.2.1). The definition of  $Q$  is :

$$Q = 2\pi \times \frac{\text{Energy stored}}{\text{Energy loss per cycle}} \quad (7.5)$$

Using this definition, the quality factor represents the number of oscillation cycles that an oscillator can have without an external driving force. However,

because the "energy stored" in an oscillator continuously changes due to dissipation, we cannot use this definition directly. Instead, after one period, the exponential decay  $E_{osc} = E_o \exp(-2T/\tau)$  can be linearized as  $E_{osc} \approx E_o(1 - 2T/\tau)$ :

$$Q \approx \frac{2\pi \times E_o}{E_o - E_o(1 - 2T/\tau)} = \frac{2\pi}{4\pi/\omega_o/\tau} = \frac{1}{2}\omega_o\tau \quad (7.6)$$

Or, the definition of Q can be written in a more explicit way:

$$Q = \frac{2\pi \times \text{Energy stored at } t = 0}{\text{Oscillation period} \times \text{Energy loss rate at } t = 0} = \frac{2\pi}{T \times 2/\tau} = \frac{1}{2}\omega_o\tau \quad (7.7)$$

Given that  $\omega_o = 50 \text{ rad/s}$  and  $\tau = 1 \text{ s}$ ,  $Q = 25$  according to Eq. 7.6 and 7.7.

The second definition of Q is given in frequency domain:

$$Q = \frac{\omega_o}{\Delta\omega} \quad (7.8)$$

where  $\Delta\omega$  is the half power width of the resonant peak in the frequency spectrum. Although we can solve Eq. 7.4 to show that the definition above also gives  $Q = 1/2 \times \omega_o\tau$ , it is easier to plot the square of Eq. 7.4 directly to demonstrate that the two definitions are equivalent.

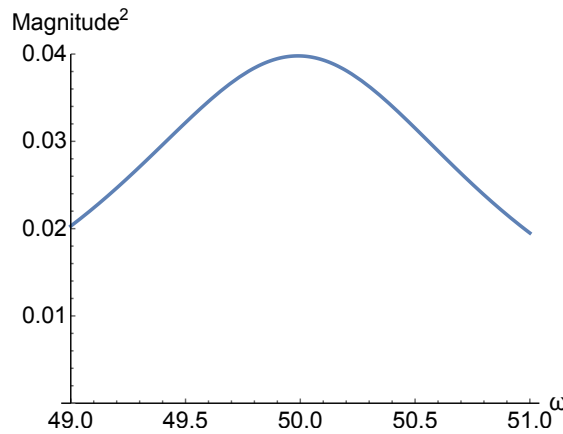


Figure 7.3: Definition of Q in frequency domain.  $Q = \omega_o/\Delta\omega = 1/2 \times \omega_o\tau$

Although the analysis of  $Q$  and  $A_{osc}(\omega)$  can be derived formally from the harmonic oscillator ODE, the links between the exponential decay in the time

domain, the Lorentzian power spectrum, and the different definitions of quality factor  $Q$  are rarely emphasized.

### 7.2.3 BAW MEMS filters and resonators

For consumer and industrial applications, Bulk Acoustic Wave (BAW) MEMS are gaining popularity in high frequency applications[131]. For instance, there are 22 BAW RF front-end filters used in the 2015 Iphone [63]. In fact, BAW devices are so important that the Institute of Electrical and Electronics Engineers(IEEE) uses the structure of a BAW resonator as the circuit symbol for all crystal resonators and filters.

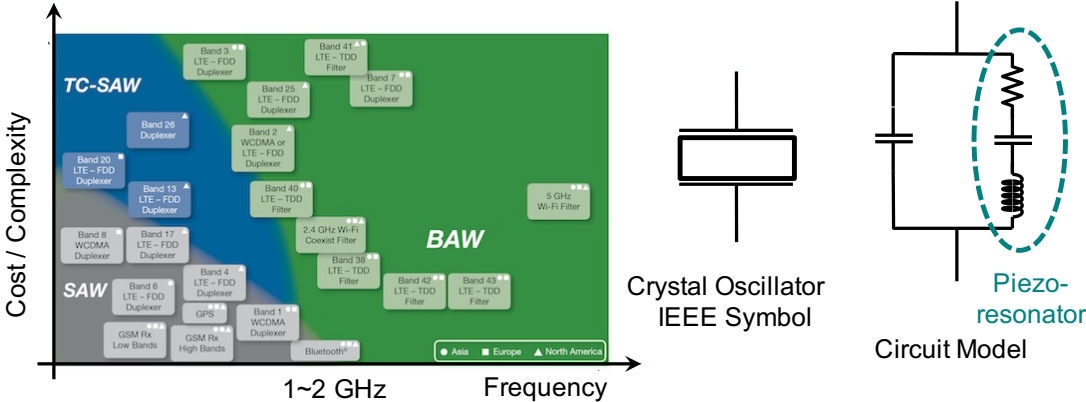


Figure 7.4: BAW MEMS dominate the market of high frequency RF applications. BAW resonator, as illustrated in Figure 7.1, are used as the IEEE symbol for all crystal oscillators.

According to Eq. 7.1, there are two ways to produce high frequency BAW MEMS: reducing the thickness of the thin film sandwiched between the two metal contacts, or by choosing piezoelectric materials with a higher longitudi-

nal acoustic phonon velocity. However, there are two challenges in building high frequency BAW devices as well: the first challenge is to manufacture ultra-thin films. For instance, a 50 GHz BAW device needs 50 nm thick thin film if the material has a sound velocity of 5 Km/s. The second challenge is that the parasitic capacitance scales inversely as a function of thin film thickness, as shown in the circuit model in Figure 7.4. At extremely high frequencies, the parasitic capacitance will short the peizo-resonator part of the BAW MEMS completely.

Because the parasitic capacitance relates to the electronic design of the MEMS devices, which is a topic beyond the scope of this chapter, we will only focus on how to produce ultra-thin films that support extremely high frequency mechanical oscillations in the 100 GHz to 1 THz range with good quality factors.

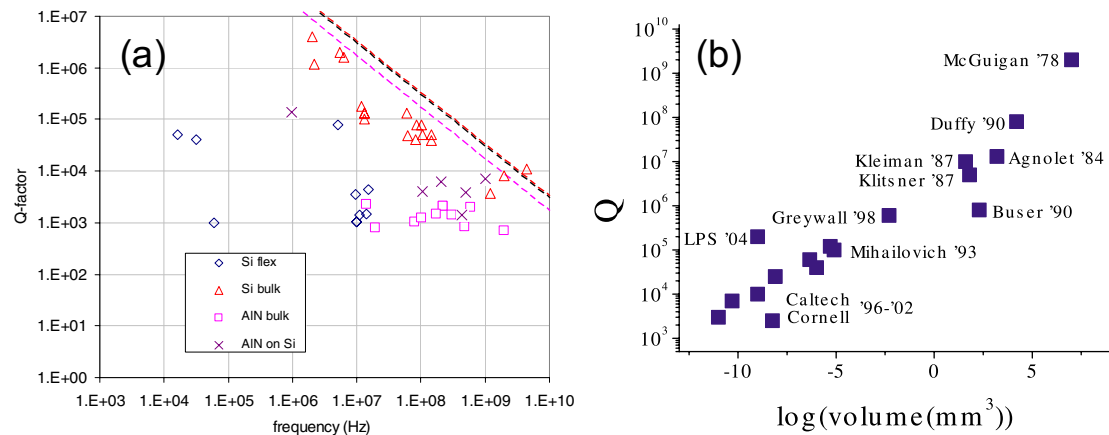


Figure 7.5: High frequency MEMS challenges. (a) It is very difficult to fabricate MEMS devices operating beyond 10 GHz with a good frequency-quality factor product (FQ)[157]. The dashed lines are theoretical maximum FQ products of AlN, Si and Quartz ( $1 \sim 2 \times 10^{13} Hz$ ). (b) Quality factor Q drops rapidly as the MEMS devices shrink in size.[132]

As shown in Figure 7.5(a), it is relatively common for research groups to

produce MEMS devices with frequency-quality factor products (FQ) close to the theoretical maximum FQ of bulk MEMS materials below 100 MHz. The theoretical FQ products of AlN, Si, and Quartz are  $1 \sim 2 \times 10^{13}$  Hz, and are plotted as the dashed lines in Figure 7.5(a). Beyond 100 MHz, MEMS devices suffer from losses due to imperfections in the MEMS fabrication processes in addition to the intrinsic material losses [132]. As shown in Figure 7.5(b), the quality factor drops rapidly as the MEMS device shrinks in size for high frequency applications.

Next, we will show that, layered metal dichalcogenides thin films are potential candidates for building extremely high frequency BAW MEMS beyond 100 GHz as they do not suffer from these fabrication related challenges.

## 7.2.4 Coherent acoustic oscillations in MEMS

For BAW devices, the BAW resonant frequency  $f$  and the thin film thickness  $d$  are related by the sound velocity:  $f = V/2d$ . This sound velocity is also referred to as the acoustic phonon velocity. Acoustic phonons are very different from optical phonons: (1) Since adjacent atoms/layers move in the same direction for acoustic motion, a sudden change in position of one atom/layer can activate the vibration of the adjacent atoms/layers. This is the reason why acoustic vibrations can propagate as waves. Unlike acoustic vibrations, propagating waves of optical vibrations cannot be easily launched and optical phonons have zero velocity in the first-order approximation. (2) Because adjacent atoms/layers move in the same direction for acoustic motion, the acoustic vibrations have long range order. For example, at resonant frequency, a standing wave vibration forms across the BAW thin film as shown in Figure 7.1. In other words,

coherent acoustic phonon oscillations are macroscopic vibrations. Conversely, because adjacent atoms move in the opposite direction, optical phonon vibrations manifest themselves as microscopic vibrations.

Since ultra-high frequency BAW devices need extremely thin MEMS films, it is natural to use layered materials such as graphite or transition metal dichalcogenides (TMDs), which can have thickness down to  $\sim 1 \text{ nm}$  (bi-layer structure), while avoiding the challenges associated with the fabrication of such thin films.

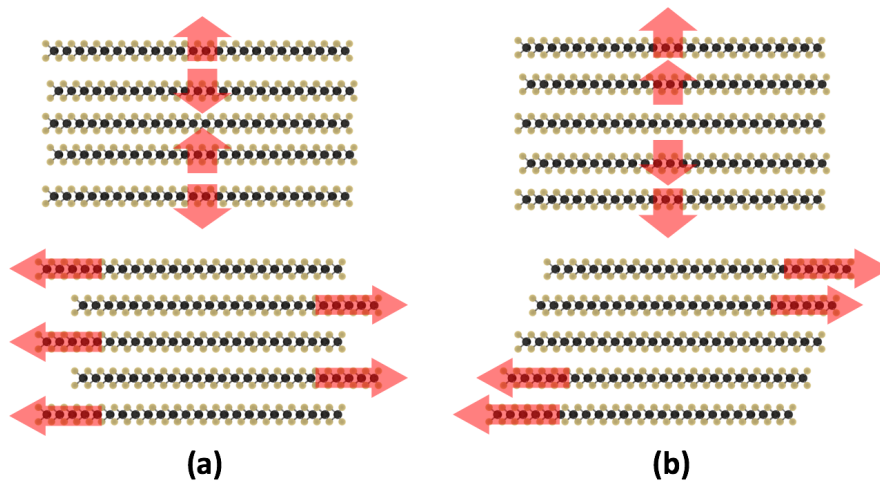


Figure 7.6: Rigid layer motions of few-layer MoS<sub>2</sub>. (a) Coherent optical phonon oscillations: adjacent layers move in opposite directions. (b) Coherent acoustic phonon oscillations: adjacent layers move in the same direction.

In few layer TMDs, such as MoS<sub>2</sub>, we are interested in rigid layer motions, which have both optical and acoustic modes. Optical phonon vibrations require adjacent layers to be moving in the opposite directions, while acoustic phonon vibrations require adjacent layers to be moving in the same direction. In addition, rigid layer motions can be categorized into breathing modes (out-of-plane motions) and shearing modes (in-plane motions). Breathing and shearing modes of coherent rigid layer optical and acoustic vibrations are illustrated in

Figure 7.6(a).

### 7.3 Ultra-high frequency coherent phonon oscillations

The dynamics of ultra-high frequency coherent phonon oscillations have been studied extensively in the past few decades. Several examples of experimental work [24, 80, 25, 179, 101, 144] on coherent phonon oscillations are given in Figure 7.7. There are several interesting observations to be made from these experimental results. Firstly, both coherent optical and acoustic phonon oscillations can be excited. Secondly, whereas coherent optical phonon oscillations can be excited and observed in bulk materials, coherent acoustic phonon oscillations can only be excited if the wavelength of the excited acoustic phonon is well defined. For example, in the work done by Sun[144], the acoustic oscillation wavelength is determined by the InGaN/GaN quantum well structure of thickness  $\sim 1$  nm. Lastly, because the coherent THz phonon oscillations are too fast to be excited and detected electronically, time-resolved ultrafast optical pump optical probe techniques were applied in all the experimental work in Figure 7.7.

So why can't coherent acoustic phonon oscillations be easily excited in bulk materials? The answer lies within the wave-propagation properties of the acoustic phonons. Like photons, the energy of an acoustic phonon is linearly proportional to its momentum:  $E = \hbar k \times V$ . The slope of the linear energy-momentum dispersion is the sound speed of this particular acoustic phonon branch in the First Brillouin Zone. In bulk materials, if there is no mechanical or optical structure to define the desired acoustic phonon wavelength, acoustic

phonons of different wavelengths will be excited at the same time and travel at the same speed, thus no coherent oscillation can be detected. Conversely, the

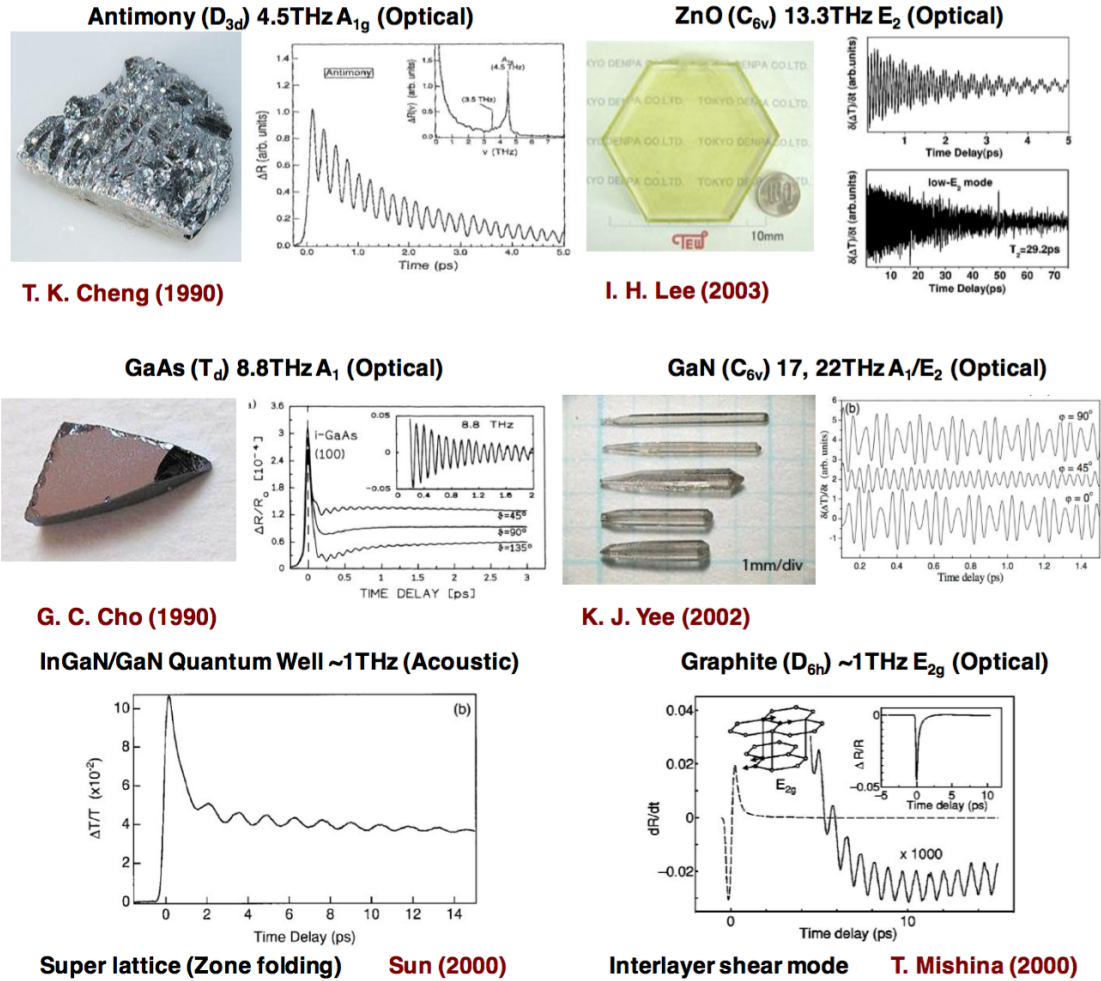


Figure 7.7: Several examples of reported coherent phonon oscillations[24, 80, 25, 179, 101, 144]. Whereas coherent optical phonon oscillations can be excited and observed in bulk materials, coherent acoustic phonon oscillations can only be excited if the wavelength of the excited acoustic phonon is well defined. For example, the acoustic oscillation wavelength is determined by the InGaN/GaN quantum well structure [144].

energy of optical phonon does not depend on its momentum in the first order approximation (Einstein Model). After the impulse excitation, optical phonons

with slightly different momentum oscillate at the same frequency with the same phase (excitation of an optical phonon mode), and slowly propagate (zero velocity in the Einstein Model) in different directions. Hence, coherent optical phonon oscillations can be excited and detected in bulk materials.

## 7.4 Ultrafast optical excitation of coherent phonons

As discussed in the last section, ultra-high frequency coherent phonon oscillations can be studied by ultrafast Optical Pump Optical Probe (OPOP) techniques. In this section, we will conduct a literature survey on different coherent phonon generation processes in OPOP experiments.

### 7.4.1 Optical interference grating

The first demonstrations of optical pulse induced coherent acoustic phonon oscillations were reported by Fayer *et al.*[130, 104, 105]. In these experiments, two excitation optical pulses ( $\sim 100$  ps pulse width) coincided on the samples. The two excitation pulses overlap and interfere with each other, creating alternating constructive and destructive optical intensity peaks or nulls. In materials that absorb the excitation pulses, the alternating optical interference pattern creates excited electron-hole density peaks and nulls, thus coherent acoustic phonons whose wavelengths that match the interference pattern geometry can be launched through electron-phonon interactions or a nonequilibrium distribution of heat. In non-absorbing materials, the optical interference pattern can create coherent acoustic phonons through stimulated Brillouin scattering[114].

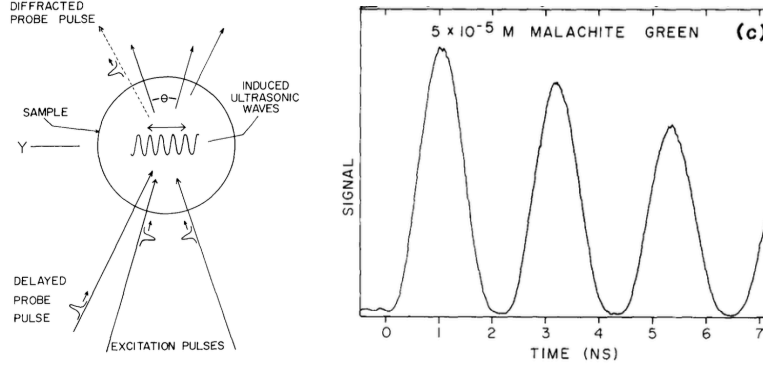


Figure 7.8: The first demonstrations of optical pulse induced coherent acoustic phonon oscillations. Data was reported by Fayer *et al.*[130, 104, 105].

In Brillouin scattering, the acoustic phonons can be generated or absorbed by the incident optical light. The periodic acoustic wave works as a periodic grating that scatters light according to Bragg's law. It is straightforward to derive the acoustic phonon frequency generated in Brillouin scattering. Assume that the incident light has momentum  $\vec{k}_i$ , frequency  $\omega_i$ , and optical index at  $\omega_i$  is  $n_i$ ; the scattered light has momentum  $\vec{k}_s$ , frequency  $\omega_s$ , and optical index  $n_s$ . The phonon emitted by Brillouin scattering has momentum  $\vec{q}$  and frequency  $\omega_q$ . According to momentum and energy conservation, we have:

$$\omega_s = \omega_i - \omega_q \quad (7.9)$$

$$\vec{q} = \vec{k}_i - \vec{k}_s \quad (7.10)$$

$$|\vec{k}_{i,s}| = n_{i,s}\omega_{i,s}/c \quad (7.11)$$

$$|\vec{q}| = \omega_q/V_q \quad (7.12)$$

If  $\theta$  is the angle between the incident and scattered light:

$$q^2 = k_i^2 + k_s^2 - 2|k_i k_s| \cos(\theta) \quad (7.13)$$

Plugging in the light/phonon energy-momentum dispersion relations yields:

$$\omega_q^2 = \frac{v_q^2 \omega_i^2}{c^2} \left[ n_i^2 + n_s^2 \frac{\omega_s^2}{\omega_i^2} - 2n_i n_s \frac{\omega_s}{\omega_i} + 4n_i n_s \frac{\omega_s}{\omega_i} \sin^2(\theta/2) \right] \quad (7.14)$$

Because the acoustic phonon frequency is at least two-orders magnitude smaller than the frequency of the incident photons, we can safely assume that  $\omega_s/\omega_i$  is approximately 1.

$$\omega_q = \frac{v_q \omega_i}{c} \sqrt{(n_i - n_s)^2 + 4n_i n_s \sin^2(\theta/2)} \quad (7.15)$$

In most cases, optical index is a slow varying function, and  $n_s$  is very close to  $n_i$ :

$$\omega_q = 2 \frac{v_q}{c} \omega_i n_i \times \sin(\theta/2) \quad (7.16)$$

## 7.4.2 Nanostructured grating

Instead of using the optical interference of two pulses to define the wavelength of acoustic oscillations, nanostructured gratings set the acoustic wavelength by their physical geometries as shown in Figure 7.9. In Liu's work [87], when the

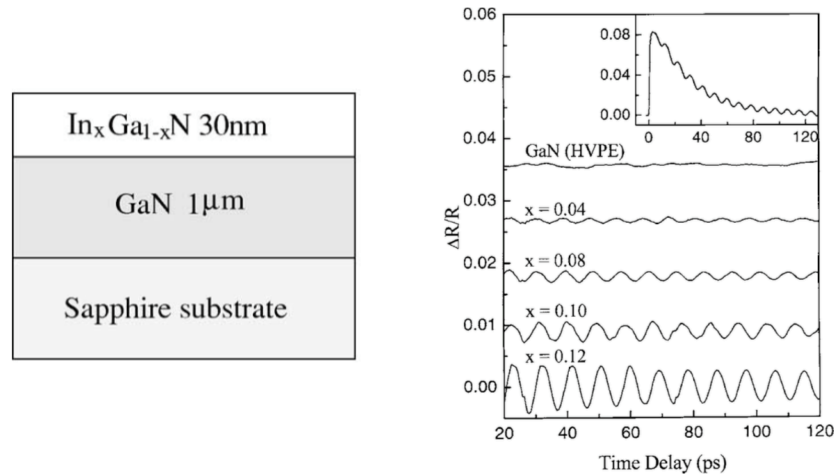


Figure 7.9: Coherent acoustic phonon oscillations can be excited by applying ultrafast optical pulses on nanostructure gratings[144, 87].

indium content  $x$  of the 30 nm thick  $In_xGa_{1-x}N$  layer is zero, coherent acoustic oscillations cannot be excited. By increasing the indium content from zero to 0.12, the absorption contrast between  $In_xGa_{1-x}N$  and  $GaN$  launches acoustic waves with a wavelength of twice the thickness of the  $In_xGa_{1-x}N$ . In addition, by increasing the indium content, the amplitude of the coherent acoustic phonon oscillations can be enhanced, as shown in Figure 7.9. Because the oscillation frequency is determined only by the acoustic velocity and the thickness of the  $In_xGa_{1-x}N$  layer in the first order approximation, the oscillation frequency only weakly depends on the indium content  $x$ .

### 7.4.3 Stress/heat pulses

Thomsen *et al.* demonstrated that acoustic phonon pulses can be created by an intense optical pulse through either stress or heat [152]. In Thomsen's work, the

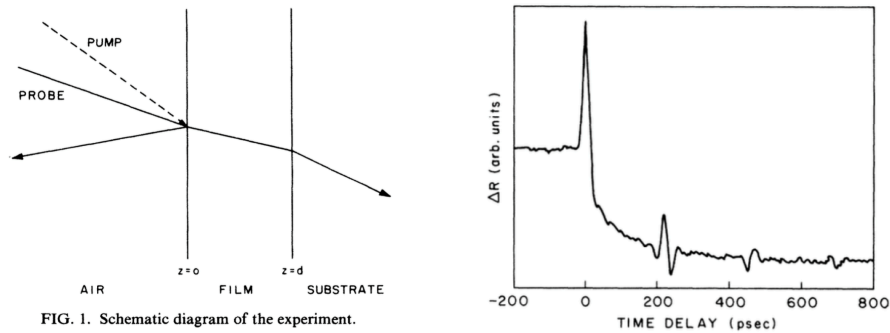


Figure 7.10: Acoustic pulse can be created by surface heat/stress pulse[152]. The acoustic echos (reflected acoustic pulses) were be observed in the transient reflection data.

acoustic pulses bounce back and forth between the two surfaces of an  $As_2Te_3$  thin film, and are observed by the reflected optical probe pulse through the change in refractive index.

## 7.4.4 Surface space-charge field

As discussed in the previous sections, without well a defined optical/structural grating geometry, coherent acoustic phonon oscillations cannot be generated efficiently. This is the reason why most reported coherent phonon oscillations in bulk materials are optical phonon oscillations. There are multiple mechanisms

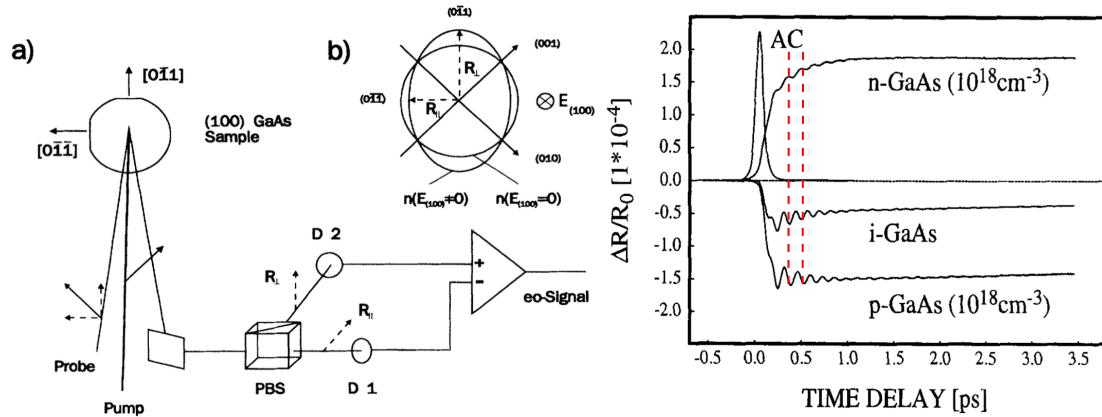


Figure 7.11: Coherent optical phonons created by a surface space-charge field. Coherent longitudinal optical phonon oscillations of *GaAs* can be excited by applying ultrafast optical pulses [25, 75, 33]. Note that the oscillation phases differ by  $180^\circ$  between the N-doped sample and P-doped *GaAs* samples.

that can create coherent optical phonons, including charge transport in the surface space-charge fields, coherent Raman scattering, and displacive excitation. We will discuss the latter two mechanisms in detail later.

In Figure 7.11, optical pump and probe pulses are sent to a [100] *GaAs* substrate. When the optical pump pulse excites the substrate, the photogenerated electron-hole pairs create a surface-charge current, which becomes the impulsive driving force of the coherent longitudinal optical (LO) phonon oscillations. The reflected probe pulse is separated into its orthogonal components  $R_{\perp}$  and

$R_{\parallel}$  as defined in Figure 7.11.  $R_{\perp} - R_{\parallel}$  contains the information of the refractive index difference  $n_{\perp} - n_{\parallel}$ , according to the electro-optic effect:

$$n_{\perp} - n_{\parallel} = n_o^3 r_{41} E_z \quad (7.17)$$

where  $n_o$  is the unperturbed refractive index,  $r_{41}$  is the electro-optic coefficient of *GaAs*, and  $E_z$  is the longitudinal surface field. Photoexcited electron-hole pairs give rise to displacement and drift currents in the  $E_z$  direction, and this current causes an impulsive change to  $E_z$ , meaning its spectrum contains the LO phonon frequency.

In Figure 7.11, the  $\sim 8.8$  THz coherent oscillation in  $R_{\perp} - R_{\parallel}$  matches the longitudinal optical (LO) phonon frequency of *GaAs*. At the surface, the band bending of *n - GaAs* and *p - GaAs* point in opposite directions, causing their surface electric fields to have opposite directions as well. This explains the sign change between samples in Figure 7.11. The intrinsic sample was determined to have a background p-doping [75, 33].

## 7.4.5 Displacive excitation and Raman scattering

Coherent acoustic and optical phonons can be excited by displacive excitation (DE) and Raman scattering (RS) as well[184]. DE and RS processes are discussed together as the two are not trivial to distinguish experimentally[84, 29, 141]. In order to identify the exact excitation mechanism, we need to extract several parameters/dependencies from the measured ultrafast transients: (1) the oscillation phase with respect to the zero time delay between the pump and probe pulses; (2) the frequency of the oscillation; (3) the oscillation amplitude and its dependence on the optical pump fluence; (4) the mode and the symmetry of the

photoexcited coherent phonons; (5) the lifetimes of the photoexcited coherent phonons and electron-hole pairs.

In this section, we will use a simple phenomenological description of coherent phonon oscillations to explain the mechanisms of displacive excitation and Raman scattering. The excitation and relaxation of coherent phonons can be phenomenologically described by a second order differential equation:

$$\frac{d^2 Q}{dt^2} + \frac{2}{\tau} \frac{dQ}{dt} + \omega^2 Q = F(t) \quad (7.18)$$

where  $Q$  is the coherent phonon oscillation amplitude,  $\tau$  is the coherent phonon lifetime,  $\omega$  is the frequency, and  $F(t)$  is the driving force initiating the coherent phonon oscillations. This driving force creates coherent phonons through either displacive excitation or coherent Raman scattering. Mathematically, there are two possible types of the driving forces: (1)  $F(t)$  is a delta function:  $F(t) = \delta(t)$ . An impulsive excitation of coherent phonons resembles the ultrafast optical excitation pulse. The duration of the ultrafast optical pulse needs to be much shorter than the phonon oscillation period. (2)  $F(t)$  is a step function:  $F(t) = \mu(t)$ . If the ultrafast optical pulse excites the sample from its ground state into an excited state, and remains in that excited state for a time much longer than the coherent phonon oscillation period, the driving force  $F(t)$  behaves like a step function. However, if the lifetime of the excited state is much shorter than the coherent phonon oscillation lifetime,  $F(t)$  is still impulsive. **Hence, the mathematical form of  $F(t)$  alone cannot tell the physical origin of the coherent phonon oscillation.** To determine the excitation mechanism, all of the aforementioned parameters/dependencies extracted from the ultrafast transients need to be considered.

To simplify our discussion, we can assume that the lifetimes of the coherent

phonon oscillations are very long:

$$\frac{d^2Q}{dt^2} + \omega^2 Q = F_o \mu(t) \quad \textit{Step like} \quad (7.19)$$

$$\frac{d^2Q}{dt^2} + \omega^2 Q = F_o \delta(t) \quad \textit{Impulsive} \quad (7.20)$$

And the solutions of  $Q(t)$  are:

$$Q(t) = F_o \frac{1 - \cos(\omega t)}{\omega^2} \mu(t) \quad \textit{Step like} \quad (7.21)$$

$$Q(t) = F_o \frac{\sin(\omega t)}{\omega} \mu(t) \quad \textit{Impulsive} \quad (7.22)$$

Because the coherent oscillation phase can be easily determined from the measured transient data, it is very easy to tell if the driving force  $F(t)$  is impulsive or step-like.

In addition, if the material is transparent to the optical pump pulse, the excitation mechanism must be impulsive as there is no direct light absorption to excite the sample into a long-lived excited state. When there is no optical grating, as described in the previous sections, the excitation mechanism in a transparent material is mostly likely the spontaneous Raman scattering, and the coherent phonon oscillations will have a *sine* form[84].

In materials that absorb the excitation laser pulse, both *cosine* [184] and *sine* phase [29] coherent phonon oscillations have been reported. The *cosine* phase originates from the step-like driving force of the coherent phonon oscillations. The physical origin of the step-like driving force is the material's ability to remain in the photoexcited state for much longer time than the phonon oscillation period. This photoexcited state can manifest itself as an electronic state in which photoexcited electron-hole pairs slowly recombine over time, or a thermal state that hot carriers slowly relax back to the equilibrium temperature [184]. Hence,

both resonant Raman scattering—which is driven by electron-phonon scattering, and displacive excitation—which relies on the quick potential energy build-up during laser excitation, will have the same *cosine* phase. There have been several theoretical attempts to unify the displacive excitation and the resonant Raman scattering processes [141, 29]. Furthermore, when the photoexcited state has a lifetime that is much shorter than the coherent phonon oscillation period, the driving force behaves more like  $\delta(t)$  than  $\mu(t)$ , leading to coherent oscillations with a *sine* phase. If the lifetime of the excited state can be adjusted such that  $F(t)$  can be smoothly tuned between  $\delta(t)$  and  $\mu(t)$ , the coherent phonon oscillation phase can even be continuously adjusted from *sine* to *cosine* [29].

In addition to the phase, we can also look at the symmetry of the excited coherent phonon oscillations. According to the definition of the displacive excitation given by Dresselhaus *et al.* [184], only the breathing mode phonons ( $A_1$  totally symmetric mode) can be excited. Thus, when only the  $A_1$  symmetry phonon oscillations are observed, and other Raman active phonon modes are not present, we can conclude that the excitation mechanism is displacive as long as the material absorbs the excitation light. The *cosine* phase requirement of the displacive excitation can be relaxed if the excited electronic state has a shorter lifetime than the phonon oscillation period [29].

Another way to distinguish Raman scattering from displacive excitation is to look at the phonon oscillation amplitude [29]. Because light absorption is mostly linear as a function of laser pulse fluence, both the resonant Raman scattering and displacive excitation scale linearly with laser pulse fluence. However, the stimulated virtual Raman transitions depend on the square of the laser pulse fluence. If the phonon oscillation amplitude has a super-linear pump fluence de-

pendence, and the phase shifts from *cosine* towards *sine* at higher fluence, stimulated Raman scattering through virtual states might contribute significantly in the observed coherent phonon oscillations.

## 7.5 THz coherent mechanical oscillations in few-layer MoS<sub>2</sub>

Few-layer MoS<sub>2</sub> samples were mechanically exfoliated from a bulk MoS<sub>2</sub> crystal (2D Semiconductors) and transferred onto quartz substrates. The thickness of the samples were measured by AFM [94]. In this nondegenerate ultrafast Optical Pump Optical Probe (OPOP) experiment, ~80 fs pulses at 905 nm wavelength (1.37 eV photon energy) were frequency doubled to 452 nm (2.74 eV) by a beta-BaB<sub>2</sub>O<sub>4</sub> crystal, and then were chopped at 1.73 KHz. The 2.74 eV pump pulses were used to excite electrons from the valence band into the conduction band, while at the same time exciting the coherent out-of-plane(OOP) rigid-layer LA phonons. The differential transmittance ( $\Delta T/T$ ) of the time delayed 1.37 eV probe pulses were measured. A positive  $\Delta T/T$  signal results from a reduced probe absorption due to the pump excitation, while a negative  $\Delta T/T$  signal indicates that the probe absorption is enhanced following the pump excitation. A 20X objective was used to focus the pump and probe beams onto the samples. The OPOP experiment is illustrated in Figure 7.12(a).

The carrier dynamics of monolayer, few layer and bulk MoS<sub>2</sub> are discussed in Chapter 4, 5, 6 and our previous publications [168, 164, 162, 142, 167]. The focus in this chapter is the coherent oscillations we have observed. To study the dissipation mechanisms of the coherent oscillations, temperature, fluence, and sample thickness dependent experiments were performed. To study the exci-

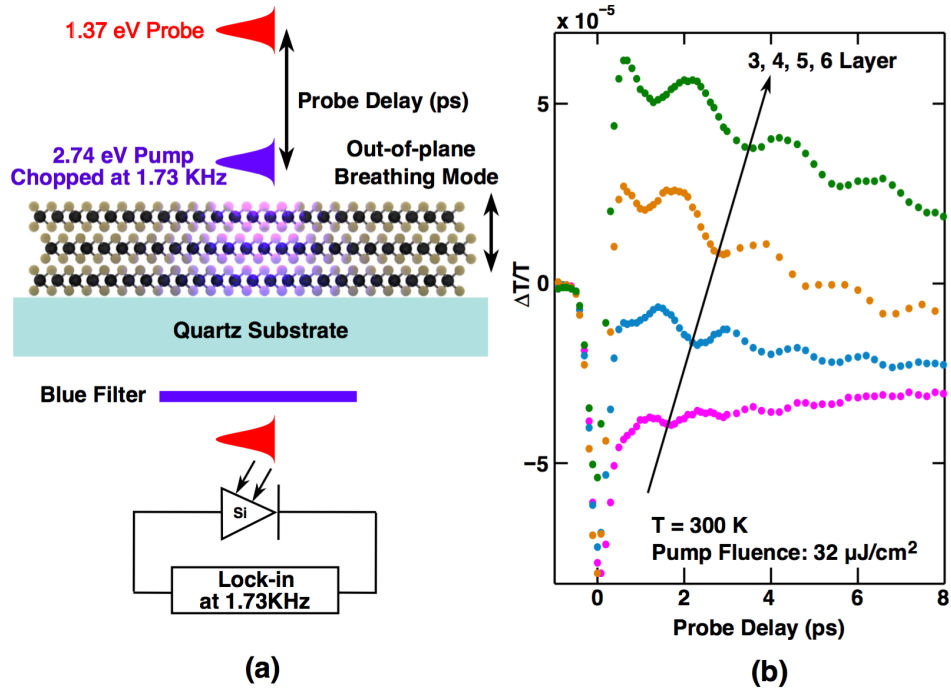


Figure 7.12: Experimental set-up and measured coherent oscillation transients. (a) Nondegenerate ultrafast OPOP experimental set-up. (b) Coherent oscillations are observed along with the ultrafast defect and carrier dynamics, which were discussed in Chapter 4, 5, 6 and by the authors [168, 164, 162, 142, 167].

tation and detection mechanisms, the OPOP experiments were also performed with 790 nm probe (1.57 eV) and 395 nm pump (3.14 eV) pulses.

$\Delta T/T$  transients of few-layer  $\text{MoS}_2$  are shown in Figure 7.12(b), and coherent oscillations were observed in all exfoliated samples other than monolayer and bilayer ones. The small coherent oscillation signals were modulated onto the defect and carrier dynamic transients, which were discussed in Chapter 4, 5 and 6. In this chapter, we focus on the coherent oscillations observed in  $\Delta T/T$  transients. Because the oscillation periods are very short compared to the slow varying defect and carrier dynamics transients as shown in Figure 7.12(b), one can use a polynomial fit for the background defect and carrier dynamics, and

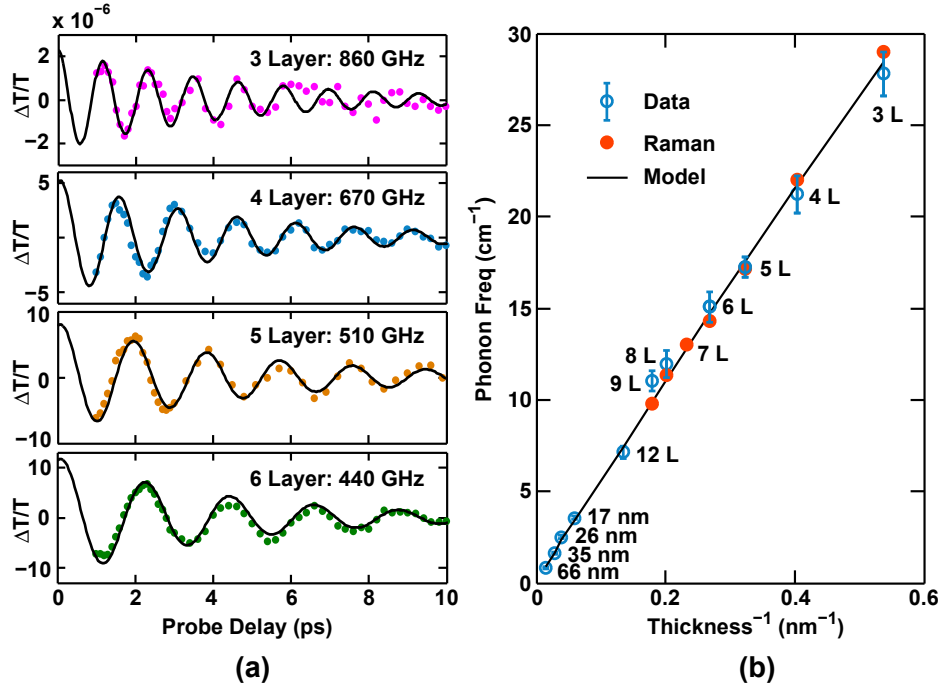


Figure 7.13: Extracted frequency-thickness dispersion of the measured coherent oscillations. (a) Frequencies, lifetimes and phases of the coherent oscillations are obtained by subtracting the background defect and carrier dynamics. The extracted transient data (dots) can be fit by  $\cos(\omega t)\exp(-t/\tau)$  (curves) very well. (d) The frequency dispersion of the coherently excited oscillations (circles with error bars) matches the Raman data (red dots) and 1D chain model (line) of out-of-plane rigid layer breathing mode in few layer MoS<sub>2</sub> very well [189]. Error bars represents the upper and lower bounds of extracted frequency for each measurement.

extract the oscillation portion of the  $\Delta T/T$  transients. In Figure 7.13(a), the coherent oscillation  $\Delta T/T$  transients of 3, 4, 5 and 6 layer samples are plotted. There are several important observations: i) the oscillation frequency of the tri-layer sample is  $\sim 860$  GHz and the frequency decreases as the number of layer increases; ii) the amplitudes of the oscillations decay exponentially as a function of the probe delay; iii) the oscillation  $\Delta T/T$  transients have  $\cos(\omega t)$  phase and start at their maximum amplitudes. Note that the oscillation transients are

extrapolated between 0 ps and  $\sim 1$  ps probe delay due to the large two photon absorption signal at zero probe delay [168, 167]. These observations are important for us to determine the nature of the measured oscillations, the excitation and dissipation mechanisms of these oscillations.

In Figure 7.13(b), the frequency dispersion of the measured coherent oscillations as a function of inverse layer thickness is plotted. The dispersion curve matches the reported OOP rigid-layer breathing mode ( $A_1$  mode) Raman data by Zhao *et al.* very well, and can be fit by the 1D chain model [189]. Directly from Figure 7.13(b), the OOP LA phonon sound velocity in bulk  $\text{MoS}_2$  is measured to be  $\sim 3.4 \pm 0.1$  km/s by  $v = \omega/q$ . These coherent oscillations are standing wave vibrations in the OOP direction due to the finite thicknesses of the few layer  $\text{MoS}_2$  samples. In the fundamental mode, the wavelength of the vibration is twice the sample thickness. In addition, the breathing mode does not break the crystal symmetry as depicted in Figure 7.14.

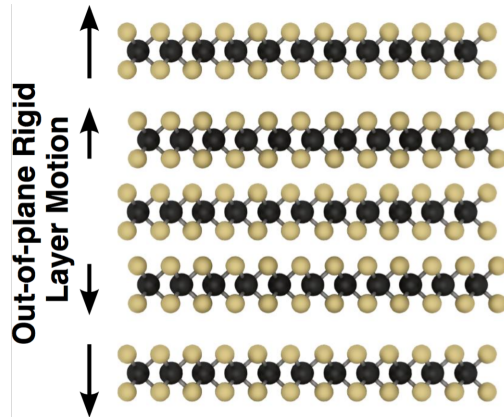


Figure 7.14: Out-of-plane (OOP) rigid layer breathing mode. The arrows depict the oscillation amplitude and direction of each layer in a 5-layer  $\text{MoS}_2$  (fundamental mode).

Unlike the reported Raman study [189], only the OOP LA rigid layer breathing mode was observed in our time-resolved ultrafast experiments as in Figure

7.12(b) and Figure 7.13(a,b). Other rigid layer motions, including all shearing modes and optical breathing modes were not detected in our OPOP experiments. OOP mechanical oscillations in trilayer samples were barely observable, and their presents in bilayer MoS<sub>2</sub> samples were not confirmed due to our limited signal-to-noise ratio.

## 7.6 Displacive excitation of the coherent THz mechanical oscillations

Coherent excitation/detection of optical and acoustic phonons by ultrafast optical pulses is a well established technique, and has been used to investigate many different material systems, include: semiconductors, oxides, super-lattices and quantum dots [130, 25, 178, 99, 87, 74]. Understanding the underlying excitation mechanism is particularly important for coherent acoustic oscillations as they are suitable for MEMS applications.

In all of the tested few-layer MoS<sub>2</sub> samples, because the pump pulse wavelength (452 nm) was much longer than the sample thickness (~2 nm in 3-layer to ~65 nm in 100-layer), the coherent oscillations were not created by absorption grating or a thermal shockwave. Therefore, the possible excitation mechanisms are Raman scattering (RS) or displacive excitation (DE). In addition, the  $\Delta T/T$  transients of the coherent phonon oscillations always start with their maximum amplitude, as shown in Figure 7.13(a), Figure 7.15 and Figure 7.16. Furthermore, the OOP rigid layer vibrations belong to the  $A_1$  symmetry group [189], which preserves the crystal symmetry. Excitation of only  $A_1$  modes, strong optical absorption at the pump wavelength, and  $\Delta T/T$  oscillation with a  $\cos(\omega t)$  phase, are

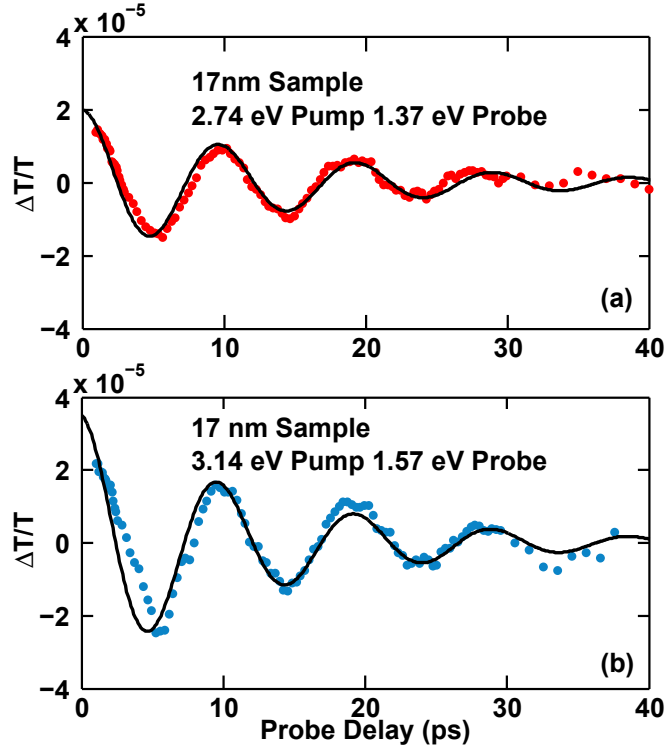


Figure 7.15: OPOP transients by 1.37 and 1.57 eV probes. (a,b) Measured coherent rigid-layer LA phonon oscillations with different pump and probe wavelengths. No significant difference was observed between the 1.37 eV probe experiment(a) and the 1.57 eV probe experiment(b). The 17 nm thick MoS<sub>2</sub> sample has a bandstructure very similar to bulk MoS<sub>2</sub>, which has an indirect-gap at  $\sim 1.3$  eV. The experiment shows that the coherent oscillations are detected by the probe beam through index oscillations. Indirect-gap Pauli-blocking of the probe beam has little contribution to the  $\Delta T/T$  oscillation. Experiments were done at  $T = 300$  K with pump fluence of  $32 \mu\text{J}/\text{cm}^2$ .

the characteristics of coherent DE [184, 47, 141]. DE of coherent phonons have been studied both theoretically and experimentally, and the stimulation of the coherent vibrations could be either from the presence of excited electron-hole pairs, or an abrupt change of carrier temperature [184, 47, 141]. Raman processes should also occur during our ultrafast experiments, and all Raman active modes should be excited, including the shearing modes [189] (which lower the

crystal symmetry). However, other than the OOP breathing mode, all other Raman active modes are absent in our data.

To study the detection mechanism of excited coherent phonon oscillations, a 17 nm sample was excited by 2.74 eV and 3.14 eV pulses, and probed by 1.37 eV and 1.57 eV pulses respectively. Because bulk MoS<sub>2</sub> has an indirect-gap of ~1.3 eV [94], if the probe detects the coherent phonon oscillation through the indirect-gap interband Pauli-blocking, we would expect to see a much smaller oscillation amplitude of  $\Delta T/T$  with the 1.57 eV probe due to the much weaker Pauli-blocking. In Figure 7.15(b), the oscillation amplitude of  $\Delta T/T$  with the 1.57 eV probe is similar to the oscillation amplitude with the 1.37 eV probe in Figure 7.15(a). Hence the oscillation in  $\Delta T/T$  mostly comes from the oscillation of refractive index.

## 7.7 Surface scattering limited coherent phonon lifetime

Temperature and pump fluence dependent experiments were performed to study the loss mechanism of the coherently excited LA phonons in few-layer MoS<sub>2</sub>. In Figure 7.16(a), OPOP experiments were carried out on an 8-layer MoS<sub>2</sub> sample. The pump fluence was varied from  $0.5\mu J/cm^2$  to  $32\mu J/cm^2$  at  $T = 300 K$ , and afterwards the oscillation lifetime was measured again at  $0.5\mu J/cm^2$ . M1 and M8 refer to the first and the 8th measurement respectively. Other than the continuous degradation of the oscillation lifetime as a function of accumulated laser exposure time, no obvious pump fluence dependence was observed. In Figure 7.16(b), for the same 8-layer sample with a  $32\mu J/cm^2$  pump fluence, the measurement M1 was performed at  $T = 300 K$  and the M2 was performed at  $T$

= 5 K. No obvious temperature dependence was observed. However, a continuous degradation of oscillation lifetime was observed as well.

Coherent mechanical oscillations dissipate through several different mechanisms, including thermoelastic damping, the Akhiezer effect, the Landau-Rumer effect, phonon-electron scatterings, anchor losses, and surface scatterings [148, 58, 157, 83]. Thermoelastic damping and the Akhiezer effect are important when phonons propagate in diffusive regime with a quality factor  $Q < 1$ . The Landau-Rumer effect considers phonon-phonon scattering in the ballistic regime and  $Q$  has a very strong temperature dependence. Phonon-electron scatterings are sensitive to the photoexcited electron and hole populations in the sample. Therefore, intrinsic phonon-phonon and phonon-electron scatterings are not dominant dissipation mechanisms according to the temperature and fluence dependent data in Figure 7.16(a,b). We also noticed that if the contact between the MoS<sub>2</sub> samples and the SiO<sub>2</sub> substrate was good, most of the oscillation energy should have been transferred into the quartz substrate due to the similar acoustic impedance between MoS<sub>2</sub> and SiO<sub>2</sub>, meaning the coherent mechanical oscillations could not exist. Thus, we conclude that the contact between the few layer MoS<sub>2</sub> samples and the quartz substrates is not good.

The temperature and pump fluence independent oscillation lifetime, as well as the continuous degradation of oscillation lifetime under laser exposure, imply that surface loss plays an important role in the dissipation mechanism of the measured coherent oscillations as laser exposure only damages the uppermost layer in few-layer TMDs [18]. In order to quantify the bulk and surface dissipation of the observed coherent oscillations, a simple cavity loss model is developed where the quality factor  $Q$  can be expressed in terms of the product

of the oscillations reflectivity in the topmost and lowermost layers  $R_1R_2$ , the loss coefficient in bulk  $\alpha$ , and the sample thickness  $d$ :

$$Q = \frac{1}{2}\omega\tau = \frac{\pi}{2(\alpha d + \log(1 + \sqrt{R_1R_2}))} \quad (7.23)$$

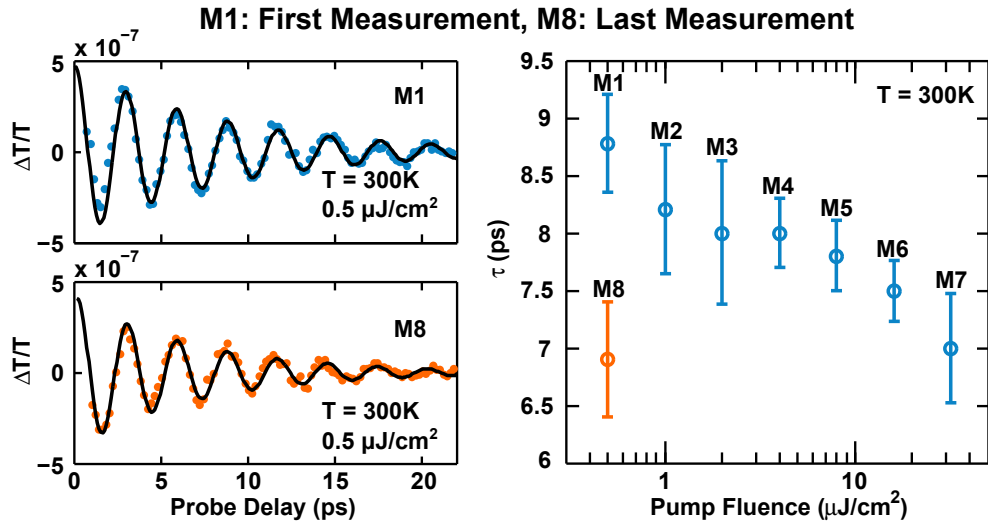
Therefore, by studying the thickness dependence of the quality factor  $Q$ , both the bulk and surface loss can be quantified. In Figure 7.17(a), quality factors of 37 MoS<sub>2</sub> samples are plotted. Measurements were done at  $T = 300$  K with a pump fluence of  $32\mu J/cm^2$ . Other than a random distribution with a mean of 10.4 and a standard deviation of 5, the quality factors do not have an obvious sample thickness dependence. Interestingly, as in Figure 7.17(a inset), the statistical distribution of the measured quality factors can be fit very well by a “log-normal” distribution, which enforces the condition that  $Q$  cannot be smaller than zero. The “log-normal” distribution implies that the measured quality factors are completely random. Due to the lack of thickness dependence, we conclude that surface loss is the major dissipation mechanism, and the bulk loss is not important. Furthermore, the random distribution of the  $Q$  matches our expectation of random sample surface qualities after exfoliation.

For high frequency MEMS, as the devices continue getting smaller and thinner, surface loss starts to overwhelm intrinsic loss mechanisms, and is under intensive study in recent years [58, 40, 157]. Experimental and theoretical studies show that if the surface loss of a mechanical resonator is dominated by quantum Two Level Systems (TLS) with a low activation temperature  $T_{ac}$ , quality factor has a weak temperature dependence ranging from  $Q \propto T^{-0.5}$  to  $Q \propto T^{-0.2}$  below  $T_{ac}$ , and becomes temperature independent above  $T_{ac}$  [132, 58, 40, 69, 113]. Our data in Figure 7.16(b) is consistent with the TLS model, and the surface loss was

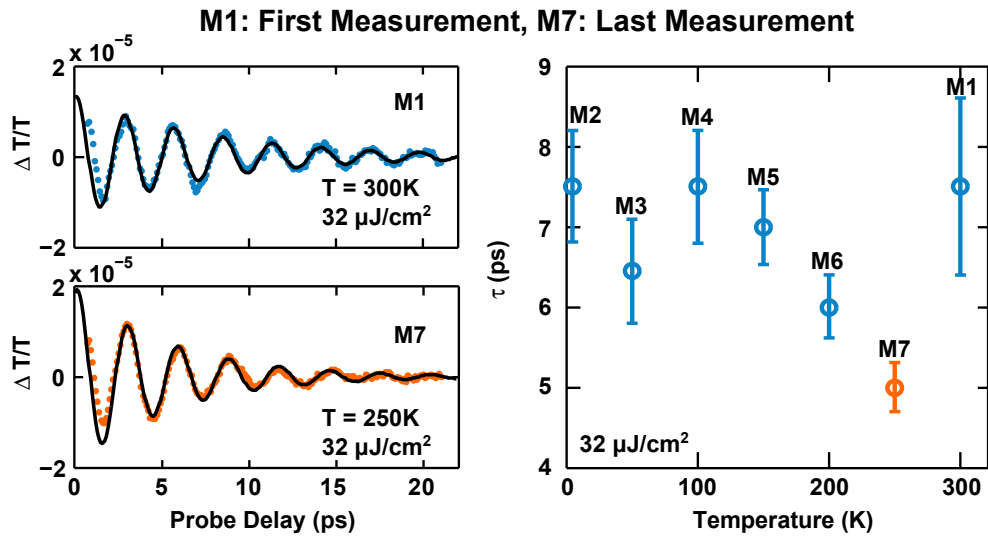
so large that other intrinsic loss mechanisms were completely overwhelmed in the entire temperature range measured.

## 7.8 Discussion

In this chapter, the photoexcitation and detection of coherent OOP rigid-layer breathing mode oscillations of few-layer MoS<sub>2</sub> are discussed. The coherent mechanical oscillations were excited by displacive excitation and detected through index oscillations. The quality factors of the excited coherent LA phonon oscillations do not depend on substrate temperature, pump fluence or layer thickness, meaning the quality factors are surface loss limited. Because the oscillation frequency is higher in thinner samples, and the oscillation  $Q$  is independent of sample thickness, the  $Freq \times Q$  scales as  $1/N$ , where  $N$  is the number of layers in the sample. In Figure 7.17(b), the  $Freq \times Q$  is over  $1 \times 10^{13}$  Hz in a 3-layer sample at  $\sim 860$  GHz room temperature. This is approaching the theoretical limits of  $Freq \times Q$  in common MEMS materials [157], such as AlN, Si and SiO<sub>2</sub> as in Figure 7.5. Advances of MEMS devices in high frequency applications rely on fabrication technology. It becomes challenging to produce resonators and oscillators operating beyond 10 GHz while maintaining a  $Freq \times Q$  above  $1 \times 10^{13}$  Hz [157, 40, 132]. Bulk TMDs are centrosymmetric and do not have piezoelectricity in the out-of-plane direction, but the centrosymmetry can be broken by the substrate for few-layer samples. In few layer TMDs, the out-of-plane piezoelectricity might be enhanced by choosing a proper substrate, and the out-of-plane mechanical oscillations in few-layer TMDs might be a plausible solution for THz MEMS devices operating at room temperature.



(a)



(b)

Figure 7.16: Pump fluence and temperature dependent oscillation lifetime. Pump fluence(a) and temperature(b) dependent oscillation lifetime on an 8 layer sample. The labels refer to the time sequence of the experiments, and a continuous degradation of oscillation lifetime was observed as a function of accumulated laser exposure time. No observable pump fluence and temperature dependence was found. Error-bars represent the upper and lower bounds of the extracted lifetime for each measurement.

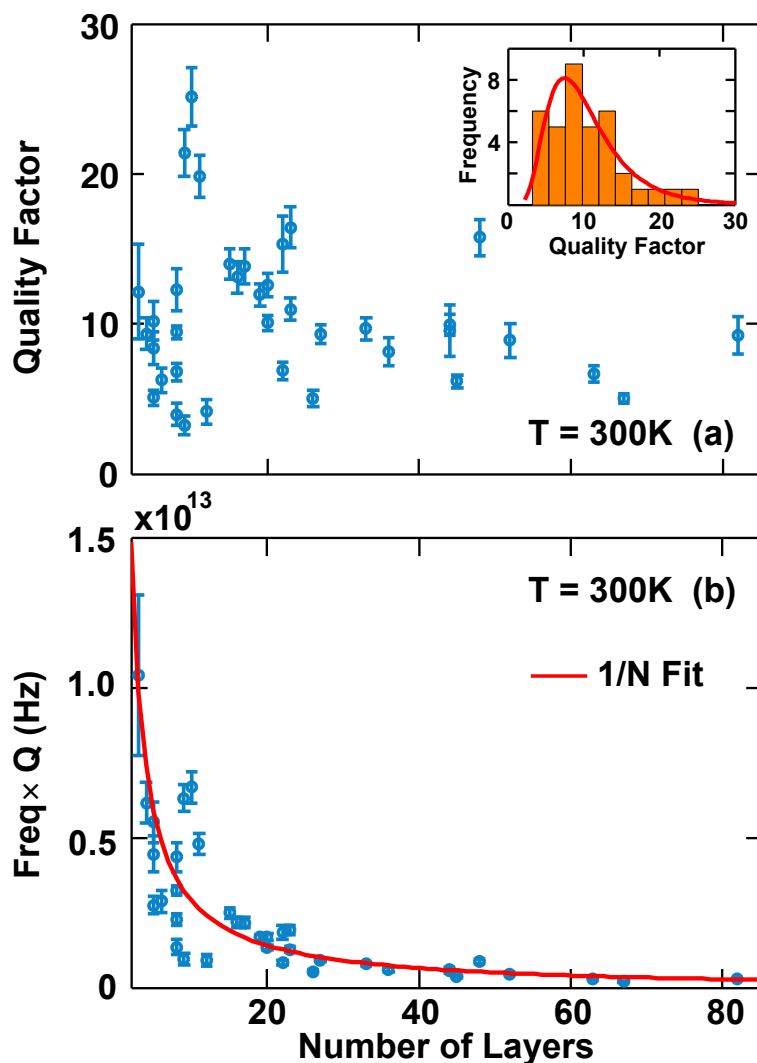


Figure 7.17: Quality factors and FQ products of few layer MoS<sub>2</sub> samples. (a) The quality factors (Q) of the measured samples do not have a dependence on the sample thickness. The statistical distribution of the quality factors is plotted in the inset, and the distribution can be fit well by a "log-normal" function. Error-bars represent the upper and lower bounds of the extracted Q for each measurement. (b) The FQ product of few-layer MoS<sub>2</sub> can reach over  $1 \times 10^{13}$  Hz in a 3 layer MoS<sub>2</sub> sample with an oscillation frequency of  $\sim 860$  GHz.

## APPENDIX A

### EXFOLIATION OF 2D MATERIALS

Since the discovery of graphene, exfoliation has been the most reliable and simple technique to produce monolayer materials from their bulk form [108]. In this appendix, we will briefly go through the standard exfoliation process.

#### A.1 Substrate selection

Most layered materials are exfoliated onto silicon substrates with 90 or 285 *nm* oxide in order to have maximum visual contrast of atomic thin samples under microscopes [183]. Because monolayer materials normally have low 2D optical conductivity in the visible spectrum, they do not reflect very much light unless constructive interference occurs. The general recommendation is to use highly doped silicon substrates with 285 *nm* dry thermal oxide. Dopants in moderately doped and high resistivity silicon wafers could be completely frozen out at cryogenic temperatures (the back-gate is no longer controllable). To avoid back-gate oxide breakdown, the metal contact pads for wire bonding should be at least 100 *nm* thick. 285 *nm* oxide silicon substrates are also less likely to suffer from gate leakage compared to 90 *nm* oxide wafers.

The quartz wafer is the most commonly used optically transparent substrate. When searching for monolayer samples on quartz substrates under microscopes, the visual contrast can be enhanced by using short-pass optical filters for the illumination light. Among different types of quartz substrates, high-temperature fused silica wafers are the best for transmission and reflec-

tion spectroscopies due to their superior performance in the UV and near-IR range. Compared to silicon wafers with thermal oxide, fused silica wafers suffer from surface roughness (few *nm* RMS vs sub *nm* RMS roughness of thermal oxide) and contamination problems (samples are found to be more doped when exfoliated onto fused silica substrates). These two problems can be mitigated by purchasing specially polished fused silica wafers and a subsequent hot-piranha rinse before exfoliation. Fortunately, transmission and reflection measurements of 2D materials are generally less sensitive to the surface quality of the substrate. On the other hand, photoluminescence (PL) experimental results can be greatly influenced by the substrate.

## **A.2 Substrate preparation**

Before exfoliation, the substrate should be patterned with coordinate marks and alignment keys. The coordinate marks serve two purposes: (1) They mark the position of the sample on the substrate. These coordinates make it much easier to find the exfoliated sample later on. (2) During device layout, mapping the coordinate marks of the microscope image onto the substrate CAD file guarantees that the Electron-beam lithography exposure is correctly aligned. The E-beam alignment keys are two perpendicular lines (3  $\mu\text{m}$  in width and a *mm* long) with arrows pointing towards the centers of the keys. These alignment keys are designed such that the E-Beam tool can perform the auto-alignment easily. A cartoon illustration of a patterned wafer is shown in Figure A.1.

After the alignment keys and alignment marks are patterned onto the photoresist (positive mask), there are several options to make them permanent on

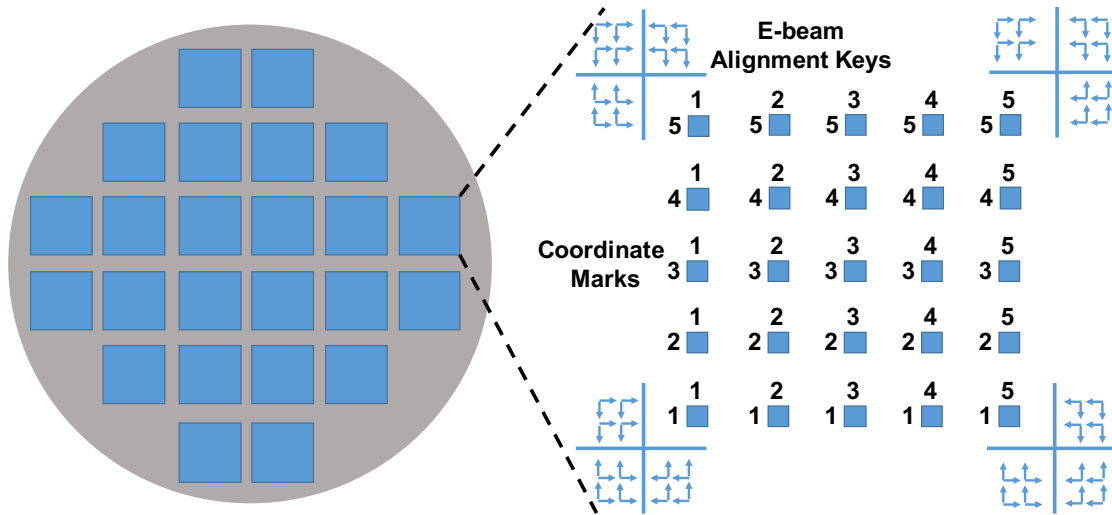


Figure A.1: Substrate preparation for exfoliation. Within each die, it is recommended to have both alignment keys (for lithography) and coordinate marks (for CAD design).

the substrate. One option is to use a Reactive Ion Etcher (RIE) to etch the alignment features into the wafer. For quartz substrates, 200~300  $\mu\text{m}$  oxide RIE etch can result in enough contrast to find the marks under microscope. These alignment patterns are visible to photolithography tools using optical alignment methods (contact aligner or stepper). E-Beam lithography will not be possible as quartz substrate is not conducting (the etched trenches do not have contrast under SEM). For silicon substrates, the RIE must etch through the oxide layer. The exposed silicon substrate is conducting and hence can be used for E-Beam lithography. However, it is still not trivial for the E-Beam tools to perform auto-alignment due to the lack of contrast.

The biggest advantage of the RIE etched marks is the flexibility of the substrate surface treatment. Hot piranha is commonly used to clean up the surface before exfoliation. Oxygen plasma cleaning can be used for surface treatments as well, but  $\text{O}_2$  plasma cleaning introduces surface roughness as well as surface

charges. It is also known that  $O_2$  plasma cleaning can improve substrate surface adhesion for exfoliation, but at the same time the device performance can be degraded [57].

Alignment marks and keys can be made by metal deposition as well. During metal deposition, a few *nm* of chromium or titanium is used as an adhesion layer, and then 50 to 100 *nm* of gold is deposited. These alignment keys/marks are great for E-beam lithography because of the superior contrast of the gold marks compared to the etched oxide marks. However, surface treatment becomes difficult as most plasma and acid treatments can cause damage to the gold marks.

### **A.3 Exfoliation**

The Scotch tape method is the most popular exfoliation technique for preparing 2D samples. Depending on the crystal quality and the strength of Van der Waals force between adjacent layers, some layered materials are more difficult to exfoliate than others. For example, graphene exfoliation is easier than  $MoS_2$  and  $WSe_2$ .

The grain size of the bulk crystal fundamentally limits the size of the exfoliated samples. During the Scotch tape exfoliation, to avoid wrinkling the tape, it is best to apply a small and steady force to separate the pieces of tapes. In addition, to maximize the exfoliation yield, one needs to find the optimum number of Scotch tape exfoliations before transferring the final tape to the substrate. Once the final tape is transferred onto the substrate, multiple techniques can be used to squeeze out the air between the sample and the substrate. One simple

method is to use a pen to apply pressure to the tape on the substrate for about 3 to 5 minutes. Occasionally, a subsequent vacuum pumping can also improve sample adhesion. The detailed Scotch tape exfoliation method is explained in Figure A.2

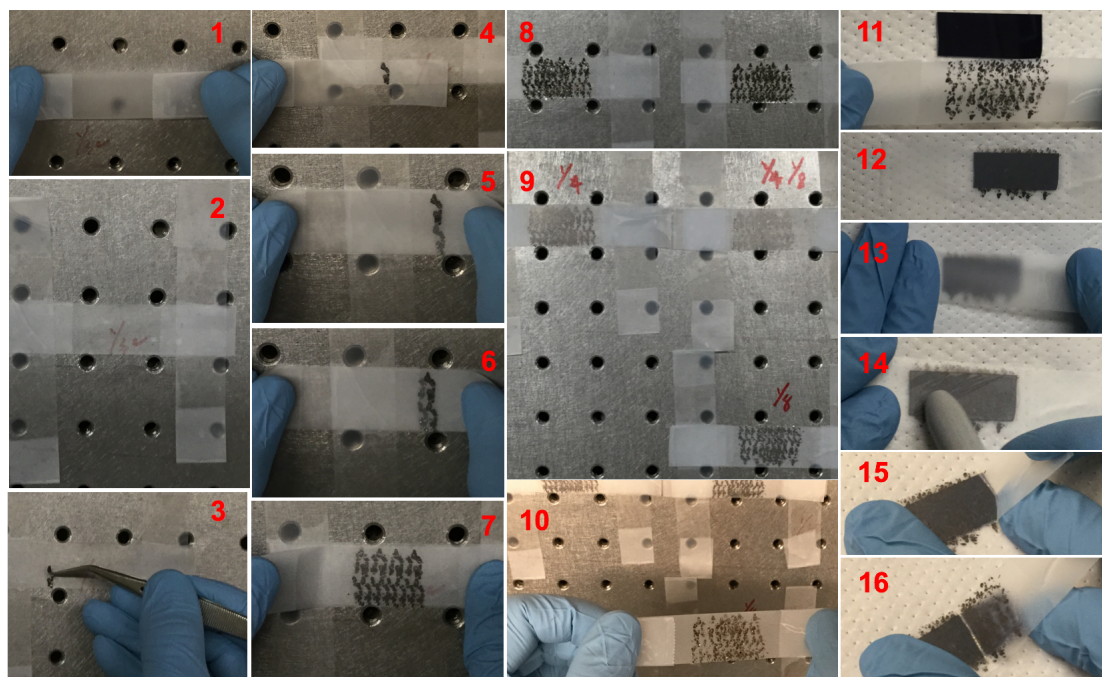


Figure A.2: Scotch tape exfoliation method.(1) Prepare a one inch long piece of Scotch tape (facing up) with two folded-ends. (2) Fasten the Scotch tape to the table. (3) Place bulk crystal to the Scotch tape. (4) Use another Scotch tape (same in dimension) to start exfoliating the bulk crystal. (5,6,7) Perform exfoliation until thin bulk crystals fill the entire tape. (8) Peel off the Scotch tapes from each other and fasten them onto the table. (9) Perform tape-to-tape exfoliation until reaching the optimum thickness for exfoliation. The fraction numbers refer to the relative thickness of the tape. (10) Take one tape ( $1/8$  thickness in this case). (11,12) Place it onto the target substrate. (13) Put more tape on top of the exfoliation tape to protect it from breaking. (14) Apply pressure to the tape on the substrate with a pen for a few minutes. (15,16) Hold the substrate from one end and slowly peel off the exfoliation tape with a small angle and steady force.

Recently, to reduce glue residues from the Scotch tape exfoliation method, PDMS exfoliation has become more popular. For MoS<sub>2</sub>, PDMS from Gel-Pak (PF film with retention X4) can produce larger and cleaner exfoliated samples than Scotch tape. The PMDS method is illustrated in Figure A.3.

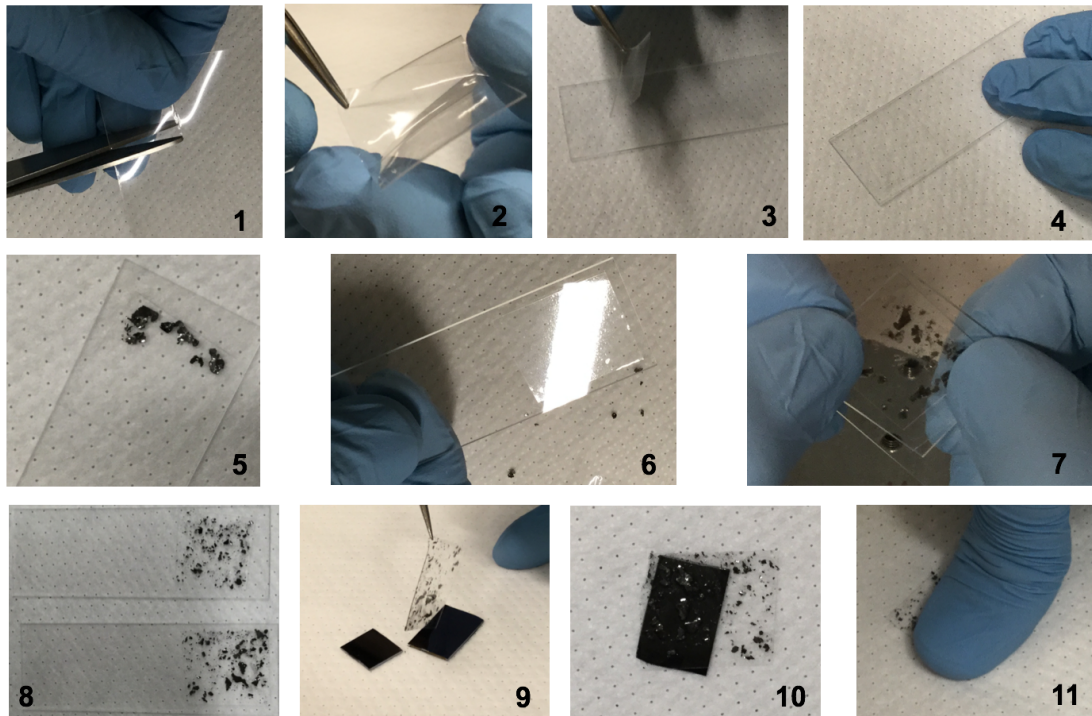


Figure A.3: PDMS exfoliation method. (1) Cut one-inch square PDMS PF film (Gel-Pak). (2) Peel off the front plastic cover, then peel off PDMS film. (3) Place the PDMS film onto a clean microslide, which must be dust free. (4) Make sure there are no bubbles underneath the PDMS. (5) Place bulk crystal onto the PDMS film. (6) Prepare another microslide with PDMS film. (7) Exfoliate the bulk crystal between the PDMS films. (8) Exfoliate till the PDMS film is filled with thin bulk crystals. (9) Peel off the PDMS film from the microslide. (10) Place the PDMS film onto the target substrate. (11) Press the PDMS film on the target substrate for several minutes before peeling it off.

## A.4 E-beam lithography on quartz wafers

Because quartz is not non-conducting, accumulated electrons cannot be discharged through the quartz substrate. This makes E-beam lithography difficult on quartz. A failed E-beam exposure is shown in Figure A.4. The lightning strikes shown on PMMA are due to the sudden discharge of the accumulated electrons on the quartz wafer.



Figure A.4: E-beam lithography on a quartz substrate. The lightning strikes on the PMMA are due to the sudden discharge of the accumulated electrons on the quartz wafer.

To pattern features on a quartz substrate by E-beam lithography, a discharging layer is required. As shown in Figure A.4, a 5 *nm* layer of thermal evaporated gold can solve the electron discharging problem. Electron beam evaporation and sputtering are not recommended techniques for the gold deposition because they might accidentally expose the PMMA.

## BIBLIOGRAPHY

- [1] Mazhar N. Ali, Jun Xiong, Steven Flynn, Jing Tao, Quinn D. Gibson, Leslie M. Schoop, Tian Liang, Neel Haldolaarachchige, Max Hirschberger, N. P. Ong, and R. J. Cava. Large, non-saturating magnetoresistance in wte2. *Nature*, 514(7521):205–208, 10 2014.
- [2] Matthew J. Allen, Vincent C. Tung, and Richard B. Kaner. Honeycomb carbon: A review of graphene. *Chemical Reviews*, 110(1):132–145, 2010. PMID: 19610631.
- [3] Densi M. Basko Andrea C. Ferrai. Raman spectroscopy as a versatile tool for studying the properties of graphene. *Nature nanotechnology*, 8:235–246, 2010.
- [4] Britton W. H. Baugher, Hugh O. H. Churchill, Yafang Yang, and Pablo Jarillo-Herrero. Optoelectronic devices based on electrically tunable pn diodes in a monolayer dichalcogenide. *Nature Nanotechnology*, 9:262–267, 2014.
- [5] Claire Berger, Zhimin Song, Xuebin Li, Xiaosong Wu, Nate Brown, Cécile Naud, Didier Mayou, Tianbo Li, Joanna Hass, Alexei N. Marchenkov, Edward H. Conrad, Phillip N. First, and Walt A. de Heer. Electronic confinement and coherence in patterned epitaxial graphene. *Science*, 312(5777):1191–1196, 2006.
- [6] Marco Bernardi, Maurizia Palummo, and Jeffrey C. Grossman. Extraordinary sunlight absorption and one nanometer thick photovoltaics using two-dimensional monolayer materials. *Nano Letters*, 13(8):3664–3670, 2013. PMID: 23750910.
- [7] Marco Bernardi, Maurizia Palummo, and Jeffrey C. Grossman. Extraordinary sunlight absorption and one nanometer thick photovoltaics using two-dimensional monolayer materials. *Nano Letters*, 13(8):3664–3670, 2013. PMID: 23750910.
- [8] Simone Bertolazzi, Jacopo Brivio, and Andras Kis. Stretching and breaking of ultrathin mos2. *ACS Nano*, 5(12):9703–9709, 2011. PMID: 22087740.
- [9] Elisabeth Bianco, Sheneve Butler, Shishi Jiang, Oscar D. Restrepo, Wolfgang Windl, and Joshua E. Goldberger. Stability and exfoliation of germanane: A germanium graphane analogue. *ACS Nano*, 7(5):4414–4421, 2013. PMID: 23506286.

- [10] R. Bistritzer and A. H. MacDonald. Hydrodynamic theory of transport in doped graphene. *Phys. Rev. B*, 80:085109, Aug 2009.
- [11] J. S. Blakemore. Lifetime in *p*-type silicon. *Phys. Rev.*, 110:1301–1308, Jun 1958.
- [12] Robert Bogue. Recent developments in mems sensors: a review of applications, markets and technologies. *Sensor Review*, 33(4):300–304, 2013.
- [13] Francesco Bonaccorso, Luigi Colombo, Guihua Yu, Meryl Stoller, Valentina Tozzini, Andrea C. Ferrari, Rodney S. Ruoff, and Vittorio Pellegrini. Graphene, related two-dimensional crystals, and hybrid systems for energy conversion and storage. *Science*, 347(6217), 2015.
- [14] Nicola Bonini, Michele Lazzeri, Nicola Marzari, and Francesco Mauri. Phonon anharmonicities in graphite and graphene. *Phys. Rev. Lett.*, 99:176802, Oct 2007.
- [15] Markus Breusing, Claus Ropers, and Thomas Elsaesser. Ultrafast carrier dynamics in graphite. *Phys. Rev. Lett.*, 102:086809, Feb 2009.
- [16] S. Butscher, F. Milde, M. Hirtschulz, E. Mali, and A. Knorr. Hot electron relaxation and phonon dynamics in graphene. *Applied Physics Letters*, 91(20), 2007.
- [17] J. Buus and M. Amann. *Tuneable Laser diodes*. Artech House Publishers, New York, USA, 1 edition, 1998.
- [18] A. Castellanos-Gomez, M. Barkelid, A. M. Goossens, V. E. Calado, H. S. J. van der Zant, and G. A. Steele. Laser-thinning of mos2: On demand generation of a single-layer semiconductor. *Nano Letters*, 12(6):3187–3192, 2012.
- [19] Andres Castellanos-Gomez, Ronald van Leeuwen, Michele Buscema, Herre S. J. van der Zant, Gary A. Steele, and Warner J. Venstra. Single-layer mos2 mechanical resonators. *Advanced Materials*, 25(46):6719–6723, 2013.
- [20] A. H. Castro Neto. Charge density wave, superconductivity, and anomalous metallic behavior in 2d transition metal dichalcogenides. *Phys. Rev. Lett.*, 86:4382–4385, May 2001.

- [21] Biswanath Chakraborty, Achintya Bera, D. V. S. Muthu, Somnath Bhowmick, U. V. Waghmare, and A. K. Sood. Symmetry-dependent phonon renormalization in monolayer  $\text{mos}_2$  transistor. *Phys. Rev. B*, 85:161403, Apr 2012.
- [22] Tawinan Cheiwchanchamnangij and Walter R. L. Lambrecht. Quasiparticle band structure calculation of monolayer, bilayer, and bulk  $\text{mos}_2$ . *Phys. Rev. B*, 85:205302, May 2012.
- [23] D. S. Chemla and D. A. B. Miller. Room-temperature excitonic nonlinear-optical effects in semiconductor quantum-well structures. *J. Opt. Soc. Am. B*, 2(7):1155–1173, Jul 1985.
- [24] T. K. Cheng, S. D. Brorson, A. S. Kazeroonian, J. S. Moodera, G. Dresselhaus, M. S. Dresselhaus, and E. P. Ippen. Impulsive excitation of coherent phonons observed in reflection in bismuth and antimony. *Applied Physics Letters*, 57(10):1004–1006, 1990.
- [25] G. C. Cho, W. Kütt, and H. Kurz. Subpicosecond time-resolved coherent-phonon oscillations in gaas. *Phys. Rev. Lett.*, 65:764–766, Aug 1990.
- [26] Kyungjune Cho, Tae-Young Kim, Woanseong Park, Juhun Park, Dongku Kim, Jingon Jang, Hyunhak Jeong, Seunghun Hong, and Takhee Lee. Gate-bias stress-dependent photoconductive characteristics of multi-layer  $\text{mos}_2$  field-effect transistors. *Nanotechnology*, 25:155201, June 2014.
- [27] S. C. Choo. Carrier lifetimes in semiconductors with two interacting or two independent recombination levels. *Phys. Rev. B*, 1:687–696, Jan 1970.
- [28] David Cohen-Tanugi and Jeffrey C. Grossman. Water desalination across nanoporous graphene. *Nano Letters*, 12(7):3602–3608, 2012. PMID: 22668008.
- [29] A. J. Sabba D. M. Riffe. Coherent excitation of the optic phonon in si: Transiently stimulated raman scattering with a finite-lifetime electronic excitation. *Physical Review B*, 76:085207, 2007.
- [30] Yaping Dan, Kwanyong Seo, Kuniharu Takei, Jhim H. Meza, Ali Javey, and Kenneth B. Crozier. Dramatic reduction of surface recombination by in situ surface passivation of silicon nanowires. *Nano Letters*, 11(6):2527–2532, 2011. PMID: 21598980.

- [31] Jahan M. Dawlaty, Shriram Shivaraman, Mvs Chandrashekhar, Farhan Rana, and Michael G. Spencer. Measurement of ultrafast carrier dynamics in epitaxial graphene. *Applied Physics Letters*, 92(4), 2008.
- [32] Jahan M. Dawlaty, Shriram Shivaraman, Jared H. Strait, Paul A. George, Mvs Chandrashekhar, Farhan Rana, Michael G. Spencer, Dmitry Veksler, and Yunqing Chen. Measurement of the optical absorption spectra of epitaxial graphene from terahertz to visible. *Applied Physics Letters*, 93:131905, 2008.
- [33] T. Dekorsy, T. Pfeifer, W. Kütt, and H. Kurz. Subpicosecond carrier transport in gas surface-space-charge fields. *Phys. Rev. B*, 47:3842–3849, Feb 1993.
- [34] Callum J. Docherty, Patrick Parkinson, Hannah J. Joyce, Ming-Hui Chiu, Chang-Hsiao Chen, Ming-Yang Lee, Lain-Jong Li, Laura M. Herz, and Michael B. Johnston. Ultrafast transient terahertz conductivity of monolayer mos2 and wse2 grown by chemical vapor deposition. *ACS Nano*, 8(11):11147–11153, 2014.
- [35] S. Donati. *Photodetectors: Devices, Circuits and Applications*. Prentice Hall, New York, USA, 1999.
- [36] Jason K. Ellis, Melissa J. Lucero, and Gustavo E. Scuseria. The indirect to direct band gap transition in multilayered mos2 as predicted by screened hybrid density functional theory. *Applied Physics Letters*, 99(26):–, 2011.
- [37] Andrey N. Enyashin, Maya Bar-Sadan, Lothar Houben, and Gotthard Seifert. Line defects in molybdenum disulfide layers. *The Journal of Physical Chemistry C*, 117(20):10842–10848, 2013.
- [38] H. Y. Fan. *Effects of Free Carriers on the Optical Properties*, volume 3. Academic Press, New York, USA, 1967.
- [39] Ji Feng, Xiaofeng Qian, Cheng-Wei Huang, and Ju Li. Strain-engineered artificial atom as a broad-spectrum solar energy funnel. *Nat Photon*, 6(12):866–872, Dec 2012.
- [40] X. L. Feng, C. A. Zorman, M. Mehregany, and M. L. Roukes. Dissipation in single-crystal 3c-sic ultra-high frequency nanomechanical resonators. *arXiv:cond-mat/0606711*, Jun 2006.

- [41] S. Fratini and F. Guinea. Substrate-limited electron dynamics in graphene. *Phys. Rev. B*, 77:195415, May 2008.
- [42] Javier D. Fuhr, Andrés Saúl, and Jorge O. Sofo. Scanning tunneling microscopy chemical signature of point defects on the mos<sub>2</sub>(0001) surface. *Phys. Rev. Lett.*, 92:026802, Jan 2004.
- [43] Marco M. Furchi, Dmitry K. Polyushkin, Andreas Pospischil, and Thomas Mueller. Mechanisms of photoconductivity in atomically thin mos<sub>2</sub>. *Nano Letters*, 14(11):6165–6170, 2014. PMID: 25299515.
- [44] Marco M. Furchi, Andreas Pospischil, Florian Libisch, Joachim Burgdrfer, and Thomas Mueller. Photovoltaic effect in an electrically tunable van der waals heterojunction. *Nano Letters*, 14(8):4785–4791, 2014. PMID: 25057817.
- [45] Nathaniel M. Gabor, Zhaohui Zhong, Ken Bosnick, and Paul L. McEuen. Ultrafast photocurrent measurement of the escape time of electrons and holes from carbon nanotube *p-i-n* photodiodes. *Phys. Rev. Lett.*, 108:087404, Feb 2012.
- [46] R Garg, B Inder, and M Bozzi. *Microstrip Lines and Slotlines*. Artech House, Artech House.
- [47] G. A. Garrett, T. F. Albrecht, J. F. Whitaker, and R. Merlin. Coherent thz phonons driven by light pulses and the sb problem: What is the mechanism? *Phys. Rev. Lett.*, 77:3661–3664, Oct 1996.
- [48] Shaofeng Ge, Xuefeng Liu, Xiaofen Qiao, Qinsheng Wang, Zhen Xu, Jun Qiu, Ping-Heng Tan, Jimin Zhao, and Dong Sun. Coherent longitudinal acoustic phonon approaching thz frequency in multilayer molybdenum disulphide. *Scientific Reports*, 4:5722 EP –, Jul 2014. Article.
- [49] A. K. Geim and I. V. Grigorieva. Van der waals heterostructures. *Nature*, 499(7459):419–425, 07 2013.
- [50] Paul A. George, Jared Strait, Jahan Dawlaty, Shriram Shivaraman, Mvs Chandrashekhar, Farhan Rana, and Michael G. Spencer. Ultrafast optical-pump terahertz-probe spectroscopy of the carrier relaxation and recombination dynamics in epitaxial graphene. *Nano Letters*, 8(12):4248–4251, 2008. PMID: 18989983.

- [51] Matt W. Graham, Su-Fei Shi, Daniel C. Ralph, Jiwoong Park, and Paul L. McEuen. Photocurrent measurements of supercollision cooling in graphene. *Nat Phys*, 9(2):103–108, Feb 2013.
- [52] A. Haug. Auger recombination with traps in quantum-well semiconductors. *Applied Physics A*, 56(6):567–569, 1993.
- [53] J. R. Haynes and J. A. Hornbeck. Trapping of minority carriers in silicon. ii. *n*-type silicon. *Phys. Rev.*, 100:606–615, Oct 1955.
- [54] Volker Heine. *Group Theory in Quantum Mechanics*. Pergamon Press, 1960.
- [55] C. H. Henry and D. V. Lang. Nonradiative capture and recombination by multiphonon emission in GaAs and GaP. *Phys. Rev. B*, 15:989–1016, Jan 1977.
- [56] J. A. Hornbeck and J. R. Haynes. Trapping of minority carriers in silicon. i. *p*-type silicon. *Phys. Rev.*, 97:311–321, Jan 1955.
- [57] Yuan Huang, Eli Sutter, Norman N. Shi, Jiabao Zheng, Tianzhong Yang, Dirk Englund, Hong-Jun Gao, and Peter Sutter. Reliable exfoliation of large-area high-quality flakes of graphene and other two-dimensional materials. *ACS Nano*, 9(11):10612–10620, 2015. PMID: 26336975.
- [58] Matthias Imboden and Pritiraj Mohanty. Dissipation in nanoelectromechanical systems. *Physics Reports*, 534(3):89 – 146, 2014. Dissipation in nano-electromechanical systems.
- [59] Tielrooij K. J., Piatkowski L., Massicotte M., Woessner A., Ma Q., Lee Y., Myro K. S., Lau C. N., Jarillo-Herrero P., van Hulst N. F., and Koppens F. H. L. Generation of photovoltage in graphene on a femtosecond timescale through efficient carrier heating. *Nat Nano*, 10(5):437–443, 05 2015.
- [60] John David Jackson. *Classical Electrodynamics*. Wiley, 2001.
- [61] Deep Jariwala, Vinod K. Sangwan, Dattatray J. Late, James E. Johns, Vinayak P. Dravid, Tobin J. Marks, Lincoln J. Lauhon, and Mark C. Hersam. Band-like transport in high mobility unencapsulated single-layer *mos2* transistors. *Applied Physics Letters*, 102(17):173107, 2013.
- [62] G. E. Jellison and F. A. Modine. Optical functions of silicon at elevated temperatures. *Journal of Applied Physics*, 76(6):3758–3761, 1994.

- [63] R. Colin Johnson. MemS market: Ups and upstarts. *EE Times*, 2015.
- [64] Kristen Kaasbjerg, K. S. Bhargavi, and S. S. Kubakaddi. Hot-electron cooling by acoustic and optical phonons in monolayers of  $\text{mos}_2$  and other transition-metal dichalcogenides. *Phys. Rev. B*, 90:165436, Oct 2014.
- [65] Tobias Kampfrath, Luca Perfetti, Florian Schapper, Christian Frischkorn, and Martin Wolf. Strongly coupled optical phonons in the ultrafast dynamics of the electronic energy and current relaxation in graphite. *Phys. Rev. Lett.*, 95:187403, Oct 2005.
- [66] R. Kappera, D. Voiry, S. E. Yalcin, B. Branch, G. Gupta, A. D. Mohite, and M Chhowalla. Phase-engineered low-resistance contacts for ultrathin  $\text{mos}_2$  transistors. *Nature Materials*, 13:1128–1134, 2014.
- [67] Keun Soo Kim, Yue Zhao, Houk Jang, Sang Yoon Lee, Jong Min Kim, Kwang S. Kim, Jong-Hyun Ahn, Philip Kim, Jae-Young Choi, and Byung Hee Hong. Large-scale pattern growth of graphene films for stretchable transparent electrodes. *Nature*, 457(7230):706–710, 02 2009.
- [68] Youngjin Kim, Yuwon Park, Aram Choi, Nam-Soon Choi, Jeongsoo Kim, Junesoo Lee, Ji Heon Ryu, Seung M. Oh, and Kyu Tae Lee. An amorphous red phosphorus/carbon composite as a promising anode material for sodium ion batteries. *Advanced Materials*, 25(22):3045–3049, 2013.
- [69] R. N. Kleiman, G. Agnolet, and D. J. Bishop. Two-level systems observed in the mechanical properties of single-crystal silicon at low temperatures. *Phys. Rev. Lett.*, 59:2079–2082, Nov 1987.
- [70] V. I. Klimov, D. W. McBranch, C. A. Leatherdale, and M. G. Bawendi. Electron and hole relaxation pathways in semiconductor quantum dots. *Phys. Rev. B*, 60:13740–13749, Nov 1999.
- [71] Hannu-Pekka Komsa, Jani Kotakoski, Simon Kurasch, Ossi Lehtinen, Ute Kaiser, and Arkady V. Krasheninnikov. Two-dimensional transition metal dichalcogenides under electron irradiation: Defect production and doping. *Phys. Rev. Lett.*, 109:035503, Jul 2012.
- [72] F. H. L. Koppens, T. Mueller, Ph. Avouris, A. C. Ferrari, M. S. Vitiello, and M. Polini. Photodetectors based on graphene, other two-dimensional materials and hybrid systems. *Nat Nano*, 9(10):780–793, 10 2014.

- [73] T. Korn, S. Heydrich, M. Hirmer, J. Schmutzler, and C. Schller. Low-temperature photocarrier dynamics in monolayer mos<sub>2</sub>. *Applied Physics Letters*, 99:102109, 2011.
- [74] Todd D. Krauss and Frank W. Wise. Coherent acoustic phonons in a semiconductor quantum dot. *Phys. Rev. Lett.*, 79:5102–5105, Dec 1997.
- [75] W.A. Kutt, W. Albrecht, and H. Kurz. Generation of coherent phonons in condensed media. *Quantum Electronics, IEEE Journal of*, 28(10):2434–2444, Oct 1992.
- [76] D. Lagarde, L. Bouet, X. Marie, C. R. Zhu, B. L. Liu, T. Amand, P. H. Tan, and B. Urbaszek. Carrier and polarization dynamics in monolayer mos<sub>2</sub>. *Phys. Rev. Lett.*, 112:047401, Jan 2014.
- [77] Peter T. Landsberg. *Recombination in Semiconductors*. Cambridge University Press, cambridge, UK, 1 edition, 1992.
- [78] Melvin Lax. Cascade capture of electrons in solids. *Phys. Rev*, 119:1502–1523, 1960.
- [79] Changgu Lee, Huguen Yan, Louis E. Brus, Tony F. Heinz, James Hone, and Sunmin Ryu. Anomalous lattice vibrations of single- and few-layer mos<sub>2</sub>. *ACS Nano*, 4(5):2695–2700, 2010. PMID: 20392077.
- [80] I. H. Lee, K. J. Yee, K. G. Lee, E. Oh, D. S. Kim, and Y. S. Lim. Coherent optical phonon mode oscillations in wurtzite zno excited by femtosecond pulses. *Journal of Applied Physics*, 93(8):4939–4941, 2003.
- [81] Jaesung Lee, Zenghui Wang, Keliang He, Jie Shan, and Philip X.-L. Feng. High frequency mos<sub>2</sub> nanomechanical resonators. *ACS Nano*, 7(7):6086–6091, 2013. PMID: 23738924.
- [82] Likai Li, Yijun Yu, Guo Jun Ye, Qingqin Ge, Xuedong Ou, Hua Wu, Donglai Feng, Xian Hui Chen, and Yuanbo Zhang. Black phosphorus field-effect transistors. *Nat Nano*, 9(5):372–377, 05 2014.
- [83] Ron Lifshitz and M. L. Roukes. Thermoelastic damping in micro- and nanomechanical systems. *Phys. Rev. B*, 61:5600–5609, Feb 2000.
- [84] Keith A. Nelson Lisa Dhar, John A. Rogers. Time-resolved vibrational spectroscopy in the impulsive limit. *Chemical Review*, 94:157–193, 1994.

- [85] D. Liu, Y. Guo, L. Fang, and J. Robertson. Sulfur vacancies in monolayer mos<sub>2</sub> and its electrical contacts. *Applied Physics Letters*, 103(18):18113, 2013.
- [86] Mingzhen Liu, Michael B. Johnston, and Henry J. Snaith. Efficient planar heterojunction perovskite solar cells by vapour deposition. *Nature*, 501(7467):395–398, 09 2013.
- [87] Rongliang Liu, G. D. Sanders, C. J. Stanton, Chang Sub Kim, J. S. Yahng, Y. D. Jho, K. J. Yee, E. Oh, and D. S. Kim. Femtosecond pump-probe spectroscopy of propagating coherent acoustic phonons in in<sub>x</sub>ga<sub>1-x</sub>NGaN heterostructures. *Phys. Rev. B*, 72:195335, Nov 2005.
- [88] Zhuang Liu, Joshua T. Robinson, Xiaoming Sun, and Hongjie Dai. Pegylated nanographene oxide for delivery of water-insoluble cancer drugs. *Journal of the American Chemical Society*, 130(33):10876–10877, 2008. PMID: 18661992.
- [89] Oriol Lopez-Sanchez, Dominik Lembke, Metin Kayci, Aleksandra Radenovic, and Andras Kis. Ultrasensitive photodetectors based on monolayer mos<sub>2</sub>. *Nature Nanotechnology*, 8:497–501, 2013.
- [90] R. Loudon. Theory of the first-order raman effect in crystals. *Proceedings of the Royal Society of London A: Mathematical, Physical and Engineering Sciences*, 275(1361):218–232, 1963.
- [91] Y. Maeno, H. Hashimoto, K. Yoshida, S. Nishizaki, T. Fujita, J. G. Bednorz, and F. Lichtenberg. Superconductivity in a layered perovskite without copper. *Nature*, 372(6506):532–534, 12 1994.
- [92] B. E. Maile, A. Forchel, R. Germann, and D. Grtzmacher. Impact of sidewall recombination on the quantum efficiency of dry etched ingaas/inp semiconductor wires. *Applied Physics Letters*, 54(16):1552–1554, 1989.
- [93] Kin Fai Mak, Keliang He, Changgu Lee, Gwan Hyoun Lee, James Hone, Tony F. Heinz, and Jie Shan. Tightly bound trions in monolayer mos<sub>2</sub>. *Nature Materials*, 7(8):207–211, 2013.
- [94] Kin Fai Mak, Changgu Lee, James Hone, Jie Shan, and Tony F. Heinz. Atomically thin mos<sub>2</sub>: A new direct-gap semiconductor. *Phys. Rev. Lett.*, 105:136805, Sep 2010.

- [95] L.M. Malard, M.A. Pimenta, G. Dresselhaus, and M.S. Dresselhaus. Raman spectroscopy in graphene. *Physics Reports*, 473:51–87, 2009.
- [96] Michelle S. Malcuit, Daniel J. Gauthier, and Robert W. Boyd. Suppression of amplified spontaneous emission by the four-wave mixing process. *Phys. Rev. Lett.*, 55:1086–1089, Sep 1985.
- [97] Massicotte M., Schmidt P., Violla F., Schädler K. G., Reserbat-Plantey A., Watanabe K., Taniguchi T., Tielrooij K. J., and Koppens F. H. L. Picosecond photoresponse in van der Waals heterostructures. *Nat Nano*, 11(1):42–46, 01 2016.
- [98] Inanc Meric, Melinda Y. Han, Andrea F. Young, Barbaros Ozyilmaz, Philip Kim, and Kenneth L. Shepard. Current saturation in zero-bandgap, top-gated graphene field-effect transistors. *Nat Nano*, 3(11):654–659, 11 2008.
- [99] R. Merlin. Generating coherent {THz} phonons with light pulses. *Solid State Communications*, 102(23):207 – 220, 1997. Highlights in Condensed Matter Physics and Materials Science.
- [100] D. A. B. Miller, D. S. Chemla, T. C. Damen, A. C. Gossard, W. Wiegmann, T. H. Wood, and C. A. Burrus. Electric field dependence of optical absorption near the band gap of quantum-well structures. *Phys. Rev. B*, 32:1043–1060, Jul 1985.
- [101] Tomobumi Mishina, Kazuki Nitta, and Yasuaki Masumoto. Coherent lattice vibration of interlayer shearing mode of graphite. *Phys. Rev. B*, 62:2908–2911, Jul 2000.
- [102] M. Mohr, J. Maultzsch, E. Dobardžić, S. Reich, I. Milošević, M. Damnjanović, A. Bosak, M. Krisch, and C. Thomsen. Phonon dispersion of graphite by inelastic x-ray scattering. *Phys. Rev. B*, 76:035439, Jul 2007.
- [103] J. M. Moison, K. Elcess, F. Houzay, J. Y. Marzin, J. M. Gérard, F. Barthe, and M. Bensoussan. Near-surface GaAs/Ga<sub>0.7</sub>Al<sub>0.3</sub>As quantum wells: Interaction with the surface states. *Phys. Rev. B*, 41:12945–12948, Jun 1990.
- [104] Keith A. Nelson and M. D. Fayer. Laser induced phonons: A probe of intermolecular interactions in molecular solids. *The Journal of Chemical Physics*, 72(9):5202–5218, 1980.
- [105] Keith A. Nelson, R. J. Dwayne Miller, D. R. Lutz, and M. D. Fayer. Op-

- tical generation of tunable ultrasonic waves. *Journal of Applied Physics*, 53(2):1144–1149, 1982.
- [106] Ryan W. Newson, Jesse Dean, Ben Schmidt, and Henry M. van Driel. Ultrafast carrier kinetics in exfoliated graphene and thin graphite films. *Opt. Express*, 17(4):2326–2333, Feb 2009.
- [107] Ji-Young Noh, Hanchul Kim, and Yong-Sung Kim. Stability and electronic structures of native defects in single-layer  $\text{mos}_2$ . *Phys. Rev. B*, 89:205417, May 2014.
- [108] K. S. Novoselov, A. K. Geim, S. V. Morozov, D. Jiang, Y. Zhang, S. V. Dubonos, I. V. Grigorieva, and A. A. Firsov. Electric field effect in atomically thin carbon films. *Science*, 306(5696):666–669, 2004.
- [109] A. D. O’Connell, M. Hofheinz, M. Ansmann, Radoslaw C. Bialczak, M. Lenander, Erik Lucero, M. Neeley, D. Sank, H. Wang, M. Weides, J. Wenner, John M. Martinis, and A. N. Cleland. Quantum ground state and single-phonon control of a mechanical resonator. *Nature*, 464(7289):697–703, 04 2010.
- [110] IDC Worldwide Internet of Things Forecast. Idc’s worldwide internet of things taxonomy, 2015, worldwide internet of things forecast, 20152020. IDC, 2015.
- [111] Manuel Cardona Peter Y. Yu. *Fundamentals of Semiconductors*. Springer, 2010.
- [112] S. G. Petrosian and A. Ia. Shik. Contact phenomena in low-dimensional electron systems. *Zhurnal Eksperimental’noi i Teoreticheskoi Fiziki*, 96:2229–2239, 1989.
- [113] W. A. Phillips. Comment on “two-level systems observed in the mechanical properties of single-crystal silicon at low temperatures”. *Phys. Rev. Lett.*, 61:2632–2632, Nov 1988.
- [114] A. S. Pine. Brillouin scattering in semiconductors. *Light Scattering in Solids*, 8:254–272, 1975.
- [115] Stefano Piscanec, Michele Lazzeri, J. Robertson, Andrea C. Ferrari, and Francesco Mauri. Optical phonons in carbon nanotubes: Kohn anomalies, peierls distortions, and dynamic effects. *Phys. Rev. B*, 75:035427, Jan 2007.

- [116] Leonhard Prechtel, Li Song, Stephan Manus, Dieter Schuh, Werner Wegscheider, and Alexander W. Holleitner. Time-resolved picosecond photocurrents in contacted carbon nanotubes. *Nano Letters*, 11(1):269–272, 2011. PMID: 21142051.
- [117] Leonhard Prechtel, Li Song, Dieter Schuh, Pulickel Ajayan, Werner Wegscheider, and Alexander W. Holleitner. Time-resolved ultrafast photocurrents and terahertz generation in freely suspended graphene. *Nat Commun*, 3:646, Jan 2012.
- [118] Hao Qiu, Tao Xu, Zilu Wang, Wei Ren, Haiyan Nan, Zhenhua Ni, Qian Chen, Shijun Yuan, Feng Miao, Fengqi Song, Gen Long, Yi Shi, Litao Sun, Jinlan Wang, and Xinran Wang. Hopping transport through defect-induced localized states in molybdenum disulphide. *Nature Communications*, 4(2642):–, 2013.
- [119] Dean C. R., Young A. F., Meric I., Lee C., Wang L., Sorgenfrei S., Watanabe K., Taniguchi T., Kim P., Shepard K. L., and Hone J. Boron nitride substrates for high-quality graphene electronics. *Nat Nano*, 5(10):722–726, 10 2010.
- [120] S Ramo. Currents induced by electron motion. *Proceedings of the IRE*, 27:584–585, 1939.
- [121] F. Rana. Graphene terahertz plasmon oscillators. *IEEE Transactions on Nanotechnology*, 7(1):91–99, Jan 2008.
- [122] Farhan Rana, Paul A. George, Jared H. Strait, Jahan Dawlaty, Shriram Shivaraman, Mvs Chandrashekar, and Michael G. Spencer. Carrier recombination and generation rates for intravalley and intervalley phonon scattering in graphene. *Phys. Rev. B*, 79:115447, Mar 2009.
- [123] C. N. R. Rao, K. Gopalakrishnan, and Urmimala Maitra. Comparative study of potential applications of graphene, mos2, and other two-dimensional materials in energy devices, sensors, and related areas. *ACS Applied Materials & Interfaces*, 7(15):7809–7832, 2015. PMID: 25822145.
- [124] Alfonso Reina, Xiaoting Jia, John Ho, Daniel Nezich, Hyungbin Son, Vladimir Bulovic, Mildred S. Dresselhaus, and Jing Kong. Large area, few-layer graphene films on arbitrary substrates by chemical vapor deposition. *Nano Letters*, 9(1):30–35, 2009. PMID: 19046078.
- [125] F. A. Riddoch and M. Jaros. Auger recombination cross section associated with deep traps in semiconductors. *J. Phys. C: Solid St. Phys.*, 13:6181, 1980.

- [126] B. K. Ridley. *Quantum Processes in Semiconductors*. Oxford University Press, New York, USA, 5 edition, 2013.
- [127] D J Robbins and P T Landsberg. Impact ionisation and auger recombination involving traps in semiconductors. *Journal of Physics C: Solid State Physics*, 13(12):2425, 1980.
- [128] Jason S. Ross, Philip Klement, Aaron M. Jones, Nirmal J. Ghimire, Jiaqiang Yan, D. G. Mandrus, Takashi Taniguchi, Kenji Watanabe, Kenji Kitamura, Wang Yao, David H. Cobden, and Xiaodong Xu. Electrically tunable excitonic light-emitting diodes based on monolayer wse<sub>2</sub> pn junctions. *Nature Nanotechnology*, 9:268–272, 2014.
- [129] D. Rugar, R. Budakian, H. J. Mamin, and B. W. Chui. Single spin detection by magnetic resonance force microscopy. *Nature*, 430(6997):329–332, 07 2004.
- [130] J. R. Salcedo, A. E. Siegman, D. D. Dlott, and M. D. Fayer. Dynamics of energy transport in molecular crystals: The picosecond transient-grating method. *Phys. Rev. Lett.*, 41:131–134, Jul 1978.
- [131] TriQuint Semiconductor. Company presentation. *TriQuint Semiconductor*, 2014.
- [132] C. Seoáñez, F. Guinea, and A. H. Castro Neto. Surface dissipation in nanoelectromechanical systems: Unified description with the standard tunneling model and effects of metallic electrodes. *Phys. Rev. B*, 77:125107, Mar 2008.
- [133] Ilan Shalish, Henryk Temkin, and Venkatesh Narayanamurti. Size-dependent surface luminescence in zno nanowires. *Phys. Rev. B*, 69:245401, Jun 2004.
- [134] Yuyan Shao, Jun Wang, Hong Wu, Jun Liu, IlhanA. Aksay, and Yuehe Lin. Graphene based electrochemical sensors and biosensors: A review. *Electroanalysis*, 22(10):1027–1036, 2010.
- [135] Hongyan Shi, Rusen Yan, Simone Bertolazzi, Jacopo Brivio, Bo Gao, Andras Kis, Debdeep Jena, Huili Grace Xing, and Libai Huang. Exciton dynamics in suspended monolayer and few-layer mos<sub>2</sub> 2d crystals. *ACS Nano*, 7(2):1072–1080, 2013.

- [136] W Shockley. Currents to conductors induced by a moving point charge. *Journal of Appl. Phys*, 9:635–636, 1938.
- [137] Sangwan Sim, Jusang Park, Jeong-Gyu Song, Chihun In, Yun-Shik Lee, Hyungjun Kim, and Hyunyong Choi. Exciton dynamics in atomically thin  $\text{mos}_2$ : Interexcitonic interaction and broadening kinetics. *Phys. Rev. B*, 88:075434, Aug 2013.
- [138] Michael Slutsky, Mehran Kardar, and Leonid A. Mirny. Diffusion in correlated random potentials, with applications to dna. *Phys. Rev. E*, 69:061903, Jun 2004.
- [139] Daohua Song, Feng Wang, Gordana Dukovic, M. Zheng, E. D. Semke, Louis E. Brus, and Tony F. Heinz. Direct measurement of the lifetime of optical phonons in single-walled carbon nanotubes. *Phys. Rev. Lett.*, 100:225503, Jun 2008.
- [140] Andrea Splendiani, Liang Sun, Yuanbo Zhang, Tianshu Li, Jonghwan Kim, Chi-Yung Chim, Giulia Galli, and Feng Wang. Emerging photoluminescence in monolayer  $\text{mos}_2$ . *Nano Letters*, 10(4):1271–1275, 2010. PMID: 20229981.
- [141] T. E. Stevens, J. Kuhl, and R. Merlin. Coherent phonon generation and the two stimulated raman tensors. *Phys. Rev. B*, 65:144304, Mar 2002.
- [142] Jared H. Strait, Parinita Nene, and Farhan Rana. High intrinsic mobility and ultrafast carrier dynamics in multilayer metal-dichalcogenide  $\text{mos}_2$ . *Phys. Rev. B*, 90:245402, Dec 2014.
- [143] Jared H. Strait, Haining Wang, Shriram Shivaraman, Virgil Shields, Michael Spencer, and Farhan Rana. Very slow cooling dynamics of photoexcited carriers in graphene observed by optical-pump terahertz-probe spectroscopy. *Nano Letters*, 11(11):4902–4906, 2011. PMID: 21973122.
- [144] Chi-Kuang Sun, Jian-Chin Liang, and Xiang-Yang Yu. Coherent acoustic phonon oscillations in semiconductor multiple quantum wells with piezoelectric fields. *Phys. Rev. Lett.*, 84:179–182, Jan 2000.
- [145] Dezheng Sun, Yi Rao, Georg A. Reider, Gugang Chen, Yumeng You, Louis Brzin, Avetik R. Harutyunyan, and Tony F. Heinz. Observation of rapid excitonexciton annihilation in monolayer molybdenum disulfide. *Nano Letters*, 14(10):5625–5629, 2014. PMID: 25171389.

- [146] Dong Sun, Grant Aivazian, Aaron M. Jones, Jason S. Ross, Wang Yao, David Cobden, and Xiaodong Xu. Ultrafast hot-carrier-dominated photocurrent in graphene. *Nat Nano*, 7(2):114–118, 02 2012.
- [147] R. S. Sundaram, M. Engel, A. Lombardo, R. Krupke, A. C. Ferrari, Ph. Avouris, and M. Steiner. Electroluminescence in single layer mos<sub>2</sub>. *Nano Letters*, 13(4):1416–1421, 2013.
- [148] R. Tabrizian, M. Rais-Zadeh, and F. Ayazi. Effect of phonon interactions on limiting the f.q product of micromechanical resonators. In *TRANSDUCERS 2009 - 2009 International Solid-State Sensors, Actuators and Microsystems Conference*, pages 2131–2134, June 2009.
- [149] K. Tahy, S. Koswatta, T. Fang, Q. Zhang, H. Xing, and D. Jena. High field transport properties of 2d and nanoribbon graphene fets. In *2009 Device Research Conference*, pages 207–208, June 2009.
- [150] K. Tai, T. R. Hayes, S. L. McCall, and W. T. Tsang. Optical measurement of surface recombination in ingaas quantum well mesa structures. *Applied Physics Letters*, 53(4):302–303, 1988.
- [151] Akinori Tanaka, Neil J. Watkins, and Yongli Gao. Hot-electron relaxation in the layered semiconductor  $2h - \text{mos}_2$  studied by time-resolved two-photon photoemission spectroscopy. *Phys. Rev. B*, 67:113315, Mar 2003.
- [152] C. Thomsen, H. T. Grahn, H. J. Maris, and J. Tauc. Surface generation and detection of phonons by picosecond light pulses. *Phys. Rev. B*, 34:4129–4138, Sep 1986.
- [153] Michael Tinkham. *Group Theory and Quantum Mechanics*. McGraw-Hill Book Company, 1964.
- [154] F. Tuinstra and J. L. Koenig. Raman spectrum of graphite. *The Journal of Chemical Physics*, 53(3):1126–1130, 1970.
- [155] Miguel M. Ugeda, Aaron J. Bradley, Su-Fei Shi, Felipe H. da Jornada, Yi Zhang, Diana Y. Qiu, Wei Ruan, Sung-Kwan Mo, Zahid Hussain, Zhi-Xun Shen, Feng Wang, Steven G. Louie, and Michael F. Crommie. Giant bandgap renormalization and excitonic effects in a monolayer transition metal dichalcogenide semiconductor. *Nat Mater*, 13(12):1091–1095, 12 2014.

- [156] Alexander Urich, Karl Unterrainer, and Thomas Mueller. Intrinsic response time of graphene photodetectors. *Nano Letters*, 11(7):2804–2808, 2011. PMID: 21627096.
- [157] J T M van Beek and R Puers. A review of mems oscillators for frequency reference and timing applications. *Journal of Micromechanics and Microengineering*, 22(1):013001, 2012.
- [158] Arend M. van der Zande, Robert A. Barton, Jonathan S. Alden, Carlos S. Ruiz-Vargas, William S. Whitney, Phi H. Q. Pham, Jiwoong Park, Jeevak M. Parpia, Harold G. Craighead, and Paul L. McEuen. Large-scale arrays of single-layer graphene resonators. *Nano Letters*, 10(12):4869–4873, 2010. PMID: 21080681.
- [159] Arend M. Van der Zande, Pinshane Y. Huang, Daniel A. Chenet, Timothy C. Berkelbach, YuMeng You, Gwan-Hyoung Lee, Tony F. Heinz, David R. Reichman, David A. Muller, and James C. Hone. Grains and grain boundaries in highly crystalline monolayer molybdenum disulphide. *Nature Materials*, 12(6):554–561, 2013.
- [160] Patrick Vogt, Paola De Padova, Claudio Quaresima, Jose Avila, Emmanouil Frantzeskakis, Maria Carmen Asensio, Andrea Resta, Bénédicte Ealet, and Guy Le Lay. Silicene: Compelling experimental evidence for graphenelike two-dimensional silicon. *Phys. Rev. Lett.*, 108:155501, Apr 2012.
- [161] Ioana Voiculescu and Anis Nurashikin Nordin. Acoustic wave based {MEMS} devices for biosensing applications. *Biosensors and Bioelectronics*, 33(1):1 – 9, 2012.
- [162] Haining Wang, Sandip Tiwari Changjian Zhang, Weimin Chan, and Farhan Rana. Ultrafast response of monolayer mos2 photodetectors. *Nature Comm.*, 6:9831, Nov 2015.
- [163] Haining Wang, Jared H. Strait, Paul A. George, Shriram Shivaraman, Virgil B. Shields, Mvs Chandrashekhar, Jeonghyun Hwang, Farhan Rana, Michael G. Spencer, Carlos S. Ruiz-Vargas, and Jiwoong Park. Ultrafast relaxation dynamics of hot optical phonons in graphene. *Applied Physics Letters*, 96:081917, 2010.
- [164] Haining Wang, Jared H. Strait, Changjian Zhang, Weimin Chan, Christina Manolatou, Sandip Tiwari, and Farhan Rana. Fast exciton annihilation by

capture of electrons or holes by defects via auger scattering in monolayer metal dichalcogenides. *Phys. Rev. B*, 91:165411, Apr 2015.

- [165] Haining Wang, Changjian Zhang, Weimin Chan, Christina Manolatu, Sandip Tiwari, and Farhan Rana. Radiative lifetimes of excitons and trions in monolayers of the metal dichalcogenide  $\text{mos}_2$ . *Phys. Rev. B*, 93:045407, Jan 2016.
- [166] Haining Wang, Changjian Zhang, and Farhan Rana. Ultrafast carrier dynamics in single and few layer  $\text{mos}_2$  studied by optical pump probe technique. In *CLEO: 2013*, page QTu1D.2. Optical Society of America, 2013.
- [167] Haining Wang, Changjian Zhang, and Farhan Rana. Surface recombination limited lifetimes of photoexcited carriers in few-layer transition metal dichalcogenide  $\text{mos}_2$ . *Nano Letters*, 0(0):null, 2015. PMID: 26535607.
- [168] Haining Wang, Changjian Zhang, and Farhan Rana. Ultrafast dynamics of defect-assisted electronhole recombination in monolayer  $\text{mos}_2$ . *Nano Letters*, 15(1):339–345, 2015. PMID: 25546602.
- [169] Han Wang, Lili Yu, Yi-Hsien Lee, Yumeng Shi, Allen Hsu, Matthew L. Chin, Lain-Jong Li, Madan Dubey, Jing Kong, and Tomas Palacios. Integrated circuits based on bilayer  $\text{mos}_2$  transistors. *Nano Letters*, 12(9):4674–4680, 2012. PMID: 22862813.
- [170] Qing Hua Wang, Kourosh Kalantar-Zadeh, Andras Kis, Jonathan N. Coleman, and Michael S. Strano. Electronics and optoelectronics of two-dimensional transition metal dichalcogenides. *Nat Nano*, 7(11):699–712, 11 2012.
- [171] Rui Wang, Brian A. Ruzicka, Nardeep Kumar, Matthew Z. Bellus, Hsin-Ying Chiu, and Hui Zhao. Ultrafast and spatially resolved studies of charge carriers in atomically thin molybdenum disulfide. *Phys. Rev. B*, 86:045406, Jul 2012.
- [172] Wei-Cheng Wang, Che-Wei Lin, Hsin-Jui Chen, Che-Wei Chang, Jhih-Jie Huang, Ming-Jui Yang, Budi Tjahjono, Jian-Jia Huang, Wen-Ching Hsu, and Miin-Jang Chen. Surface passivation of efficient nanotextured black silicon solar cells using thermal atomic layer deposition. *ACS Applied Materials & Interfaces*, 5(19):9752–9759, 2013. PMID: 24028609.
- [173] G. K. Wertheim. Transient recombination of excess carriers in semiconductors. *Phys. Rev.*, 109:1086–1091, Feb 1958.

- [174] Sanfeng Wu, Sonia Buckley, John R. Schaibley, Liefeng Feng, Jiaqiang Yan, David G. Mandrus, Fariba Hatami, Wang Yao, Jelena Vuckovic, Arka Majumdar, and Xiaodong Xu. Monolayer semiconductor nanocavity lasers with ultralow thresholds. *Nature*, 520(7545):69–72, 04 2015.
- [175] Wenzhuo Wu, Lei Wang, Yilei Li, Fan Zhang, Long Lin, Simiao Niu, Daniel Chenet, Xian Zhang, Yufeng Hao, Tony F. Heinz, James Hone, and Zhong Lin Wang. Piezoelectricity of single-atomic-layer mos<sub>2</sub> for energy conversion and piezotronics. *Nature*, 514(7523):470–474, Oct 2014. Letter.
- [176] Fengnian Xia, Thomas Mueller, Rokhsana Golizadeh-Mojarad, Marcus Freitag, Yu ming Lin, James Tsang, Vasili Perebeinos, and Phaedon Avouris. Photocurrent imaging and efficient photon detection in a graphene transistor. *Nano Letters*, 9(3):1039–1044, 2009. PMID: 19203207.
- [177] E. Yablonovitch, D. L. Allara, C. C. Chang, T. Gmitter, and T. B. Bright. Unusually low surface-recombination velocity on silicon and germanium surfaces. *Phys. Rev. Lett.*, 57:249–252, Jul 1986.
- [178] Aishi Yamamoto, Tomobumi Mishina, Yasuaki Masumoto, and Masaaki Nakayama. Coherent oscillation of zone-folded phonon modes in gaas-alas superlattices. *Phys. Rev. Lett.*, 73:740–743, Aug 1994.
- [179] K. J. Yee, K. G. Lee, E. Oh, D. S. Kim, and Y. S. Lim. Coherent optical phonon oscillations in bulk gan excited by far below the band gap photons. *Phys. Rev. Lett.*, 88:105501, Feb 2002.
- [180] Zongyou Yin, Hai Li, Hong Li, Lin Jiang, Yumeng Shi, Yinghui Sun, Gang Lu, Qing Zhang, Xiaodong Chen, and Hua Zhang. Single-layer mos<sub>2</sub> phototransistors. *ACS Nano*, 6(1):74–80, 2012.
- [181] Shengjun Yuan, Rafael Roldán, M. I. Katsnelson, and Francisco Guinea. Effect of point defects on the optical and transport properties of mos<sub>2</sub> and ws<sub>2</sub>. *Phys. Rev. B*, 90:041402, Jul 2014.
- [182] Won Seok Yun, S. W. Han, Soon Cheol Hong, In Gee Kim, and J. D. Lee. Thickness and strain effects on electronic structures of transition metal dichalcogenides: 2h-*mX*<sub>2</sub> semiconductors (*m* = mo, w; *x* = s, se, te). *Phys. Rev. B*, 85:033305, Jan 2012.
- [183] Z. H. Ni, H. M. Wang, J. Kasim, H. M. Fan, , T. Yu, Y. H. Wu, Y. P. Feng, , and Z. X. Shen\*. Graphene thickness determination using reflection and contrast spectroscopy. *Nano Letters*, 7(9):2758–2763, 2007. PMID: 17655269.

- [184] H. J. Zeiger, J. Vidal, T. K. Cheng, E. P. Ippen, G. Dresselhaus, and M. S. Dresselhaus. Theory for displacive excitation of coherent phonons. *Phys. Rev. B*, 45:768–778, Jan 1992.
- [185] Changjian Zhang, Haining Wang, Weimin Chan, Christina Manolatu, and Farhan Rana. Absorption of light by excitons and trions in monolayers of metal dichalcogenide  $\text{MoS}_2$ : Experiments and theory. *Phys. Rev. B*, 89:205436, May 2014.
- [186] Saifeng Zhang, Ningning Dong, Niall McEvoy, Maria O'Brien, Sinad Winters, Nina C. Berner, Chanyoung Yim, Yuanxin Li, Xiaoyan Zhang, Zhang-hai Chen, Long Zhang, Georg S. Duesberg, and Jun Wang. Direct observation of degenerate two-photon absorption and its saturation in  $\text{ws}_2$  and  $\text{mos}_2$  monolayer and few-layer films. *ACS Nano*, 9(7):7142–7150, 2015. PMID: 26135798.
- [187] Y. J. Zhang, T. Oka, R. Suzuki, J. T. Ye, and Y. Iwasa. Electrically switchable chiral light-emitting transistor. *Science*, 344(6185):725–728, 2014.
- [188] Weijie Zhao, R. M. Ribeiro, Minglin Toh, Alexandra Carvalho, Christian Kloc, A. H. Castro Neto, and Goki Eda. Origin of indirect optical transitions in few-layer  $\text{mos}_2$ ,  $\text{ws}_2$ , and  $\text{wse}_2$ . *Nano Letters*, 13(11):5627–5634, 2013. PMID: 24168432.
- [189] Yanyuan Zhao, Xin Luo, Hai Li, Jun Zhang, Paulo T. Araujo, Chee Kwan Gan, Jumiati Wu, Hua Zhang, Su Ying Quek, Mildred S. Dresselhaus, and Qihua Xiong. Interlayer breathing and shear modes in few-trilayer  $\text{mos}_2$  and  $\text{wse}_2$ . *Nano Letters*, 13(3):1007–1015, 2013. PMID: 23432683.
- [190] Wu Zhou, Xiaolong Zou, Sina Najmaei, Zheng Liu, Yumeng Shi, Jing Kong, Jun Lou, Pulickel M. Ajayan, Boris I. Yakobson, and Juan-Carlos Idrobo. Intrinsic structural defects in monolayer molybdenum disulfide. *Nano Letters*, 13(6):2615–2622, 2013.